SENSOR TECHNOLOGIES FOR MEASURING COASTAL HYDRODYNAMICS AND MORPHOLOGICAL CHANGE

Thesis submitted in accordance with the requirements of the University of Liverpool for the degree of Doctor in Philosophy

By

Philip John Knight

School of Environmental Science

Department of Geography and Planning

October 2022

DECLARATION

This thesis is the result of my own work and includes nothing which is the outcome of work done in collaboration except here specifically indicated in the text. It has not been previously submitted, in part or whole, to any university institution for any degree, diploma, or other qualification.

In accordance with the university of Liverpool guidelines, this thesis does not exceed 100,000 words.

Signed: P. J. Knight

Date: 24 October 2022

Philip John Knight.

Contributions by authors to manuscripts:

Chapter 2: Knight, P.J.; Bird, C.O.; Sinclair, A.; Plater, A.J. A low-cost GNSS buoy platform for measuring coastal sea levels. Ocean Eng. 2020, 203, 107198, doi:10.1016/j.oceaneng.2020.107198.

P.K. conceived, designed, developed software, performed the experiments, analysed the data and wrote the original draft.

A.P. reviewed and commented on the final draft.

A.P. provided supervision.

C.B and A.S. provided project administration and resources.

Chapter 3: Knight, P., Bird, C., Sinclair, A., Higham, J., & Plater, A. (2021). Testing an "IoT" tide gauge network for coastal monitoring. IoT, 2(1), 17-32.

P.K. conceived, designed, developed software, performed the experiments, analysed the data and wrote the original draft.

A.P. reviewed and commented on the final draft.

A.P. and J.H. provided supervision.

C.B and A.S. provided project administration and resources.

Chapter 4: Knight, P. J., Bird, C. O., Sinclair, A., Higham, J., & Plater, A. J. (2021). Beach Deployment of a Low-Cost GNSS Buoy for Determining Sea-Level and Wave Characteristics. Geosciences, 11(12), 494.

P.K. conceived, designed, developed software, performed the experiments, analysed the data and wrote the original draft.

A.P. reviewed and commented on the final draft.

A.P. and J.H. provided supervision.

C.B and A.S. provided project administration and resources.

ABSTRACT

Sensor technologies for measuring coastal hydrodynamics and morphological change

Philip Knight

This research has focused on development of cost-effective sea-level and wave measuring technologies for implementation alongside X-band radar monitoring programmes. These data are important for two reasons: firstly, sea-level data are required for deriving the morphological maps from the X-band radar images; these maps can inform coastal managers of critical lowering of beach levels that might compromise sea-defences, or high beach levels that might exacerbate run-up and overtopping hazard, and secondly, sea-level and wave data can be used to understand the role of tides, storm surges and waves in shaping beaches and tidal flats. While there are numerous commercial devices capable of measuring sea level and waves, many are not suitable for the intertidal zone and those that can are generally too expensive to deploy for long durations or to implement at scale as part of a near-real time system. This research is based upon taking ideas and developed products from other sectors and transferring these advances to create low-cost devices. This research has successfully produced and evaluated two devices with field experiments; a low-cost GNSS buoy capable of deployment from a small boat or from the beach at low water, and an Internet of Things (IoT) tide gauge capable of scaling up to provide a network of near/real time devices. A comparison of tidal heights between the GNSS buoy and a reference tide gauge at Holyhead harbour (located 1.5 km away) produced a mean difference of -1.1cm and a RMSE of 1.4 cm, indicating its suitability for sea level measurement. Likewise, a comparison between the IoT tide gauge and a reference tide at Gladstone Lock, Liverpool (located 2.6 km upstream), produced a mean difference of 0.2 cm and a RMSE 3.5 cm, showing that acceptable data can also be obtained using low-cost pressure sensors.

The research also sets out to develop a method of using temporal X-band derived Digital Elevation Models (DEMs) (which contain spatial elevation errors), alongside more accurate annual LiDAR data, to characterise morphological changes of a tide flat. Analysis of DEMs over a three-year period shows the importance of regular monitoring of beach morphology over annual surveys. The results indicate the presence and shoreward movement of small sand ridges situated between the mean-sea-level and mean-low-water-springs. There are also regular cycles of erosion and deposition and these appear to be related to both the tidal height and stormy periods. The two-week X-band radar composite maps of the intertidal zone are not at a resolution capable of analysing the effect of individual storm events, or to separate parts of the tidal cycle e.g., neap tides over seven days. Future surveys with the X-band radar would benefit from the instrumentation developed as part of this research. This would improve the data quality, allow for increased temporal output i.e., more maps, and thus provide the additional data necessary to solve some of the issues encountered with analysis of the historical data.

ACKNOWLEDGEMENTS

I would like to thank my supervisors, Prof Andy Plater and Dr Jonathan Higham for their help, advice and feedback which they have provided during the course of this work. I would particularly like to thank Prof Andy Plater for his friendly encouragement during the past five years and for guidance with research publications and manuscript development. I would also like to acknowledge the engineering support offered from staff at the National Oceanography Centre.

The research was funded by the "Low Carbon Eco-Innovatory (LCEI)—Liverpool University" (www.liverpool.ac.uk/environmental-sciences/working-with-business), with industrial partner MM Sensors Ltd. I would also like to thank Alex Sinclair and Cai Bird for their contribution as excellent industrial partners; for providing historical X-band data and advice throughout my research journey.

Thanks also go to my friend Andy Lane for proof reading my research paper manuscripts and providing me with constructive feedback before submission to journals.

Finally, thanks to both my wife Lisa for putting up with me during these last few years of seemingly endless evenings finalising this thesis, and as a practicing Christian, to God for providing me this opportunity in the first place and for being with me every step of the way.

Table of Contents

List of Figures

List of Tables

1 Introduction

Whilst sea-level data are routinely collected at harbours and ports there are significant gaps along most coastlines, where measurements are limited or even absent. Sea-level data in near-real time can help with informed decision making in areas at flood risk, e.g., low-lying coastal communities. Also, sea-level data are an essential requirement for understanding morphological change as part of a coastal monitoring programme. The intertidal zone can provide the first level of protection against extreme sea-levels, e.g., sand banks attenuating the action of large waves (Hanley et al., 2014). This level of protection can also be compromised by a single extreme event or by a series of smaller events over time (Coco et al., 2014). Beach replenishment schemes (Van den Hoek et al., 2012) are often employed to reset the level of flood protection provided by the shoreline, and thus there is a requirement for regular spatial surveys. With some spatial surveying methods localised tidal data are required as part of the methodology, e.g., waterline method used with X-band radar data to derive morphological maps (Bell et al., 2016).

The absence of sea-level measurements in the intertidal zone is partly historical, since tide gauges were originally setup to aid maritime activities, and beaches and tidal flats are often difficult environments for installation. In addition, equipment and on-going maintenance costs can often prohibit long-term installation at remote locations. This research has explored the current methods of sea-level measurement and identified two areas for development, to provide cost effective solutions for sea-level measurement which are also suitable for the intertidal zone.

The research is based upon utilising new advances in technology from other fields of research and commercial sectors, and applying them to sea-level measurement; to develop these devices so that they can be incorporated into localised networks and to supplement data from high-end oceanographic instrumentation. Measurements of waves in the intertidal zone are a useful addition to offshore wave data due to wave transformation in the intertidal zone; waves travelling from offshore are affected by the seabed through processes such as refraction, shoaling, bottom friction and wave breaking. These devices have been developed to the first stage of evaluation and to show that they are fit for purpose, and thus only deal with the initial design and implementation.

The research also investigates morphological change using derived digital elevation models (DEMs) from X-band radar/Light Detection and Ranging (LiDAR) surveys, sea-level data and wave data. LiDAR is commonly used to produce morphological maps of the intertidal zone (Miles et al., 2019), and is a method for determining ranges (variable distance) by targeting an object or a surface with a laser and measuring the time for the reflected light to return to the receiver. In the first instance, 2-weekly DEMs derived from X-band radar and annual LiDAR DEMs are used to describe morphological changes within the intertidal zone over a three-year period. Data masking techniques are then applied to extract the ‘best data’ from the X-band radar derived DEMs in order to calculate temporal changes

in morphology Finally, tidal, storm surge, wave data are used to assess the contribution of tidal range and wave height to the calculated changes in the sediment budget.

The GNSS buoy platform was developed in a step by step process. The first stage of the process was testing the positional capabilities of a low-cost GNSS receiver using an evaluation kit based upon the U-blox M8T GNSS receiver and logging data to a desktop computer. After the static testing, the configuration was ported to a floating pontoon alongside the Liverpool water front (to capture vertical movement over the 10-m tidal range). To make the hardware portable, a stand-alone data logger was purchased together with a water proof casing; the GNSS receiver was powered by a USB battery pack and the logger by a 9-volt alkaline battery. After a successful trial, the same hardware was then attached to the stern of a sailing club committee boat moored in the Dee Estuary. This demonstrated the capability of the hardware in a realistic marine environment. At the same time the buoy platform was developed (see Appendix 8.4) and tested in the West Kirby Marine lake. To keep costs low it was constructed using small diameter aluminum scaffold poles along with standard connectors, with floatation provided by trawler fishing net floats. After the early GNSS testing, an Emlid Reach was identified as a suitable alternative to the original setup; this used an Edison micro-computer running Linux, internal logging, with WiFi capability, and had an embedded U-Blox M8T GNSS receiver (this hardware setup was relatively new and aimed at the emerging drone survey market). Both the Emlid Reach setup and buoy platform were then evaluated at two locations, one within Holyhead harbour, and another at an intertidal site at Rossall Point, near Fleetwood.

The IoT tide was developed by first identifying a suitable low-cost pressure sensor to couple with a low-power microcomputer with IoT capabilities i.e., with telemetry capable of two-way communication. The pressure sensor was first tested in the laboratory by varying water levels in a plastic tube (see Appendix 8.3); this was constructed using plastic tubing, clamps and plumbing connections. The pressure sensor was coupled with an Arduino microcontroller which was then attached to a laptop via a USB cable. Later software scripts were written for the Arduino (see Appendix 8.1) to enable these data to be sent in real-time via the SigFox network to a cloud data server (see Appendix 8.2). Data signals across long cables (>10m) were tested in the laboratory using I^2C differential convertors; I^2C sensors are limited to cable lengths of 1m. Field evaluations were then carried out, one using a 10m cable configuration and another with self-contained logging as well as telemetry.

1.1 Monitoring the coastal zone

It is important to monitor shallow water environments around the coast, especially when they are adjacent to large populated areas and high value infrastructure assets e.g., ports, oil refineries and power stations. The intertidal and subtidal zones are dynamic in nature and changes in the morphology can be significant in both the short and long term (Brand et al., 2020). These can be due to single extreme

storm events, after a succession of smaller storm events, or combinations of tidal and storm events over seasonal time scales. Another consideration is that rising sea levels, and the relatively rapid increase in sea level, will begin to impact on these coastal zones (Taherkhani et al., 2020). Protection is often required for areas of low-lying coastal communities, which generally results in the construction of high-cost concrete structures which have large carbon footprints (Dennis et al., 2018). An alternative method of providing protection against storms is the use of 'nature-based solutions'; beach replenishment schemes are common and are created by moving or introducing large quantities of sand to targeted locations within the intertidal/subtidal zones to provide protection against storms and large waves. This is often carried out on an annual basis, with repeated intervention required in the following year. For example, Sefton Council regularly monitor the beach at Crosby, located to the north of Liverpool (UK), and add sediment to locations of erosion; to alleviate potential flood risk from increased damage by waves and storms to the existing sea defences. Recently, experiments have begun using mega-beach replenishment schemes called Sand Engines (Stive et al., 2013). These interventions are orders of magnitude greater than standard beach replenishment schemes and are expected to provide protection against storms and waves for 10-20 years. Thus, there is a requirement to monitor the morphological changes over these timescales to make sure that they are still providing the design standard of protection.

There are numerous ways to monitor the intertidal zone, and these have improved over time, with new technological and computing capabilities. Shallow draft vessels using echo sounders can be used to derive bathymetry maps after correction to a local datum using Global Navigation Satellite System (GNSS) systems (Costa et al., 2009). However, they are difficult to operate in very shallow waters and within the intertidal zone. A common method is to survey beaches and tidal flats at low water using a GNSS survey (Elsner et al., 2018). This is often performed from small 4x4 vehicles in order to cover larger areas rapidly. This is a cost-effective method of surveying and producing maps, however it is likely to be not quite as effective on tidal flats where fine sand and mud sediments can reduce vehicular and foot access (Chowdhury et al., 2014) (The author whilst surveying one of the north Wirral beaches, near Liverpool, encountered mud too deep to proceed safely).

Airborne LiDAR is commonly used to produce morphological maps of the intertidal zone (Miles et al., 2019). LiDAR is a method for determining ranges (variable distance) by targeting an object or a surface with a laser and measuring the time for the reflected light to return to the receiver. To maximise coverage of the intertidal zone these surveys need to be flown during spring tidal low waters. The advantage of the LiDAR survey method is that it can produce accurate levels covering wide areas of the intertidal zone. For example, the LiDAR (EA, 2019a) data used within this research were taken from the UK Environment Agency; the Optech ALTM 3100 system flown over the Dee Estuary (area 136 km^2) has a quoted manufacturer vertical accuracy of 0.15m or better (1x standard deviation) and <1m in the horizontal (Sallenger Jr et al., 2003). However, the flights are expensive and consequently

these are generally only re-flown on an annual basis; coastal management programmes using LiDAR are usually setup for annual surveys, although the costs sometimes prohibit this frequency.

Another method is the land-based version of LiDAR called the Terrestrial Laser Scanner (TLS) which is operated from ground-level. In practice it is usually set up to produce beach profiles perpendicular to the shore line, and at regular intervals along the coast (O'Dea et al., 2019). Morphological maps can be derived by interpolation of a number of profiles (Telling et al., 2017). For example, TLS has been successfully used in a tidal flat environment to generate DEMs before and after extreme storm events (Xie et al., 2017). The advantage of this technique is that it can be used in areas not accessible to the previous ground-based survey methods, since the equipment can be operated from the shoreline. In general, all the above methods are unsuitable for reproducing morphological maps on a regular basis due to labour and system costs.

By its nature the intertidal zone can be quite dynamic with changes in spatial sedimentation (Brand et al., 2020). The previous survey methods can produce good quality morphological maps; however, these can soon become obsolete after completion. Storms and groups of storms over time can move sediment on and off the intertidal zone and sand features can develop and/or move positions (Miles et al., 2019). Therefore, a number of survey techniques have been introduced to provide more temporal coverage. One method is to use video monitoring techniques to quantify shoreline evolution and, erosional/accretional sediment volume change on intertidal beaches (Poate et al., 2009). Video output can also be used to extract subtidal beach bathymetry, to assess the performance of beach replenishment schemes and to determine wave run-up for evaluation of coastal structures.

Another approach is the use of X-band radar, which was initially used to record wave spectra, wave characteristics and current parameters (Bell, 1999; Wolf et al., 2001). In practice this requires an agitated sea surface for good signal reflection and this is typical provided when wind speeds are greater than 3 ms^{-1} and waves are greater than 1m. A technique was later developed by using the water-line method with the X-band radar outputs to derive morphological maps (Bell et al., 2016). The water-line method assumes the same water level across the radar footprint as the tide ebbs and flows, and thus if the sea-level is known at a particular time then elevation can be extracted for that location. However, the authors concluded that the method is an over-simplification for locations with increasing tidal asymmetry caused by tidal flats and sand banks, and thus additional tidal measurements within the radar footprint would be necessary to improve data quality.

1.2 Sea-level measurement

Along the coastline of most industrialized countries, sea level is routinely monitored by national organisations and port authorities for scientific studies and for safe navigation. These are often located

at harbours/ports and are traditionally installed in sheltered areas to reduce the impact of waves on the measurements (Pugh et al., 2014). Also, specific wave buoys, as part of national networks tend to be deployed further offshore, and are generally limited in number and spread out along the coastline (WaveNet, 2022). In the intertidal zone, there is a lack of continuous sea-level and wave measurements, with most of the data coming from short-term research projects. As part of coastal monitoring programmes, additional sea-level and wave data are needed to understand the fundamental local processes affecting the coastal zone, however the costs of implementing commercial systems often make them prohibitive. For example, generation of morphological maps using the waterline method and X-band radar data requires accurate local sea-level data (Bell et al., 2016). This technique provides an efficient way of producing a series of morphological maps, however it also needs complementary low-cost sea-level measurements, as part of an overall cost-effective monitoring solution.

Devices capable of capturing sea-level can be characterised into three main groups; surface following devices, fixed sensors and remote /mobile sensors. Examples of surface following devices include tide poles which are vertical mounted rulers and systems transferring the level of a float in a stilling well (which allows water in at the base) to a recording device. The former is a tedious measurement to take as it is required to be manually read by eye, however it is an inexpensive method that has been used successfully since Egyptian times. It has an accuracy of between 0.02-0.10m (Pugh et al., 2014). For example, Hutchinson in the 18th century managed to manually record high waters at Liverpool over a thirty-year period from 1768, and these data, contributing to the 2nd longest sea-level record in the world, have since been used to investigate long-term sea level rise (Woodworth, 1999). The float gauge is a later innovation (late 19th century), and is a robust method due to the float being contained within a stilling well with an open interface at the bottom (Pugh, 1987). This type of gauge and has accuracy between 0.01-0.05m, however it needs to be attached to a vertical structure and is generally high maintenance; early examples had seven-day ink chart recording systems. They can also be affected by salinity and temperature differences at estuarine sites during a tidal cycle, so that the water sample contained within the stilling well is seldom compatible in its density with the open water and then only at low tide (Lennon, 1971).

Fixed sensors include acoustic reflection and radar reflection gauges. These have accuracies of between 0.005-0.01m (Pugh et al., 2014) and are deployed to point directly down at the water surface. Acoustic reflection gauges measure the time taken for a pulse of sound to travel from the source to the reflecting surface and back again, and thus the distance can be calculated using the speed of sound in air. They generally perform better when installed within a stilling well or sounding tube to avoid the effect of reflections directed away due to irregular or sloping sea-level surfaces (Pugh et al., 2014). In addition, the results need careful calibration due to the effect of air temperature and air temperature gradients on the speed of sound through air.

Radar reflection gauges work on the same principle as acoustic reflection gauges by timing the reflected signal of a pulse of electromagnetic radiation. Recent versions of this type of gauge have lower power outputs and thus are suitable for solar panels installations (Gobron et al., 2019). In practice they are attached, pointing downwards, at the end of horizonal arms that are themselves fixed to piers or harbour wall structures. Unlike, acoustic radar gauges, radar reflection gauges are not affected by temperature or vertical temperature gradients (Pugh et al., 2014). However, both these types of fixed sensor require significant vertical structure and thus would not be suitable at many coastal locations.

An alternative approach to the above methods, and one that is traditionally used for accurate sea-level measurements, is to measure the pressure at a fixed point below the sea surface and then convert this to a water level using the basic hydrostatic relationship (Pugh, 1972). This pressure can be used to calculate the head of water above the outlet using the following equation:

$$P_m = \rho\, g\, \zeta_i + P_a \qquad (1)$$

where P_m is the measured pressure, P_a is the atmospheric pressure at the water surface, g is the gravitational acceleration, ρ is the water density and ζ_i is the water level. The underwater pressure can be physically transmitted to a shore-based recorder along a narrow tube from a point underwater. An example of this method is the pneumatic system which are often referred to as bubbler gauges or gas-purging gauges and can deliver accuracies of 0.01m (Woodworth et al., 2003). This type of system consists of a narrow tube which extends to an outlet just below low water. Compressed air is then passed down the tube to the outlet where it escapes. At this underwater outlet the gas pressure is equal to the water pressure, and this pressure can be measured at a location where the gas is introduced into the system. Normal practice would be to use a differential pressure transducer which responds to the difference between atmospheric pressure and the water head pressure, and thus only the water head pressure is recorded. These bubbler gauges have the advantage that they can easy be deployed on beaches if the narrow tube can be protected across the surf zone; although it would need to reach beyond the low-water level, which on some tidal flats can be greater than 400m.

1.2.1 Pressure sensors for sea-level measurement

Another variation is the self-contained pressure recorder which is routinely used for offshore sea-level measurements (bottom mounted) and can be mounted alongside harbour structures for coastal sea-level measurements (Martin Miguez et al., 2012). Offshore devices can be levelled in to shore-based datums over short horizontal distances by using other local tide gauge data, and aligning the mean sea-level. In addition, these devices require a local measurement of atmospheric pressure which needs to be subtracted from the recorded pressure. Stand-alone devices without telemetry vary in cost £800-£5000 and this is dependent on the configuration. In addition, some manufacturers also offer telemetry hardware options, which allow near-real-time data to be retrieved via land-line or mobile phone

broadband data connections. Power can either be supplied by mains power or battery/solar panel systems. They can be deployed within the intertidal zone with suitable fixed bottom frames, or at locations where structures are available for attachment e.g., jetties, channel markers, and then levelled in to local datums using a GNSS devices. They are not routinely deployed to support coastal monitoring programmes and currently no low-cost devices (i.e., less £200) are available on the market.

Hi-resolution and low-power pressure sensors have over the last 5 years have been brought to the market place by Measurement Specialties (MS) e.g., MS5803, 2 bar and 5-bar pressure sensors. These sensors have SPI and I^2C communication interfaces which allow connection to suitable micro-controllers for data storage. They are also an inexpensive sensor; in modular form they cost around £4 per sensor. This type of pressure sensor, coupled with a data logger (Arduino microcontroller), has been successfully deployed in underwater cave systems to record fluctuating water levels. These data were shown to be reliable and stable over long deployment periods ~ 6 months (Beddows et al., 2018). Furthermore, these sensors are able to sample pressure at rates up to 10Hz, which would allow detection of higher frequency changes such as that of coastal waves.

While there are a number of commercial tide gauges (which use pressure sensors) many are expensive. For example, the RBR compact tide & wave logger (https://rbr-global.com/products/compact-loggers/compact-tide-wave/) costs upwards of £1000. RBR tide gauges, with quoted resolutions of 1 mm, were used to record the tidal elevations around Bardsey Island, North Wales (Green et al., 2020). In contrast, the low-cost IoT tide gauge developed, and deployed at Liverpool and Crosby Sands, uses a 2-bar pressure sensor with a resolution of 0.16 mm, with an overall build cost less than £100 and this includes near-real time telemetry.

1.2.2 GNSS devices for sea-level measurement

GNSS devices are also used to determine sea-levels directly, either from shore-based installations at the coastline or from devices mounted on buoys or other surface following platforms. GNSS is a generic term which encompasses all satellite networks including the United States Global Positioning System (GPS), the Russian Federation Global Navigation Satellite System (GLONASS), European Union's Galileo and the Chinese BeiDou Navigation Satellite System. They operate at slightly different frequencies, for example, the GPS system operates at three L-band frequencies (L1, L2 and L5), which is a part of the radio spectrum between 1 and 2 GHz (Kaplan et al., 2017). One advantage of using GNSS to determine water levels is that the vertical positional measurement can be directly related to a national vertical datum e.g., UK Ordnance Datum Newlyn (ODN). GNSS receivers which operate at multiple frequencies e.g., L1, L2 and L5, are often referred to as geodetic receivers.

The shore-based GNSS sea-level measuring systems use the interferometric reflectometry technique (Larson et al., 2013); reflected satellite signals (i.e., noise) from the sea surface, as well as direct satellite signals, are picked up by the receiver. Patterns within the signal-to-noise-ratio (SNR) data were shown to be related to the height of the antenna above the reflected surface. Geodetic GNSS receivers have been shown to work very well using this technique (Larson et al., 2017). More recently the technique has been shown to work using a single frequency low-cost GPS receiver (Karegar et al., 2021; Williams et al., 2020). However, the technique delivers the best results when adjacent to water which does not dry out, and when the deployment location can maximise the number of visible GNSS satellites.

Geodetic GNSS receivers have been successfully installed on buoys in both sheltered and ocean settings to determine sea-level (André et al., 2013). However, they are expensive to self-build or to buy commercially, and hence are not routinely used to determine sea-level. Some of the high-end specialist GNSS buoys can cost upwards of £100k, with the GNSS receivers and antennas combinations costing ~£10k. For example, Morales Maqueda et al. (2016) attached a geodetic dual GNSS receiver to a Wave Glider, an unmanned water surface vehicle, and obtained surface height measurements with ~0.05m precision; the receiver and antenna alone cost ~£6k.

Real-Time Kinematic positioning (RTK) is a technique that uses carrier-based ranging and provides ranges (and thus positions) which are more precise than can be derived with code-based positioning. In practice, this requires a fixed receiver (base station) and a moving receiver (rover); the base station (usually a dual frequency receiver) sends corrections to the rover (this can be a single frequency receiver). If the rover can record the raw satellite data then the corrections can be applied later, and this can provide additional precision and is known as Post-processed Kinematic (PPK). In contrast, Precise Point Positioning (PPP) is a positioning method which only uses a dual frequency receiver and relies on direct observables and ephemerides sources of information. Like RTK it also uses the carrier phase and ephemerides, however it also uses the differential delay between GNSS signals of different frequencies to reduce positional errors. Like RTK, post processing of the raw data with the latest ephemerides will improve the positioning.

The advantage of a dual frequency receiver over a single frequency receiver is that the largest errors associated with GNSS timing calculations can be almost eliminated. For example, the ionosphere and troposphere cause the largest errors in timing (ionized particles have a protruding effect on the signals and disrupt them). However different frequencies are affected differently and thus a portion of the ionospheric/troposphere bias can be removed (Brunner et al., 1993; Klobuchar, 1983). These GNSS setups typically use the Precise Point Positioning (PPP) method, where data from a single dual frequency receiver can be used to derive levels of a few centimetres under good conditions.

Another option is to use the real-time kinematic positioning (RTK) method or, if processed later, the Post-processed Kinematic (PPK) method (Pırtı, 2021). This would typically require a base station and

a rover i.e., a fixed receiver, and a moving receiver. These setups are used extensively for land surveys and are very accurate since rover positional errors are corrected using data from the base station. Typically distances between rover and base stations should be less than 20km. A buoy with a suitable GNSS receiver and antenna which if deployed close to the shore would be able to take advantage of the RTK/PPK methodology, and use less expensive single frequency GNSS receivers.

Developments within the GNSS field are moving at a rapid rate with additional satellites being launched as networks improve and expand, and through advances in receiver and antenna technology (European_GNSS_Agency, 2020). For example, low-cost, low-power and small-form receivers are appearing on the market place every few months or so. These devices (i.e., chipsets, modules and receivers) are now being manufactured in very large quantities and are primarily aimed at consumer devices e.g., mobile phones, drones, robotics etc. One example is the U-blox M8T series of GNSS single frequency receivers. The U-blox M8T series has been shown to be capable of centimetre accuracies for land based RTK applications (U-blox, 2016). It can record concurrent GPS, GLONASS, BeiDou and Galileo satellite data up to 5Hz, and up to 10Hz for single GNSS systems such as GPS. It can also record carrier phase output which is a necessary requirement to determine centimetric positional accuracy. Development boards with these GNSS receivers embedded can be bought for less than £100, with the actual receiver chips at a fraction of this cost. An example is the Emlid Reach ("Emlid Reach M+ RTK GNSS module for precise navigation and UAV mapping," 2019) which has been designed for the drone market; it consists of an Edison micro-computer running Linux with an embedded U-blox M8T GNSS receiver.

There are two types of GNSS buoys; those which are capable of measuring waves e.g., Sofar Spotter buoy (https://www.sofarocean.com/products/spotter) and those which are capable of measuring both sea-level and waves e.g., Axys Technologies Hydro Level buoy (https://axys.com/hydrolevel-tide-level-buoy/). For example, the Axys Technologies Hydro Level buoy uses a geodetic GNSS receiver (dual frequency) and costs around £100k, whereas the Sofar Spotter buoy uses a GNSS receiver (single frequency) and costs around £5k (plus a subscription service to access the data). In addition, to illustrate individual GNSS costs, a geodetic GNSS receiver and antenna costing around £6k was fitted to a Liquid Robotics Wave Glider (https://www.liquid-robotics.com/) to produce ~5 cm precision water surface heights for a Scottish lock (Morales Maqueda et al., 2016).

The low-cost GNSS buoy developed here can measure both sea-level and waves, and is based upon a single frequency GNSS receiver; the overall cost is around £300 (buoy parts £100, GPS.logger £200). Subsequent field evaluations produced a RMSE of 1.4 cm, computed from the differences between the GNSS-buoy and a reference tide gauge; this is comparable with other more expense GNSS buoy platforms. The small dimensions of the low-cost GNSS buoy also allow for easy deployment from

small boats, and for beach installations at the low water mark using suitable screw anchors and mooring lines.

1.3 Tidal networks and telemetry

The majority of countries with coastlines have national tide gauge networks e.g., the Environment Agency maintains the UK Tide Gauge Network. This network has forty-four tide gauges spread out around the British Isles coastline covering Northern Ireland, Scotland, Wales and England (EA, 2019b). National tide gauge networks generally record high quality sea-level measurements (between 0.01 m and 0.001 m accuracy), which are suitable for academic sea-level research into sea-level rise (to be included in the Global Sea Level Observing System (GLOSS), tides gauges need to have an accuracy better than 0.01 m (IOC, 2016)). The majority of these tide gauges are located within harbours and at ports, and spread out along the coastline to take account of spatial and temporal tidal variation. They also tend to be associated with a telemetry element to relay data, such as by dial up telephone modem, or more recently connected to broadband internet services via telephone cables or mobile phone 3G/4G data connections. The UK tide gauge network data (unchecked data) are made available in near-real time via the National Tidal & Sea Level Facility (NTSF) website (https://ntslf.org) which is part of the National Oceanographic Centre (NOC, Liverpool). Delayed-mode data are quality checked by the British Oceanographic Data Centre, and these are made available with a 3-month delay.

Port authorities and smaller harbours can also have tide gauges, not connected to the national networks but often available for coastal users to use in near-real time. For, example, Mersey Docks and Harbour Company have a small number of tide gauges covering the entrance to the Mersey Estuary. These are located along the River Mersey estuary (Alfred Lock, Gladstone Lock and Eastham Lock) and on Hilbre Island. Also, in the past decade they have installed another tide gauge on one of the wind turbines at Burbo Bank, located at the main entrance to the River Mersey. This was installed to replace the Hilbre Island tide gauge (15 km to the south west of the entrance to the Mersey). This tide gauge was discontinued due to continued problems with the silting up of the tide gauge well, the subsequent high cost of maintenance, and the distance was considered too far to estimate depths for ships entering the main channel into Liverpool. In the past these gauges used VHF communications, however they now use mobile phone or direct telephone broad band services.

Recovery of oceanographic data in near/real time can be beneficial for a number of reasons. Firstly, regular quality checks can be made and thus problems identified early. If necessary, these devices can then be scheduled to be swapped out at the earliest opportunity. Secondly, port authorities, coastal communities and coastal defence managers often require timely data in order to make decisions and respond to the prevailing conditions e.g., the effect of storm surges, and/or as input to nowcast/forecasting modelling systems (Glenn et al., 2000). Finally, data can be combined with other

data to provide additional products which would otherwise have to be delayed e.g., use of sea-level data combined with X-band radar data and the waterline method to derive morphological maps.

A local network of sensors as part of a coastal monitoring programme would be beneficial since they can provide some duplication against sensor failure. They would also be useful since they can provide the level of detail necessary to monitor and understand complex intertidal zone, estuary system and channels leading to harbours and ports.

1.3.1 Innovative telemetry options for tide gauge networks

With the emergence of Internet of Things (IoT) concept, low power wide area networks, sometimes called gateways, have become available for transmitting and receiving data. An IoT ecosystem consists of smart devices that use embedded systems, such as sensors, processors and communication hardware, to collect and send data they record from their environments. IoT enabled devices share these data by connecting to an IoT gateway where data is sent to the cloud for analysis, or forwarded to localised computer systems. There are currently two main telemetry systems; Sigfox which offers a subscription model, and LoraWAN which offers free access to the network with the expectation that each user group should contribute a base station gateway. Table 1.1 shows the common differences between the two systems. These types of system would be ideal telemetry option for incorporation into both localised and wider area tidal gauge networks.

Table 1.1: Sigfox and LorWAN system comparison

	SigFox	LoraWAN
Bandwidth	100Hz	250KHz and 125KHz
Maximum data rate	100bps	50Kbps
Maximum messages per day	Upload 140, download 4	Unlimited
Maximum payload length	Upline, 12 bytes, Downlink 8 bytes	Maximum payload length is 243 bytes
Range	10km in urban 40km in rural	5km in urban 20km in rural

Both these transmitter/receiver platforms are available on the Arduino MKR microcontroller e.g., Arduino MKR FOX 1200 and the Arduino MKR WAN 1310 LoRaWAN Communication Board. Thus, this provides an opportunity to combine one of these boards with a MS pressure sensor to test the feasibility of creating a low-cost tide gauges capable of scaling up to provide a network.

1.4 Data analysis methods

Welch's method was used to compute an estimate of the power spectral density (PSD) using the high frequency data from the GNSS buoy. The method divides the data into overlapping segments,

computing a modified periodogram for each segment and averaging the periodograms. This was computed using a python script and the "scipy.signal" python API (https://docs.scipy.org/doc/scipy/reference/generated/scipy.signal.welch.html). This allows for interpretation of peaks in the spectral density in relation to frequency and the corresponding wave period. The significant wave heights (where significant wave height is approximately equal to the highest one-third of waves, as measured from the trough to the crest of the waves) were then estimated by calculating four times the square root of the area from under the peak of spectral density (Fiorentino et al., 2019) between the frequency bands 0.5 Hz and 0.125 Hz (equivalent to the variance of the wave displacement time series acquired during the wave acquisition period). The area was calculated with a python script using scipy.integrate.simps (https://docs.scipy.org/doc/scipy-0.15.1/reference/generated/scipy.integrate.simps.html).

1.5 Research goals

The research goals within this thesis are to:

1. Develop and evaluate low-cost sea-level instrumentation for incorporation into routine coastal monitoring programmes using X-band radar; deploy these devices in sheltered and exposed environments and test their resilience and capabilities.
2. To characterise the morphology of a tidal flat using DEMs from LiDAR and derived from X-band radar, and in the process highlight limitations within the archived data, and thus explore how the above instrumentation (in 1.) would improve both temporal coverage and data quality of the X-band radar derived DEMs.

1.6 Thesis layout

The thesis has been written in research paper style with the five main chapters. Three of the chapters (2-4) have already been submitted, accepted and published in scientific journals. Chapter 5 details the analysis of morphological maps, and how the combined temporal X-band data and annual LiDAR data can be used to characterise the morphology of a tidal flat. Chapter 2 is based upon the initial research into using GNSS to measure sea-levels, and the subsequent design and evaluation of a low-cost GNSS buoy platform. It consists of the design and build of the buoy platform, and lays out the choice of the GNSS receiver and logger. The package was then fully evaluated using field deployments and comparisons made with an existing research quality tide gauges.

In chapter 3, two emerging technologies, in telemetry and pressure sensor design, have been merged together to create an "IoT" tide gauge. It develops the idea of using low-cost sensors with micro-controllers and the incorporating pressure sensors. The tide gauge was evaluated at two locations near Liverpool; one close to a research quality tide gauge and attached to a vertical dock wall, and another on a tidal flat, attached to a channel marker post and next to an Acoustic Wave and Current Profiler

(AWAC). In chapter 4, the low-cost GNSS buoy developed in chapter 2 was evaluated on an exposed intertidal location. The research explores the mooring design for this type of deployment, and investigates both the sea-level, and high frequency oscillations caused by waves. Data was compared against the nearest local tide gauge and an offshore wave buoy.

Chapter 5 is based upon developing an understanding of the mechanisms of morphological change as recorded over a three-year period by LiDAR and X-band radar. While analysis using maps derived from LiDAR, GPS surveys and beach profiles is commonly place, using three years of X-band derived maps is a new development. The derived digital elevation models, along with the forcing parameters, such as sea-level and wave data have been used to determine the role of both tides and waves.

Chapter 6 sums up all the results and conclusions within chapters 2, 3, 4 and 5. It also provides discussion on improvements to the developed sensor packages, and how they might be incorporated with the X-band radar to provide an overarching coastal morphological monitoring system.

2 A low-cost GNSS buoy platform for measuring coastal sea levels

This chapter was taken from the published research paper:

Knight, P. J., Bird, C. O., Sinclair, A., & Plater, A. J. (2020). A low-cost GNSS buoy platform for measuring coastal sea levels. Ocean Engineering, 203, 107198. doi:10.1016/j.oceaneng.2020.107198 (see declaration section page 2 for contribution).

2.1 Abstract

A low-cost Global Navigation Satellite System (GNSS) buoy platform was developed for measuring coastal sea levels to provide information where logistical, physical and/or financial constraints prevent the application of established tide gauges and satellite altimetry, and where spatially and temporally discrete tidal data are required to support surveys for monitoring coastal morphodynamics. The buoy was constructed from scaffold tubing and four floats, with a central platform for the GNSS receiver and antenna. The overall cost was around £300 (buoy parts £100, GPS/logger £200). The single frequency GNSS receiver was set up to record GPS/GLONASS satellite data at 5Hz. Post-processing was carried out with RTKLIB software to derive solutions for sea level. GNSS buoy performance was evaluated against a reference tide gauge using a Van de Casteele test. The RMSE of 1.4 cm, computed from the differences between the GNSS-buoy and reference tide gauge, demonstrates that this low-cost GNSS buoy tide gauge compares well with previous, more expensive GNSS buoys and is suitable for obtaining local-scale coastal sea level data. In addition to providing coastal data at cm accuracy, the results also indicate the presence of high frequency oscillations in the sea level data caused by coastal geometry and wave-induced disturbance.

2.2 Introduction

Obtaining local sea level data is a critical challenge for assessing risks to increasing coastal populations, infrastructure, economies and ecosystems, particularly with respect to characterizing environmental response to projected climate change, storms and sea level rise (cf. Nicholls et al., 2007). This is especially important for low-latitude, small island developing states (SIDS) where the economy is highly reliant upon sustainable development in the low-lying coastal hinterland and adjacent waters, both of which are vulnerable to tropical storms and hurricanes (cf. Turvey, 2007). More widely, data on local sea level can be used to quantify biases and errors due to land contamination of satellite altimetry coastal sea level data, to assure safe port operations and navigation, to underpin accurate flood hazard assessment and forecasting, and to facilitate the assessment of coastal response to hydrodynamic forcing (Marcos et al., 2019) and thus has an essential role to play in climate change adaptation. Amongst the technologies available for coastal sea level measurement, GNSS buoy platforms provide an effective means for quantifying local sea level, independent of land level, at cm accuracy (André et al., 2013). Here, we describe the development

and testing of a low-cost GNSS buoy for deployment where local sea level data are required or where tide gauges or satellite altimetry cannot be utilised.

Local sea level data are important for repeat surveys of coastal bathymetry and morphodynamics, which provide essential data on the character of coastal/nearshore change – including quantification of long-term accretion/recession rates, monitoring impacts of engineering interventions and dredging operations, and assessment of response to inter-annual and seasonal variability, and storm forcing (Harley et al., 2011). Furthermore, repeat surveys at smaller spatial and shorter temporal scales provide a foundation for assessing the local implications of global sea level rise projections (Nicholls et al., 2007). Progressing beyond the established application of periodic LiDAR, differential GPS and Unmanned Aerial Vehicle (UAV) surveys, marine X-Band radar allows continuous monitoring of coastal morphology and morphological change over timescales from days to years (Bell, 2008; Bird et al., 2017). Here, the morphology of beaches and tidal flats can be characterised in terms of their instantaneous and long-term behaviours by applying a water-line method (Bell et al., 2016) whereby the advancing and retreating shoreline during the tidal cycle can be assigned an altitude on the basis of the corresponding tidal level. The accuracy of intertidal morphology determined via the water-line method can be significantly improved when combined with tidal data obtained within the radar survey operating (spatial and temporal) window (Bell et al., 2016). For example, applying the radar water-line method with tidal measurements taken from within the survey domain would reduce any spatial or temporal tidal phase issues that might be present between the survey location and the location of the nearest tide gauge. Furthermore, these portable radar systems may be deployed at coastal locations where local sea level data are not readily available or traditional methods of measuring sea levels cannot easily be applied, e.g., no fixed structures such as piers to attach tide gauges. Thus, GNSS buoy deployment for local sea level at cm accuracy provides an important complement to these new survey technologies.

Global Navigation Satellite System (GNSS) is the standard generic term for satellite navigation systems that provide autonomous geo-spatial positioning with global coverage. This term includes, for example, the US Global Positioning System (GPS), the Russian Global Navigation Satellite System (GLONASS), the European Union Galileo system, the Chinese BeiDou system and other regional systems. GNSS buoys for sea level measurement were originally developed for the verification of data from earth-orbiting satellite altimeters (Hein et al., 1990; Rocken et al., 1990). Essentially, a sea level time-series can be obtained from a GPS antenna mounted on a buoy if the height of the antenna phase centre above sea level is known (Kelecy et al., 1994). GNSS systems use the properties of L-band microwave frequencies, e.g., GPS satellites use L1 (1575.42 MHz) and L2 (1227.60 MHz) (Kaplan et al., 2017) to determine geodetic position from appropriate scaling and combination of the L1 and L2 measurements.

In the past decade, considerable progress has been made on the analysis of reflected GNSS data for sea level monitoring (GNSS-R, e.g. (Roussel et al., 2015)) but GNSS geodetic receivers are readily deployed on buoy platforms to measure sea surface heights (Watson et al., 2008). For example, (Apel et al., 2012) and (Frappart et al., 2016)) demonstrated how the technology can be applied to buoys in estuarine and river systems, while (Lin et al., 2017) showed that by using real time kinematic (RTK) positioning technology, accurate measurements of tidal levels from an offshore buoy could be obtained with a root mean square error (RMSE) of less than 10 cm. Another use of kinematic GNSS at sea is for seafloor geodesy were GNSS buoys have been used in combination with seafloor pressure gauges for vertical deformation monitoring (Ballu et al., 2010). Furthermore, Morales-Maqueda et al. (2016) installed a geodetic GPS on a Wave Glider and used kinematic precise point positioning (PPP) to produce ~5 cm precision water surface heights for a Scottish loch. Later, (Penna et al., 2018) used the same Wave Glider configuration with a North Sea deployment and obtained centimetric precision instantaneous sea surface heights, as well as ellipsoidal height estimates and significant wave heights. In another GNSS application, André et al. (2013) compared three geodetic GPS equipped buoys (two recording at 5 Hz and one at 1 Hz) with established radar tide gauge data. They post-processed the GPS data in 'kinematic mode' with respect to a land-based reference station; post-processed kinematic (PPK) mode is an alternative technique to RTK and differs in that the solution algorithms and timing corrections are applied later. The reference station was located around 500 m away from a relatively sheltered coastal location where the buoys were deployed. They concluded that a RMSE range of 1–2.2 cm between the GPS buoys and a radar tide gauge, again evidenced that GPS buoys are suitable for determining coastal sea level. However, Stal et al. (2016) using a similar approach reported an accuracy of 4 cm in a more exposed location and further out to sea. They used a NavCom geodetic GNSS receiver recording at 1 Hz which was fitted to an AXYS Technologies Hydrolevel buoy, with the closest GNSS reference station within 20 km of the deployment. They reported that the data sets suffered noise related to wave heights, and that a significant amount of other noise was present in the positioning solution (see Stal et al. (2016) for further elaboration).

In the examples above, the buoys were fitted with geodetic GNSS receivers and antennas, capable of picking up both the L1 and L2 satellite signals, and recording carrier phase information. These types of receiver can cost between £2000 and £10,000 (GBP), and typically require expensive antennae (~£3000). The advantage of using a L1/L2 receiver is that one of the largest errors (caused by the travel time delays on the satellite signals due to the ionosphere) can be almost eliminated (Kaplan and Hegarty, 2017). Another advantage is that having two simultaneous satellite signals can help in the processing when cycle slips occur in the data (Kaplan et al., 2017). Furthermore, both the L1/L2 signals are necessary for accurate sea level measurements if using PPP methods, for example when processing data from remote ocean deployments, well away from suitable land-based GNSS reference stations. This paper assesses the performance of an inexpensive GNSS buoy for measuring of sea

levels: consisting of a buoy made from readily available parts and a low-priced GNSS receiver and logger, especially as these buoys are intended for deployment in the coastal zone with a potentially high attrition rate. Successful development of this buoy will also have the potential for wider deployment in low and middle income countries where the financial resources for gathering data on coastal hydrodynamics may be limited. First, we compare the derived sea levels with a reference tide gauge, and then investigate the noise in the RTK solutions as reported by Stal et al. (2016). Here, we apply the PPK technique to data from a low-cost U-blox M8T GNSS receiver (U-blox, 2019b) with a Tallysman (TW2741) patch antenna. Although limited to the measurement of the L1 signal, it can record the necessary carrier phase information and is capable of centimetre-level accuracies (U-blox, 2016). As well as the lower cost, single L1 receivers also consume less power, which is an advantage for battery/solar-power based applications. Also, their use in the nearshore zone is complemented by land-based GNSS reference stations with geodetic receivers as part of the overall positioning solution.

2.3 Materials and methods

2.3.1 Buoy design

The buoy (Figure 2.1a) was designed to be easy to construct with 'off the shelf' components (buoy parts total cost ~ £100). The buoy consists of four yellow Polyform Purse Seine floats (BPB Series 4600), four sections of 33 mm diameter aluminium scaffold tubing (three 0.5 m sections and one 1.0 m section), one four-way scaffold connector, two other scaffold tube fittings (one with an eyelet for the mid-section, and one for connecting the mooring line using shackles). The aluminium tubes connect with stainless steel bolts using standard grub-screw holes in the four-way connector, and other fittings as a guide for the drill bit. A black plastic base bolts on to the top of the four-way connector, on which attaches the GNSS package. Each Purse Seine float has a buoyancy capable of supporting a weight of 4.6 kg. The buoy was tested in a local marine lake with different weights to assess the floating profile and its stability in the water. The GNSS receiver electronics and battery (Figure 2.1b) were contained in an IP67/68 waterproof enclosure: BOPLA Bocube (270×125×60 mm). The waterproofing was enhanced using silicon grease on the rubber seals, waterproof tape and flexible sealant for the antenna cable entry.

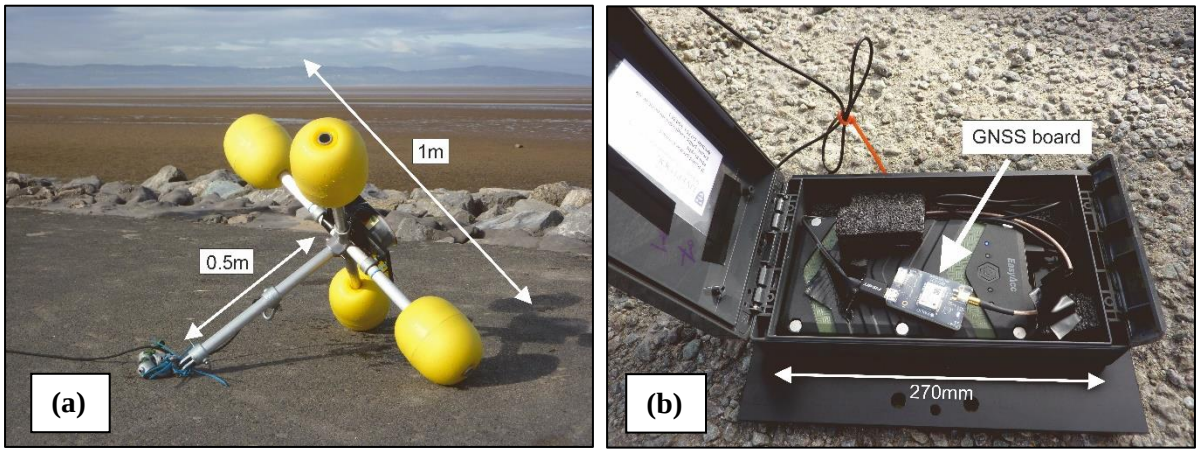

Figure 2.1: (a) Buoy design using standard aluminium scaffold tubing and Polyform Purse Seine floats, (b) GNSS package: Emlid Reach Linux board with embedded U-Blox M8T GNSS receiver and battery pack.

2.3.2 GNSS receiver

The U-blox M8T GNSS receiver was chosen as it is a cost-effective, low power unit (~32 mA @ 3 volts; just receiver) and has been shown to be capable of centimetre-level accuracies (U-blox, 2016) for land-based RTK applications, including built-up areas where satellite signal losses can occur. It is a single-frequency receiver (capable of receiving the L1 satellite signals) that can record concurrent GPS, GLONASS, BeiDou and Galileo satellite data up to 5 Hz, and up to 10 Hz for single GNSS systems such as GPS. In addition, it records the raw satellite data, including the carrier phase output which is required for the centimetre accuracy. An advantage of the buoy being deployed in a marine environment is that visibility of the whole sky will be available; while on many land-based applications, such as car tracking, buildings can obscure and scatter the satellite signals. A disadvantage of marine-based deployments is that they can be affected by large waves; while not proposing an explanation, Stal et al. (2016) reported that noisy data were coincident with large wave heights from a GNSS buoy deployment in the North Sea.

The U-blox M8T receiver was first tested using a U-blox evaluation kit (EVK-M8T) with a GNSS logger, though for field-testing, an early Emlid Reach (("Emlid Reach M+ RTK GNSS module for precise navigation and UAV mapping," 2019); now updated to the Reach M+, with 8 Gb of memory) was used as it had a M8T receiver already embedded onto a small form Linux board (an Intel Edison), WiFi for data transfer, internal storage (2 Gb) and a software user interface that allowed for quick alteration of the receiver settings. The Emlid Reach (costing ~ £200) includes a small Tallysman multi GNSS patch antenna (TW4721), and is mainly aimed at the growing UAV (drone) market. It is a self-contained experimental package (Figure 2.1b) and draws a current of 200–300 mA depending on the set-up and antenna used. The antenna was secured to the top of the enclosure on a 7-cm square steel ground plane. The ground plane is essential to reduce multi-path reflections and increase the antenna

gain (U-blox, 2019a); its optimum dimensions (often supplied with antenna manufacturer's specifications) are determined by the antenna size.

An EasyAcc 20,000 mAh battery pack was used with the Emlid Reach, which provided enough power to cover the experimental period; the expected endurance based upon the power requirements would be up to 4 days. Although not part of this initial experiment further successful trials have been carried out using larger capacity batteries as well as Voltaic Systems solar power panels to allow for extended periods of deployment.

2.3.3 Buoy testing at Holyhead

Holyhead Harbour (Figure 2.2) was chosen as the site for the testing as it has a long-established tide gauge (part of the UK National Tide Gauge Network) and an additional Holyhead Port Authority tide gauge for direct comparisons. There is also a UK Ordnance Survey (OS) geodetic GNSS site

(WGS: 53° 19′ 03.8″N, 04° 38′ 31.4″W, British National Grid: SH 24104 83343) located at the life boat station close to the New Harbour; a source of research-quality GNSS data which can be applied to the PPK solution, and a fundamental benchmark (WGS: 53° 18′ 47.2″N, 04° 38′ 30.0″W, British National Grid: SH 24111 82829). The datum used throughout is local chart datum (CD) which at Holyhead is 3.05 m below Ordnance Datum Newlyn (ODN). At Holyhead the largest tidal range is 6.26 m (National Oceanography POLTIPS-3, 2019). During the test (11–13 September 2018) the highest predicted tide was 6.16 m while the lowest was 0.21 m, and the largest range was 5.86 m. The highest predicted tide of the month was 6.17 m on 10 September at 22:45; the tides were close to the peak springs, decreasing towards neaps.

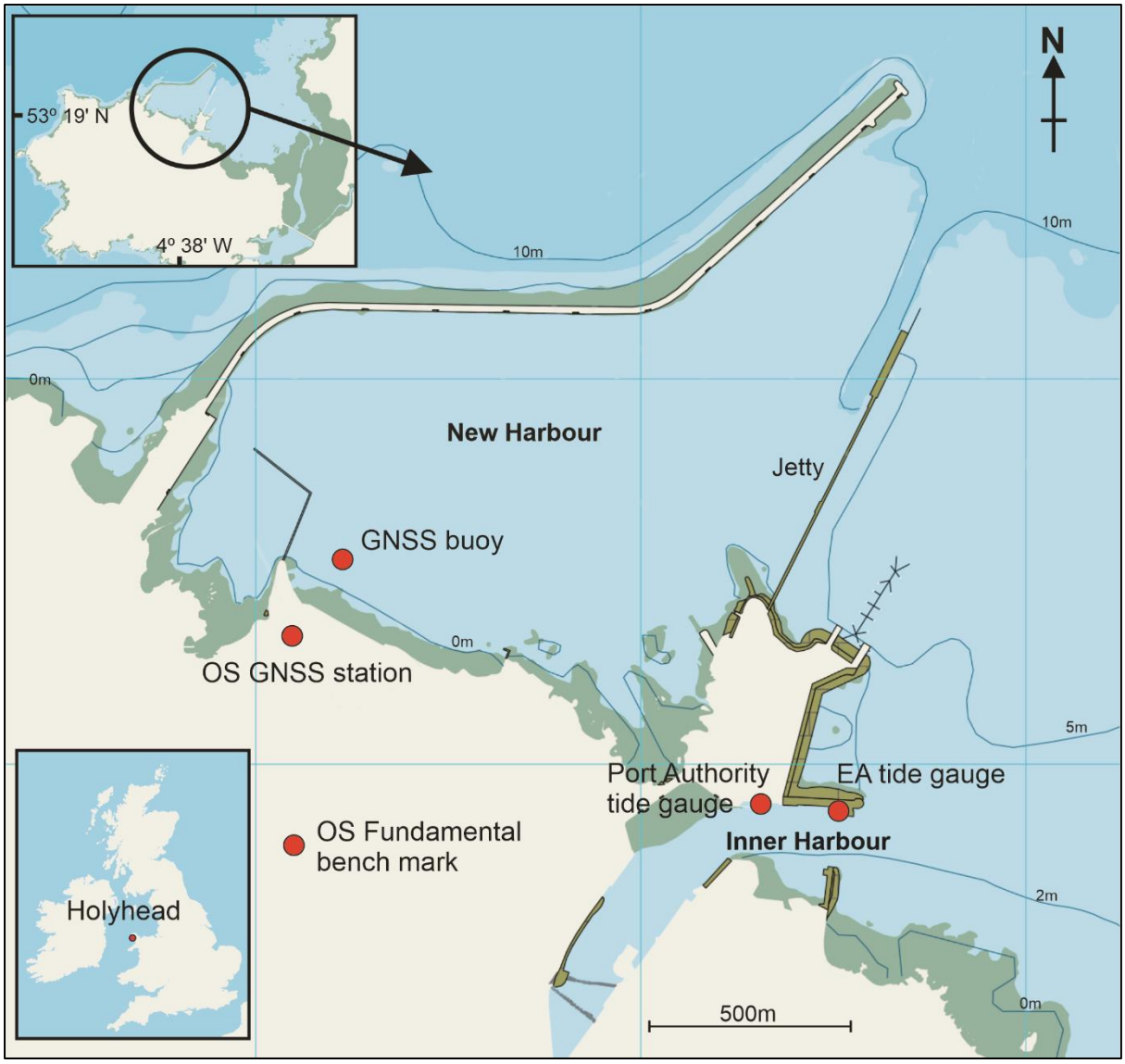

Figure 2.2: Location of Holyhead Harbour (North Wales, UK); GNSS buoy, Ordnance Survey GNSS station, Holyhead Port Authority tide gauge, Environment Agency tide gauge and OS fundamental benchmark. The Jetty is open underneath and allows water to pass between the two harbours, although at low tide it is relatively shallow 1–2 m CD. Base map source: EDINA Marine Digimap Service (http://edina.ac.uk/digimap).

The test took place in the New Harbour (Figure 2.2) where the buoy was attached to a mooring buoy (Figure 2.3) and allowed to float freely (deployed position: WGS: 53° 19′ 08.4″N, 04° 38′ 24.0″W). Charts indicated the mooring location was in about 4 m water depth below chart datum. The U-blox M8T receiver embedded on the Emlid Reach using a Tallysman patch antenna was set up to record GNSS data at 5 Hz; GPS and GLONASS raw satellite data were recorded, including the carrier phase information in the U-blox binary format (ubx). Data were recorded from 10:00 on 11 September until 09:51 on 13 September, with a gap of 42 minutes (09:35–10:17) on 12 September during a data download test and battery check.

Figure 2.3: GNSS buoy attached to mooring buoy in Holyhead New Harbour.

2.3.4 GNSS data processing

To obtain accurate positions using a moving single-frequency receiver (U-blox M8T), data from another GNSS at a known fixed location are needed (ideally recording both L1 and L2 frequencies), for both RTK and PPK solutions. The open source software (RTKLIB, 2018) was used for processing the GNSS data. The advantage of PPK over RTK is that the solution can be applied both forwards and backwards in time, and additional corrections for the satellite clocks and orbits can be included as they become available after a few weeks (see below for further details), thus improving the overall positional solution.

Here, the U-blox M8T is the moving rover (the buoy moving in vertical and horizontal directions at the mooring) and the reference OS GNSS is the base station. Optimal solutions for the PPK are obtained as the distances between the rover and base station reduce to within 20 km of each other, thus these have been kept as short as possible for the experiment

At Holyhead, the distance between the buoy and the reference OS GNSS station was about 200 m (Figure 2.2). The OS GNSS station comprises a Trimble Alloy GNSS receiver (capable of receiving the L1 and L2 satellite signals) combined with a Leica AR25 GNSS antenna and data were downloaded from the OS online download facility (Ordnance Survey, 2019). These data are initially available at 30-second intervals and used for initial PPK processing, however, once the 1 Hz data are

available (delay of 45 days) these were used in the final positioning solution. The archived 1 Hz GNSS data were obtained from the British Isles continuous GNSS facility BIGF (2018).

The processing uses RTKLIB on data spans of up to six hours (to be within software memory limits); the parameter settings for the software are listed in Table 2.1. They are mostly the default settings for RTKLIB with recommendations from other groups (for example, Emlid Reach, 2019). They are similar to the optimised settings of Stal et al. (2016) except that 'Sensor dynamics' was switched to ON and GLONASS satellites were used, both of which improve the derived solution. These parameters were used to obtain the best solution for each data period based on the returned RTKLIB solution quality indicators (see RTKLIB manual: (RTKLIB, 2018)).

To improve the overall solution, satellite ephemerides for precise orbit corrections and satellite and station clock error corrections were applied. These were obtained from the Crustal Dynamics Data Information System (CDDIS, 2018; Noll, 2010). The corrections are delivered with increasing accuracy in the form of 'ultra', 'rapid' and 'final' correction files; available between 3–9 hours, 17–41 hours and 11–17 days, respectively. The results in this paper use the final products.

The GNSS measurements are referred to an 'antenna phase centre': a non-constant value that depends on the direction of the satellite signal i.e., corrections need to be applied during the processing. Within the RTKLIB software package, which outputs the positional data (i.e., including the sea level), there is an option to apply these corrections by including models of the 'antenna phase centre'. These models are available for many of the geodetic antenna types, including the Leica AR25 (base antenna), although not for small low-cost patch antennas such as the TW4721 (rover antenna). Thus, during the processing, the corrections were applied for the Leica AR25 antenna, but not for the TW4721 antenna. Tallysman (Tallysman, 2019) provides some antenna performance documentation for the TW4721 which suggests that the 'antenna phase centre' variations fall in a range of 1 cm.

Table 2.1: Parameter settings for the post-processing using RTKLIB

Parameter	Value
Solution	Kinematic
Frequency	L1
Sensor dynamics	On
Earth tides	Off
Ionosphere	Broadcast
Troposphere	Saastamoinen
Ephemerides	Precise
Satellite system	GPS + GLONASS
Ambiguities GPS	Fix & Hold / Continuous
Ambiguities GLONASS	Off

2.3.5 Local tidal data

Tidal data for comparison with the GNSS buoy results were from the Environment Agency (EA) tide gauge (WGS: 53° 18′ 50.2″N, 04° 37′ 13.6″W, British National Grid: SH 25529 82870) downloaded from British Oceanographic Data Centre (BODC) website www.bodc.ac.uk, and the Holyhead Port Authority's tide gauge (verbal and email communication with the harbour master; WGS: 53° 18′ 50.5″N, 04° 37′ 29.5″W, British National Grid: SH 25233 82889), both in the Holyhead Inner Harbour (Figure 2.2). The EA tidal data were recorded as 15-minute averages, while the Port Authority tidal data were recorded as one-minute averages. The EA gauge is part of the UK National Tide Gauge Network (UK Coastal Monitoring and Forecasting, 2015) and is the reference tide gauge for this experiment (as BODC monitor the data quality). It consists of a full tide bubbler tide gauge system (Woodworth et al., 2003).

2.4 Results

2.4.1 GNSS-derived tidal heights and local tide gauge data

Selected comparisons from the data are displayed in Figure 2.4 a–e: derived tidal heights to chart datum from the GNSS buoy (5 Hz), Environment Agency tide gauge (15-minute averages) and filtered GNSS data (boxcar 15-minute moving averages). GNSS data quality is good, with an exception that occurred on 11 September 2018 (23:02–23:10), as illustrated in Figure 2.4e. The discontinuity was present when the GNSS receiver recorded fewer quality satellite fixes, hence more uncertainty in the derived position. As the harbour is used 24 hours a day and seven days a week, any port traffic nearby could potentially cause 'shadowing' as boats may block some of the satellite signals.

The Figures 2.4a–b also show higher frequency signals in the 5 Hz GNSS-derived sea levels (which will be explored in detail in following sections), oscillations of around 10–30 minutes (which can be attributed to harbour oscillations) and higher frequency oscillations of less than one minute (for example, see Figure 2.4a around high water). Figures 2.4c–d show that while the higher frequency oscillations are present in the 5 Hz data, the harbour oscillations are not obvious and seem to have disappeared.

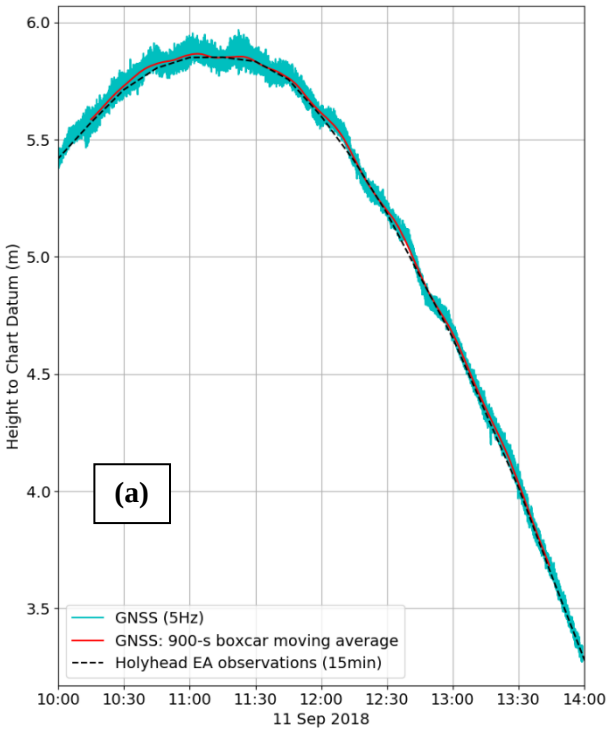

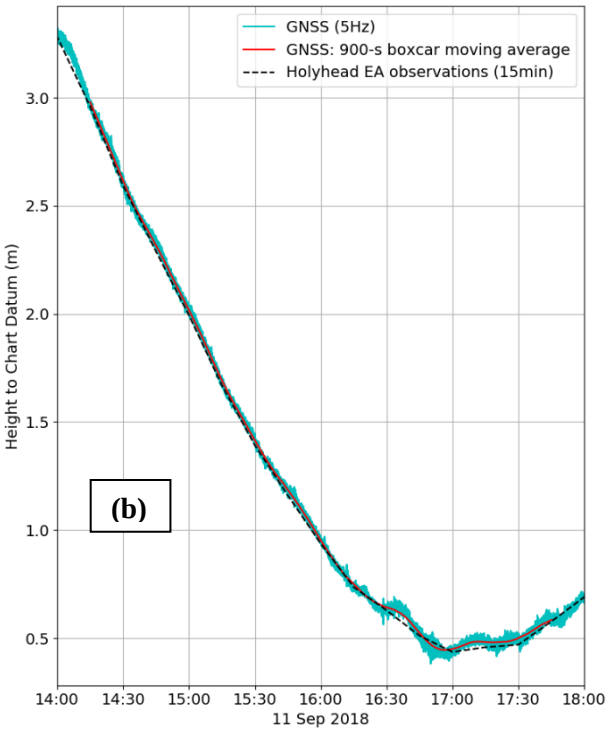

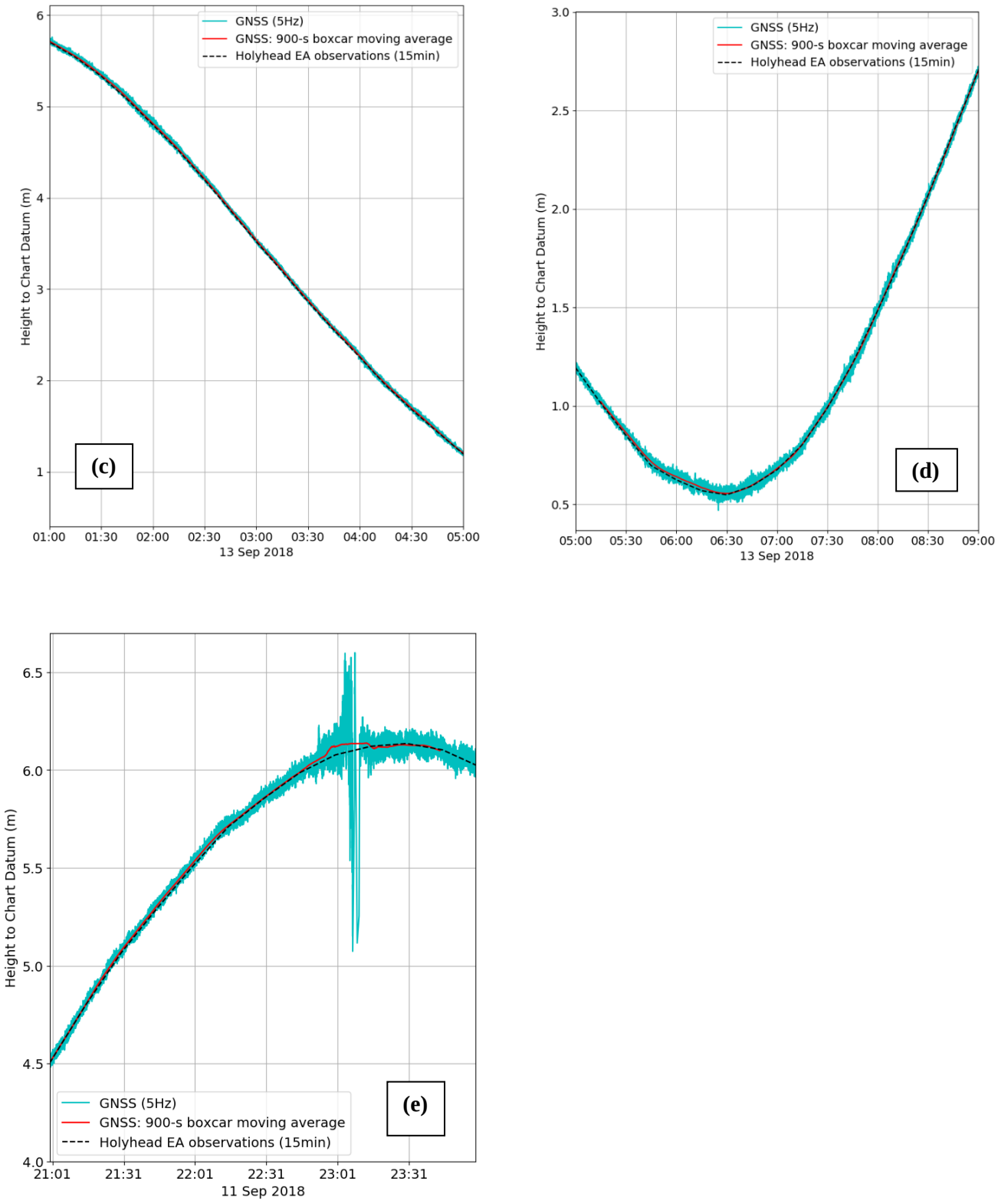

Figure 2.4: Holyhead tidal elevations (a) 11 September 2018 10:00–14:00, (b) 11 September 14:00–18:00, (c) 13 September 01:00–05:00, (d) 13 September 05:00–09:00, (e) 11 September 21:00 – 23:59 (to illustrate discontinuity 23:02-23:10); GNSS (5 Hz), GNSS (900-s boxcar moving average) and EA tide gauge (15 minute)

2.4.2 The Van de Casteele Test

The performance of a tide gauge can be assessed using the Van de Casteele Test. Miguez et al. (2008, 2012) tested a variety of tide gauges and demonstrated the ability to highlight different types of tide gauge error, while André et al. (2013) used it to compare data from three different GNSS buoys for measuring sea level against a nearby radar tide gauge. The method compares a reference tide gauge data set (data known to be an accurate measurement of sea level) to contemporaneous data from the tide gauge being tested (H'): the reference sea level data (H) are plotted on the ordinate against the tide gauge difference (ΔH) on the abscissa (x-axis), where $\Delta H = H - H'$. The resulting diagram would produce a straight vertical line centred on $x = 0$ for a perfect match between the two tide gauges.

2.4.2.1 Assessing the GNSS buoy tide gauge accuracy

Before comparing the GNSS data with the EA tide gauge data, a 900-s boxcar moving average was applied to the GNSS data, and then values corresponding to the timings of the EA gauge data were resampled at fifteen-minute intervals. The resulting Van de Casteele diagram in Figure 2.5a indicates good agreement between the EA tide gauge and the GNSS buoy tide gauge. The near vertical alignment in the chart of the differences between low water and high water, although not perfectively straight, implies that there are no timing offsets (which would result in a more ellipsoidal pattern) and no obvious systematic errors (e.g., scale error; which would have introduced a large gradient from low water to high water), however there is a small overall negative offset from zero. This bias shown in Figure 2.5a may be partly due to the spatial difference between the two tide gauges, and/or due to errors in the measurement of the antenna elevation above the water surface. The mean difference between the GNSS data and the EA tide gauge data was −0.011 m, the standard deviation was 0.009 m and the RMSE was 0.014 m. Some of the larger residuals are due to the presence of the harbour oscillations which are noticeable in the 900-s boxcar averaged GNSS data (Figure 2.4a), that are not represented in the 15-minute EA tide gauge record. These differences may be the result of wave damping that has been introduced within the design of the EA tide gauge bubbler system.

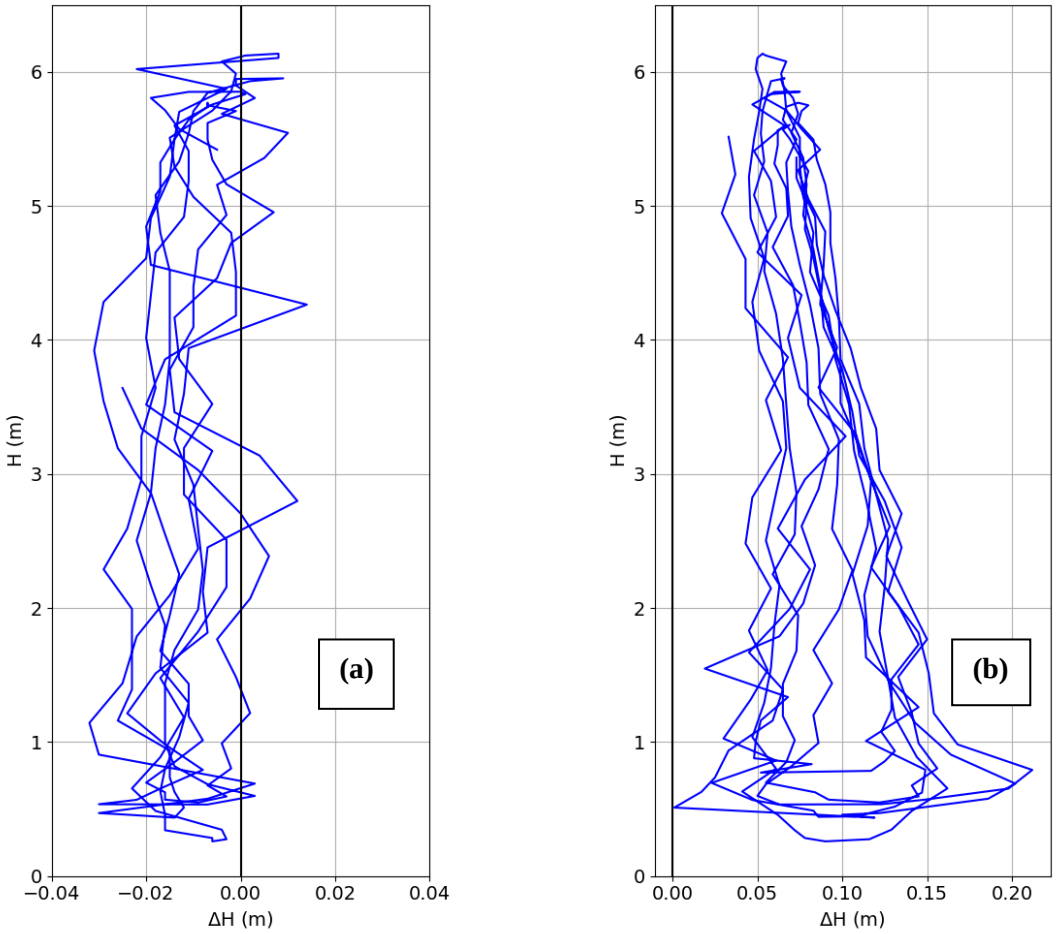

Figure 2.5: Results of the Van de Casteele Test for (a) GNSS buoy 15-minute averages using the EA tide gauge as a reference: differences between EA tide gauge and GNSS buoy tide gauge (ΔH) plotted against reference tide gauge (H), (b) Port Authority tide gauge 15 minute averages using the EA tide gauge as a reference (for comparison). Note: Horizontal scales are different.

Figure 2.6 plots the tidal differences against time (left axis) alongside the EA tide gauge observations (right axis). The time series of differences between tide gauges (ΔH) produces a tide-shaped sinusoid, which is mildly correlated with the tidal cycle; this translates into the small slope (from high tide to low tide) that is evident within the Van de Casteele diagram (Figure 2.5a), thus indicating that the GNSS buoy tide gauge is performing well (cf. Miguez et al., 2008).

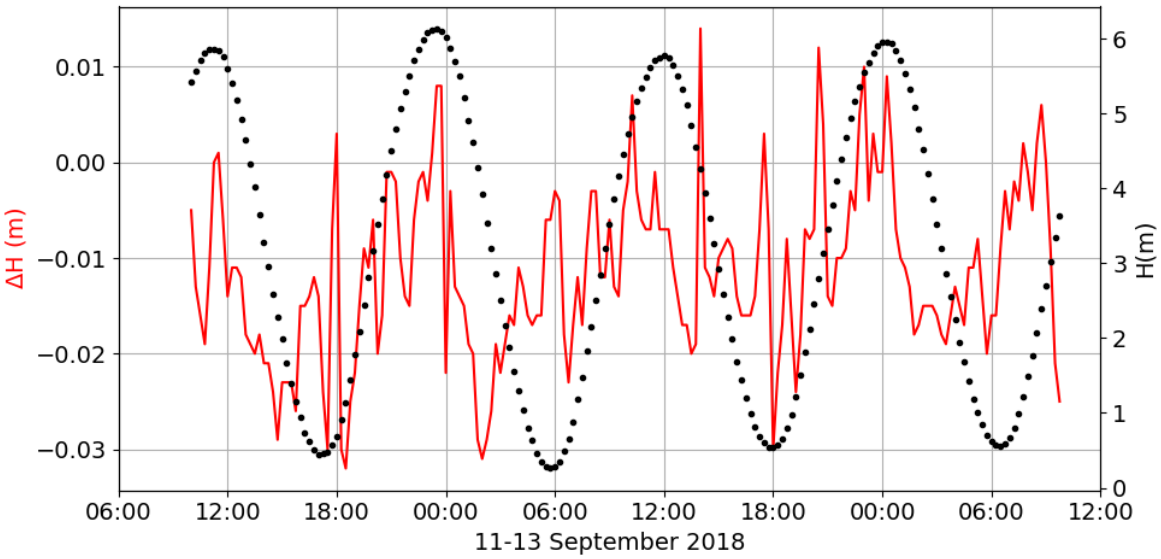

Figure 2.6: Results of the Van de Casteele Test for the GNSS derived sea level data using the EA tide gauge as a reference: time series of tide gauge differences (ΔH, solid red line) and EA tidal observations (H, black dots).

2.4.3 Harbour oscillations

To examine the above-mentioned oscillations (with periods of between 10 and 30 minutes) seen in the 5 Hz data (Figure 2.4a), data from the Port Authority tide gauge (recording one-minute averages) were compared to the GNSS-derived sea level data. After applying the Van de Casteele Test (described above) to the Port Authority tidal data using the EA tidal data as the reference, the test results highlight three issues with the Port Authority tide gauge: a general datum offset, a gradient (away from vertical) in the Van de Casteele Test diagram (Figure 2.5b) from high water to low water, and large differences at low water. The mean difference was 0.086 m, the standard deviation was 0.034 m and the RMSE was 0.092 m. However, these data confirm the presence of harbour oscillations seen within the GNSS data (Figure 2.7a–b), which can be seen clearly across the high water period: 11 September 2018 at 10:00–13:00 and to a lesser degree across the high water period: 12 September 10:30–13:30. It is interesting that these oscillations are reduced in amplitude and appear to be at a different frequency during the high water period 24 hours later.

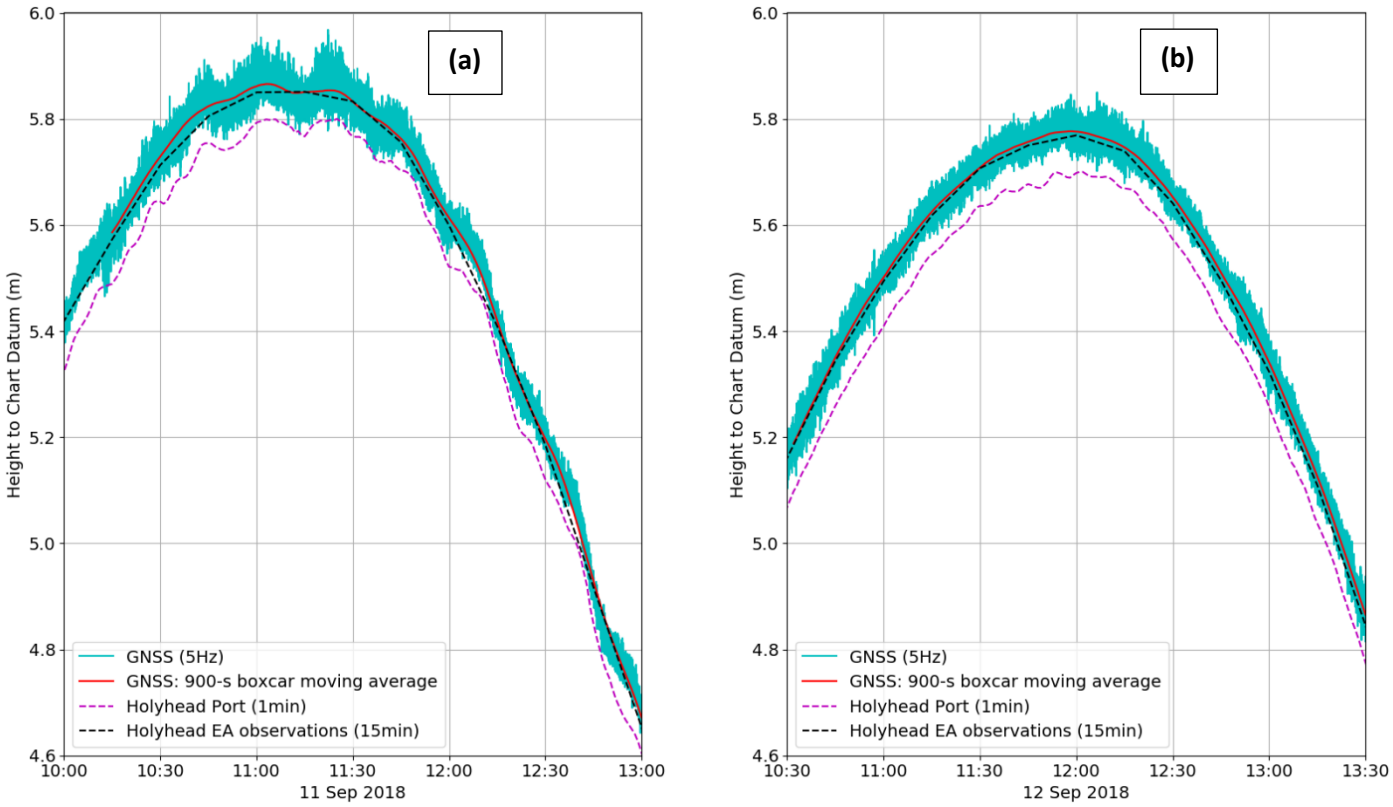

Figure 2.7: Holyhead tidal elevations during (a) 11 September 2018 at 10:00–13:00, (b) 12 September 10:30–13:30. GNSS (5 Hz) in cyan, GNSS (1 minute) in red, Port Authority tide gauge (1 minute) in magenta and EA tide gauge (15 minutes) in black.

The power spectral density (PSD; using Welch's method) of the 5 Hz GNSS data (in Figure 2.8) indicates the presence of oscillations at frequency peaks across the 10–30 minute band. Between 10:00–13:30 on 11 September, the oscillations have a period of around 22 minutes, while 24 hours later between 10:30–13:30 on 12 September the oscillations appear to have periods of 15 and 22 minutes; both have similar spectral density. There appears to be more energy in the 10–30 minute band spanning the high water on 11 September than on the corresponding high water on 12 September.

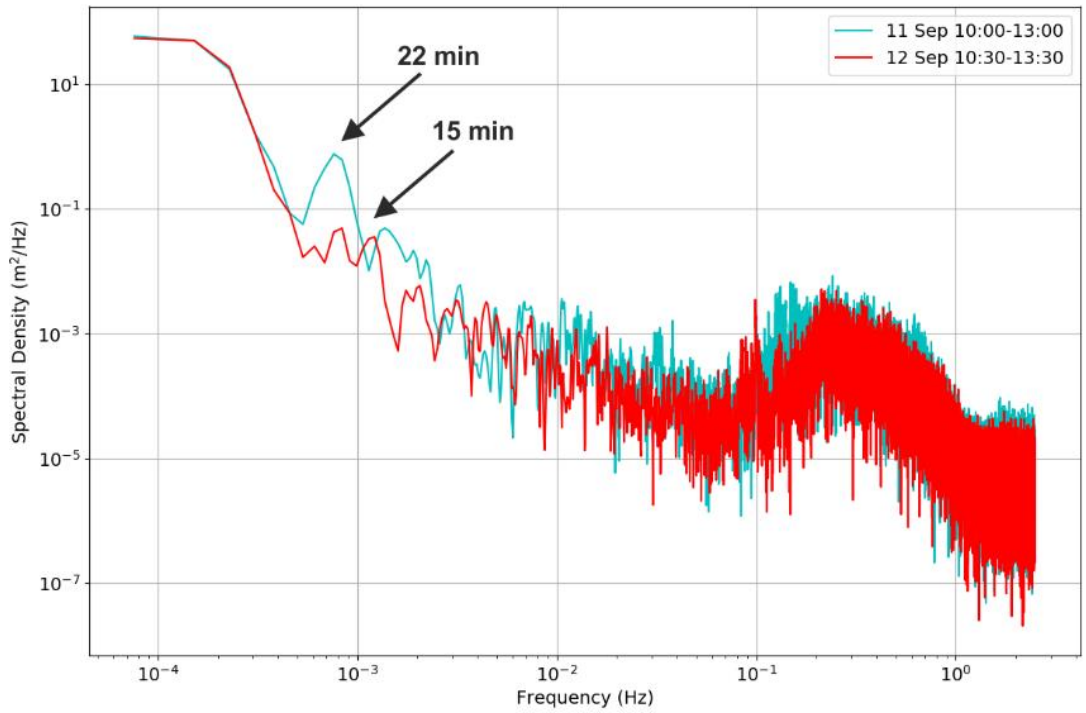

Figure 2.8: Power spectral density (PSD) for the 5 Hz GNSS-derived sea level data for two 3-hour periods around high water. 10:00–13:00 on 11 September 2018 in cyan, and 12 September 10:30–13:30 in red.

2.4.4 Higher frequency oscillations

Oscillations contained within the GNSS data with periods shorter than one minute (frequencies higher than 0.0167 Hz) were explored. As well as noise introduced by the GNSS system and PPK solution method, other potential sources of the high frequency oscillations are the responses to external waves across the harbour entrance, ferry movements, and pitch and roll motion induced by response of the buoy platform to sea surface waves.

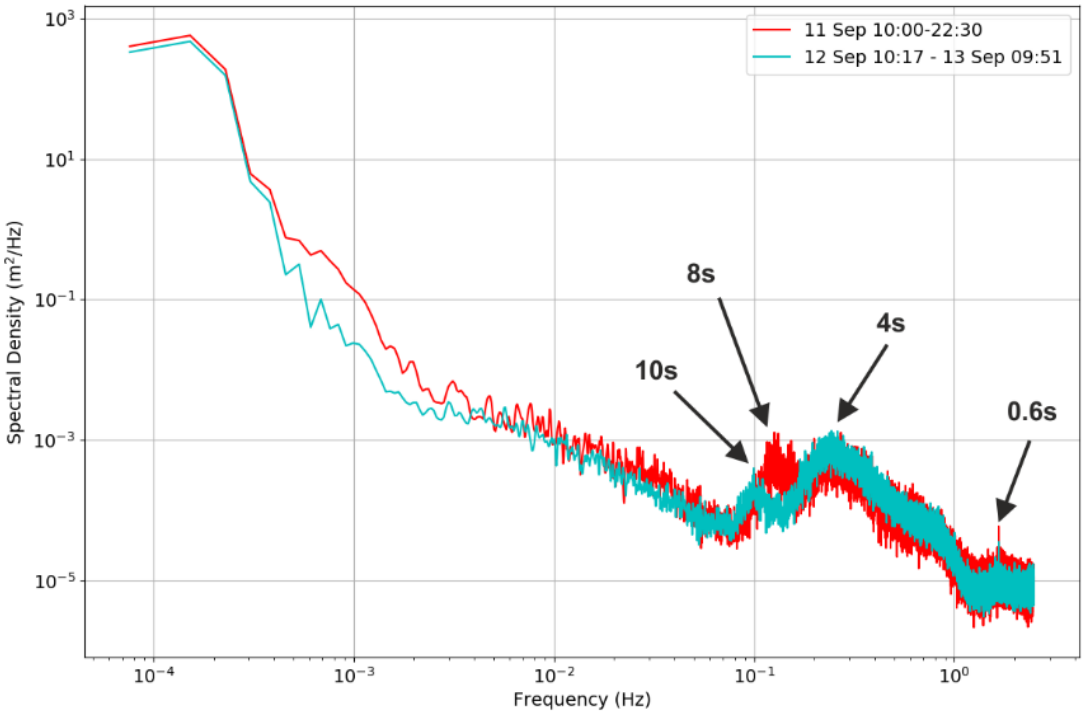

Figure 2.9: Power spectral density (PSD) for the 5 Hz GNSS-derived sea level data for 11 September 10:30 – 12 September 09:35 in cyan, and 12 September 10:17 to 13 September 09:51 in red. Note the first period is shorter so as to avoid contaminating the spectra from the poor quality data on 11 September (23:02–23:10).

Figure 2.9 shows the power spectral density of the 5 Hz GNSS-derived sea level data for the periods 11 September 10:30 to 12 September 09:35, and 12 September 10:17 to 13 September 09:51. The first period is shorter in order to avoid contaminating the spectra from the poor quality data on 11 September (23:02–23:10). There are peaks at 10 s, 8 s, and 4 s periods, which point to the presence of appreciable wave activity in the New Harbour complex. A possible cause of the waves could be the wakes of Irish Sea ferries (with an extensive daily schedule to and from Ireland) and other port traffic. On each day of the deployment, there were twenty evenly spread departures and arrivals; the longest gap with no scheduled ferry service was 3.5 hours, although the ferry arrival/departure times were not always consistent with the schedule (visual note made during deployment) and other traffic were using the port. The results are consistent with other studies on ferry wakes, for example Soomere (2005) observed groups of waves created by a fast ferries operating in the Baltic Sea with periods of 9–15 s, 7–9 s and 3–4 s.

2.4.5 Uncertainty in the derived sea level solution

The GNSS-derived sea level solution contains uncertainty related to the processing method in ‘kinematic mode’, which manifests itself as resembling noise (see section 2.3.4 on data processing). To investigate this contribution and ascertain its likely effect on the derived solution, another identical

U-blox M8T receiver and antenna were positioned on the fundamental benchmark (FBM) at Holyhead for one hour, coincident with a buoy deployment. The RTKLIB software was then applied, with the parameters listed in Table 2.1, to obtain the vertical levels, and once again using the Ordnance Survey GNSS data as the base station. Applying the solution parameter of 'kinematic' to a receiver on a fixed point (stationary) would therefore quantify the processing noise within the kinematic solution. To compare the results, the solution parameter of 'static' was also applied to the GNSS M8T receiver data at the FBM reference station.

The power spectral densities for the three situations are shown in Figure 2.10. It confirms the presence of high frequency components in the GNSS buoy results (see section 2.4.4). When compared with the GNSS results at the FBM, the spectra support the hypothesis of locally generated waves within the New Harbour. The two FBM power spectra highlight the differences in the solution due to the chosen processing options ('static' and 'kinematic') with the static solution having much lower energy. Differences between the mean of each FBM solution (static, kinematic) is small (less than 1 cm), and the corresponding standard deviations for each time series are 0.0024 m and 0.0097 m, respectively. Also, there is a peak of around 1 s period within the FMB (Kinematic mode) solution (Figure 2.10). This may be an artefact of the RTKLIB processing software and how it copes with two different sampling rates for base and rover e.g., the GNSS buoy recorded at 5 Hz and the OS GNSS station data were recorded at 1 Hz.

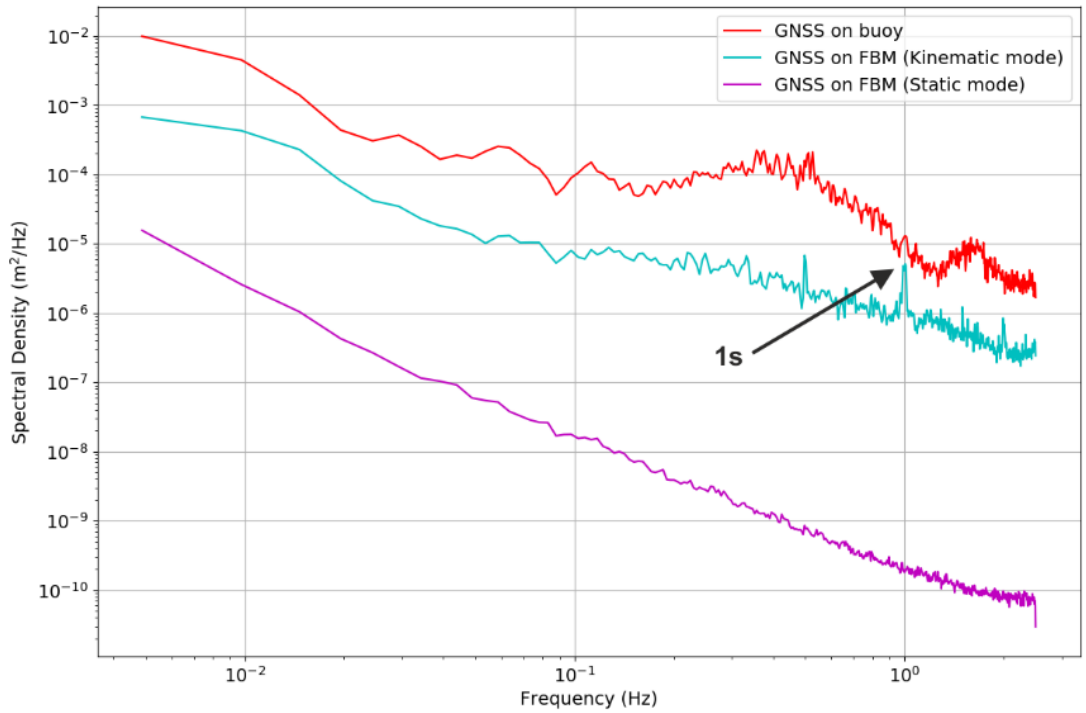

Figure 2.10: Power spectral density (PSD), 5 Hz GNSS-derived vertical data for a one-hour period for a GNSS U-blox M8T located at a fixed point (the fundamental benchmark, FBM) using 'static'

mode (magenta line) and 'kinematic' mode (cyan line), and on the buoy in 'kinematic' mode only (red line).

2.5 Discussion and conclusions

A test deployment of an experimental buoy fitted with a GPS system (U-blox M8T GNSS receiver) for measuring coastal sea level has been undertaken in Holyhead Harbour, Wales, UK. The GNSS receiver recorded two days of 5 Hz data between 11 and 13 September 2018, encompassing four high waters and four low waters. The Van de Casteele Test results, comparing the GNSS positioning solution with the local EA tide gauge (part of the UK National Tidal Gauge Network), gave a mean difference of around 1 cm (RMSE 1.4 cm), thus confirming that this low-cost GNSS buoy tide gauge can produce coastal sea level measurements that are comparable with previous deployments of more expensive GNSS buoys for the same purpose (e.g., André et al., 2013; Rocken et al., 1990). The 1 cm difference may be due to many factors including the instruments themselves, tying errors and the way the subsequent data are analysed. For example, the uncertain 'antenna phase centre' on the Tallysman TW4721 antenna could produce errors up to 1 cm, as specified in the antenna documentation and, indeed, inferred from previous studies (Kelecy et al., 1994; Marcos et al., 2019). Using similar antennas for base and rover receivers would almost eliminate this problem, if the base site is first established using a geodetic GNSS receiver, and in combination with a short baseline. Also, the differences could arise from the different hydrodynamics between the New Harbour and the Inner Harbour; i.e., there is a separation of 1500 m between the GNSS buoy and the other tide gauges, with the added complexity of a jetty (which is open underneath) separating the New Harbour from the outer basin and Inner Harbour (Figure 2.2). Furthermore, the uncertainty within the kinematic solution may result in a bias, although the experiment at the FBM reference station using both static and kinematic solutions suggest that this is smaller than 1 cm.

The observed harbour oscillations in the GNSS and Port Authority tidal data are likely to be seiches (Pugh et al., 2014; Rabinovich, 2010) that can be set in motion by external forces such as wave energy impinging on the harbour, wind, tide, and so on. Using Merian's formula, where the basin is open at one end, and with the length of the bay corresponding to one-quarter of a wavelength, the natural period for the basin is $\tau = 4L(gD)^{-½}$, where L is the length of the harbour, D is its average depth, and g is acceleration due to gravity. Considering the New Harbour, with L=1800 m and D=9 m the calculated period becomes 13 minutes, which is similar to the observed periods of 15 and 22 minutes (Figure 2.8). Likewise, for the Inner Harbour (which is dredged to a 5.5 m minimum depth; with L=800 m and D=8 m), and the whole basin (i.e., the area of water contained within the seawall and the land towards the east (Figure 2.2), with L=3700 m and D=10 m), the corresponding periods are 6 minutes and 25 minutes respectively. These observed oscillations (Figure 2.7a, Figure 2.8) may be related to tidal forcing since the deployment was at, or just after the peak spring tides.

The higher frequency oscillation peaks at ten, eight and four second periods shown in Figure 2.9 are most likely caused by waves induced by the busy port traffic, e.g. ferries to and from Ireland. As mentioned previously these periods are consistent with other studies on ferry waves (Soomere, 2005). The pitch and roll of the buoy with local wind induced wavelets appear to be at much higher frequencies (visual assessment of the buoy on mooring), and this is what is possibly represented as the small peak in the PSD beyond 1 Hz e.g., approx. 0.6 second period (Figure 2.9). Whilst this may be regarded as a complicating factor in the evaluation of the GNSS buoy for measuring sea level, it highlights the further potential for this instrument for capturing data on local wave climate (cf. Hein et al., 1990; Kelecy et al., 1994).

Over the last decade using GNSS receivers on buoys to measure sea levels has been prohibitively expensive when compared to other methods, and thus they have mainly been used for specific scientific purposes. However, recently the overall cost for 'geodetic quality' GNSS receivers and antennas and associated loggers has fallen dramatically and these low-cost packages can now deliver centimetre-level accuracy. For example, U-blox now offer a new dual frequency receiver (e.g., ZEP-F9P) with a similar cost to the U-blox M8T used in this experiment. Furthermore, there are additional GNSS systems such as Galileo becoming fully operational, a new carrier frequency (e.g., L5), which when combined with advances in GNSS receiver software will help to reduce errors and improve the overall positional results. Consequently, the low-cost GNSS tide gauge buoy developed herein offers considerable potential for multiple deployments within survey domains and for addressing information gaps in our global network of tide gauges for monitoring coastal sea level. This potential is enhanced by the GNSS buoy tide gauge's compact size, permitting 'single person' deployment, and its low cost making it attractive for use in low and middle income countries where financial resources for environmental monitoring are limited.

2.6. Acknowledgements

The authors would like to thank Holyhead Sailing Club for access to moorings and boat support during the experiments, Holyhead Port Authority for supplying tidal and meteorological data, the British Oceanographic Data Centre for providing UK Environment Agency tide gauge data, and Dave Jones and colleagues at the UK National Oceanography Centre for technical help and advice. Also, the services of the Natural Environment Research Council (NERC) British Isles continuous GNSS Facility (BIGF), www.bigf.ac.uk, in providing archived GNSS data (and/or products) to this study are gratefully acknowledged. The research is part of a PhD study funded by the 'Low Carbon Eco-Innovatory (LCEI) - Liverpool University' (https://www.liverpool.ac.uk/environmental-sciences/working-with-business/), with industrial partner MM Sensors Ltd. This paper is a contribution to work package 4 of the UK NERC-funded BLUEcoast project (NE/N015614/1).

3 Testing an “IoT” Tide Gauge Network for Coastal Monitoring

This chapter was taken from the published research paper:

Knight, P., Bird, C., Sinclair, A., Higham, J., & Plater, A. (2021). Testing an “IoT” tide gauge network for coastal monitoring. IoT, 2(1), 17-32. (see declaration section page 2 for contribution).

3.1 Abstract

A low-cost ”Internet of Things” (IoT) tide gauge network was developed to provide real-time and “delayed mode” sea-level data to support monitoring of spatial and temporal coastal morphological changes. It is based on the Arduino Sigfox MKR 1200 micro-controller platform with a Measurement Specialties pressure sensor (MS5837). Experiments at two sites colocated with established tide gauges show that these inexpensive pressure sensors can make accurate sea-level measurements. While these pressure sensors are capable of ~1 cm accuracy, as with other comparable gauges, the effect of significant wave activity can distort the overall sea-level measurements. Various off-the-shelf hardware and software configurations were tested to provide complementary data as part of a localized network and to overcome operational constraints, such as lack of suitable infrastructure for mounting the tide gauges and for exposed beach locations.

Keywords: tide gauge network; Internet of Things; beach morphology

3.2 Introduction

3.2.1 Beach Morphology Changes

Understanding morphological change in the intertidal zone is important for coastal flood management (Scott et al., 2016), as beaches often provide the first defence against extreme sea levels and waves. Beaches offer natural coastal protection and can reduce some of the impact of high tides with storm surges and waves (Hanley et al., 2014; Walvin et al., 2015).

Beaches are dynamic and under constant change; the overall sediment load tends to move onshore in the summer and offshore during the winter. In addition, large single event storms can move significant amounts of sediment along and across a coastal frontage (Russell, 1993). In these vulnerable locations, it is common practice for coastal engineers to regularly monitor sediment transport and sedimentation, using survey methods such as beach profiles and spatial surveys with mobile GPS devices, photography and video, and LiDAR surveys (Klemas, 2011), which can be costly and time-consuming.

A recent technique developed by Bell et al. (Bell et al., 2016) applies the “waterline method”’ to a set of marine X-band radar images to produce a time-series of spatial and temporal images equivalent to digital elevation models (DEMs). The accuracy of intertidal morphology obtained by this “waterline method” can be significantly improved when combined with tidal data obtained from within the radar

survey operating (spatial and temporal) window. The advantage of this technique is that it is relatively inexpensive to install and can provide a detailed picture of the daily and weekly morphological changes within the intertidal zone, and thus supports strategic planning and management of coastal defences. Indeed, these types of data can help identify where sections of the beach have changed and provide information to determine the best time to intervene with beach replenishment schemes (Elko et al., 2021).

An "Internet of Things" (IoT) tide gauge network will be capable of providing accurate sea-level data, be portable and easily deployed. It should also be low cost so as, for example, to provide redundancy in case of failure and loss and supplement any existing local tide gauges. Furthermore, IoT-enabled devices using an ultra narrowband wide area network such as Sigfox would provide low-power communication and transfer of data.

Therefore, developing a low-cost tide gauge network that is easy to deploy, is necessary to support routine monitoring of the coastal morphology, for example, in combination with X-band surveys. The near-real-time data aspect of the tide gauge network allows rapid production of morphological maps for coastal engineers to quickly identify significant changes (in the sediment distribution, particularly after storms) and timely identification and notification of faults in the network. Furthermore, this type of low-cost tide gauge network could supplement other regional tidal gauge networks, including those for safe port navigation (Metters et al., 2017) and for tsunami/surge detection (Joseph et al., 2006), and has the potential to provide enough spatial tidal data to fully understand complex coastal locations, e.g., macro-tidal estuaries.

3.2.2 Sea-Level Measurements

There are several methods of measuring sea levels, which can be categorized into three types, surface-following devices, fixed sensors, and remote or mobile sensors.

Surface-following devices: While tide poles are inexpensive to install, they are tedious measurements to make and require the wave averaging to be done by eye. Placing a float gauge (Pugh et al., 2014) in a stilling well introduces systematic wave averaging. They are robust but require installation on a vertical structure and are high maintenance.

Fixed sensors: Acoustic reflection and radar reflection methods are robust and low cost, but again they require vertical structures for installation. **Pressure sensors** have an advantage in that they do not need a vertical structure for installation. However, they require water density and wave corrections and are deemed to be high maintenance (Pugh et al., 2014). GPS reflectometry is cost-effective and works best where there is no drying out at low water. However, Williams et al. (Williams et al., 2020) showed that with the latest GPS devices and in combination with improvements to the global satellite network, improved sea-level measurements could be made within

intertidal zones. In this case, the wave average is effectively done by using around 20 minutes of a satellite pass to derive the sea level height.

Remote/mobile sensors: Satellite altimetry gives global coverage of sea levels, but the coarse resolution makes it difficult to interpret readings in the intertidal zone. Surface GPS buoys were previously expensive to build and deploy. However, Knight et al. (2020) showed that low-cost GPS buoys could deliver accurate sea-level measurements and can be potentially installed in the intertidal zone.

3.2.3 Sensors and Measurements

Pressure sensors are suitable devices for measuring sea levels in an IoT network. However, commercially available devices can be very expensive, with single pressure-based tide gauges costing more than £1000. For example, the Nortek AWAC used for comparison in this research project costs around £17,000 (although it also measures waves and currents). While these types of commercial gauges are capable of long deployments and near-real-time data return, they have a high initial cost for self-contained devices and require additional electronics and software packages for the telemetry element.

Beddows et al. (2018) showed that inexpensive pressure sensors (e.g., MS5803, 2-bar and 5-bar pressure sensors from Measurement Specialties) could be used for long periods and produce reliable data when combined with low-cost microcontrollers. They recorded pressure measurements internally (on microSD cards), recovered the data many months later and demonstrated that the sensors could remain stable over long deployments. Also, Lyman et al. (2020) used these types of sensors together with low-power micro-controllers to record high-frequency pressure data for long periods (e.g., MS5803, 10-bar pressure sensors from Measurement Specialties).

The research presented here demonstrates that low-cost pressure sensors can provide accurate sea-level measurements, and when incorporated with a Sigfox ultra narrowband wide-area network with off-the-shelf Arduino micro-controllers, can be incorporated into an IoT network, which can then provide the necessary data to monitor the changes in coastal morphology.

3.3 IoT Tide Gauge Network Design

There are many tide gauge networks around the world, for example, national networks covering whole coastlines and localized networks often associated with port operations. These use a variety of different communication methods (cellular, ethernet, telephone lines, etc.) to transmit the data to users (Holgate et al., 2008; Pérez et al., 2013). These tide gauges are often sparsely spread along coastlines, and some port authority data are not always publicly available.

The “Internet of Things” (IoT) tide gauge network tested here is being developed specifically to support morphology monitoring. However, it could be easily adapted to fill in gaps and contribute to

larger data projects such as Smart Cities (Kim et al., 2017) or Smart Coastlines (Bresnahan et al., 2020). It uses the IoT ultra narrowband wide area network, which combines low-power communication with good range, an ideal combination for coastal locations away from major infrastructure.

The IoT, tide gauge network, is required to provide accurate sea-level for coastal monitoring at a number of locations (for duplication and redundancy), in both near-real-time mode and "delayed-time" mode. An IoT device on a beach needs to store data in memory when communications are inhibited by being underwater and then begin to send that data when exposed to air during the ebb tide. In addition, each tide gauge in the network should have relatively low-power consumption to be capable of long deployments.

3.3.1 Design of IoT-Enabled Tide Gauge

The monitoring system architecture (see Figure 3.1) comprises a number (depending on the location) of individual tide gauges, all of which communicate with one or more base stations. The base stations then relay the data messages to the "cloud" on a regular basis. Once in the cloud infrastructure, the data can be pushed or picked up by other data servers for postprocessing. For example, the data could consist of 40-s averages of pressure data representing water level, and other statistics of the 10-Hz data, such as burst maximum, minimum and standard deviation, which can be used as a proxy for wave conditions.

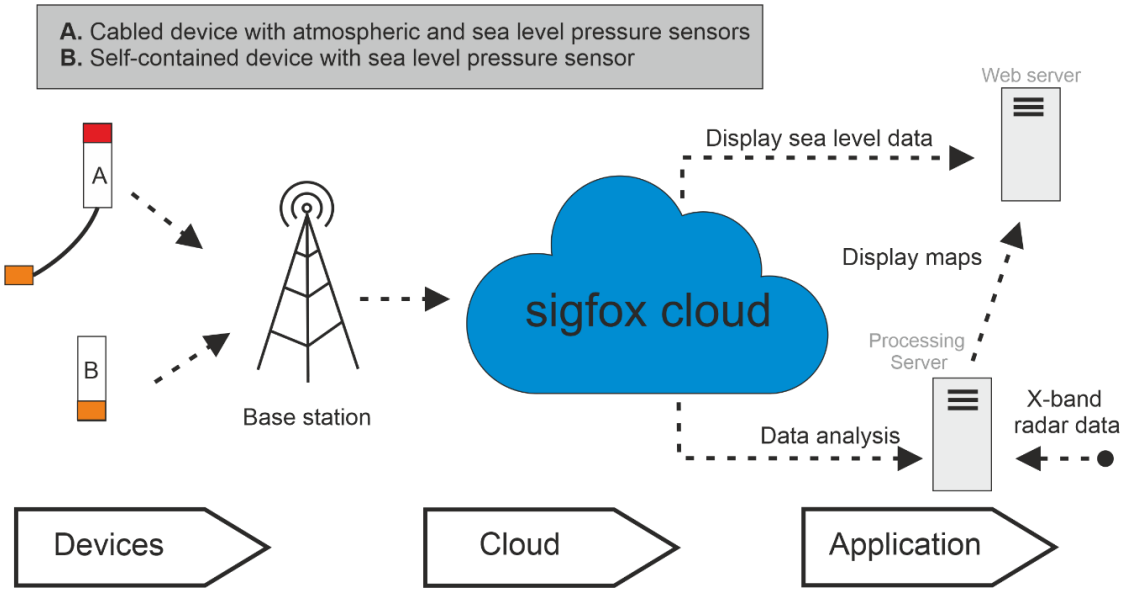

Figure 3.1: Monitoring system architecture.

The IoT-enabled tide gauge developed here is based on the off-the-shelf Arduino MKR micro-controller. The controller is available with a variety of communications formats, including Sigfox (MKR FOX 1200), LoraWan (MKR WAN 1300), and GSM (MKR GSM 1400). For this project, we chose the MKR FOX 1200 as it has an established subscription-based backend communication

infrastructure, and each unit comes with one year's free subscription. The cost of the MKR FOX 1200 controller is around £40.

The GSM version was excluded because it was twice the price of the others and had relatively high running costs. The LoraWan and Sigfox controllers are very similar in characteristics and cost, but to use the MKR WAN 1300 requires access to a LoraWan base station.

3.3.2 Arduino Micro-Controller

The Arduino MKR FOX 1200 (see Figure 3.2a) is based on the SAMD21 microchip and an ATA8520 Sigfox module. It has low-power Sigfox communication, 32-bit computational power and can be programmed using the well-supported Arduino Software (IDE) development package.

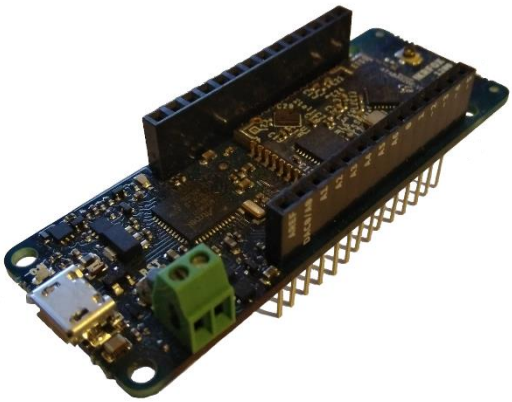

(**a**)

(**b**)

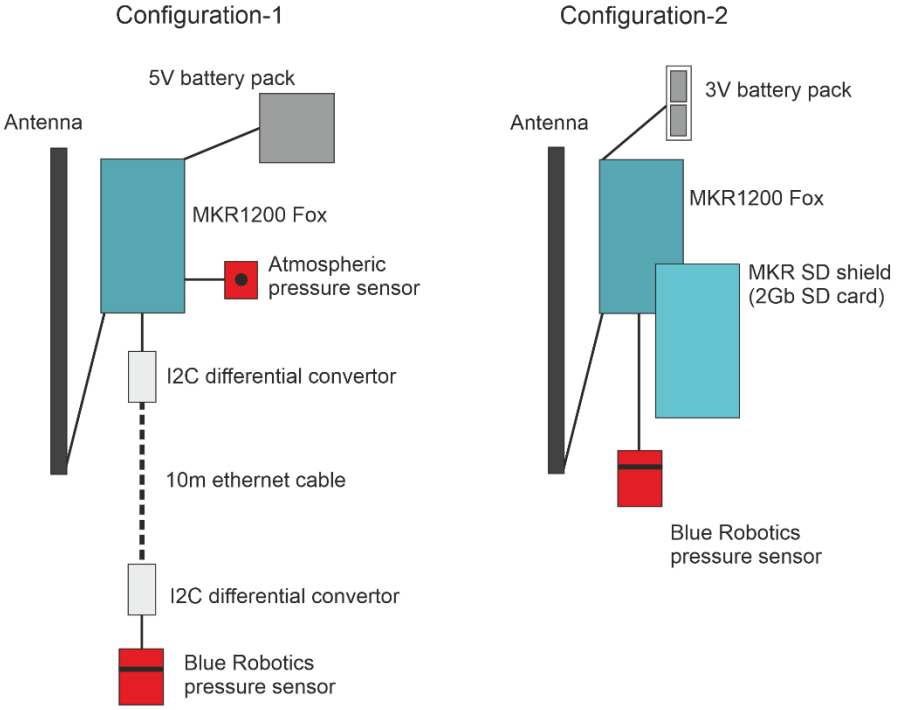

(**c**)

Figure 3.2: (a) Arduino MKR 1200 Fox micro-controller, (**b**) Blue Robotics 2-bar (MS5837 pressure sensor), (**c**) Configuration-1 and Configuration-2.

Power can be supplied via the USB port at 5 V, using a battery pack that does not shut down when the Arduino goes into low-power mode (e.g., the Voltaic Systems USB battery is suitable for this purpose), and at 3.3 V on the I/O pins using a couple of AA, AAA, C or D-cell batteries. The Arduino typically takes around 20 mA, and with the sensors used here and other electronic components, e.g., SD Proto Shield with SD card, gives a total current draw of between 35 and 54 mA, and with a 70 mA current draw during the 1–4 s Sigfox transmission. Bench tests suggest that two alkaline D-cell batteries would last up to 22 days by sampling for 40 s periods and then cycling to sleep mode. Using the Voltaic Systems USB battery with solar panels can allow for continuous recording. The micro-controller is relatively small at 68 mm length and 25 mm width. It is designed to use "prototyping shields" such as the MKR SD Proto Shield, which can be directly plugged in to provide the internal logging option.

3.3.3 Sigfox Wide-Area Network

The Sigfox module used has a carrier frequency of 868 MHz (working region EU) with an antenna power gain of 2 dB. The Sigfox network permits a maximum of 140 messages of 12 bytes to be sent each day. For instance, the data package could be made up of two integers (taking one byte each) and five floating-point numbers (taking two bytes each). This restriction for the UK is due to European Telecommunications Standards Institute regulations, which only permits devices on these frequencies to send messages 1% of the time (36 s in each hour). The typical communication range is around 10 km in urban areas and 40 km in open countryside.

Data from the IoT devices are delivered to the Sigfox Cloud (see the schematic of the overall network in Figure 3.1) and redistributed from there to various servers for processing and display. For example, web servers show the tabulated data and graphical outputs; and a computer-server prepares inputs for the waterline algorithms in combination with the marine X-band radar data to produce beach morphology DEMs.

3.3.4 In-Water Pressure Sensor

A Blue Robotics two-bar pressure and temperature sensor ("Blue Robotics Bar02 Ultra High Resolution 10m Depth/Pressure Sensor," 2020) was used for measuring water depths (see Figure 3.2b). It is based on the Measurement Specialties MS5837 2BA gel-filled, compact, water-resistant sensor ("Measurement Specialties, MS5837-02BA Data Sheet," 2020). This is a low current (0.6 µA) 24-bit digital output I^2C device. The sensor has a quoted 10-bar maximum mechanical pressure, with a standard operating pressure of 0–2 bar, giving an equivalent measuring range of 10 m of seawater (water depth pressure plus atmospheric pressure) with a water depth resolution of 0.16 mm. The Blue Robotics two bar sensor, although relatively expensive at £70 when compared to buying just the

pressure sensor (~£4), was chosen for testing since it was already fully waterproof and ready for installation. The pressure sensor was tested in the lab with a 4-m vertical tube of fresh water and performed within ±1 cm when varying the water levels.

3.3.5 Atmospheric Pressure Sensor

Atmospheric pressure needs to be known when converting the measurements made with the Blue Robotics pressure sensor into the depth of water. The instrument used is a Bosch BME280 environmental sensor, an I^2C sensor with temperature, barometric pressure and humidity. It is a low current sensor, 3.6 μA at 1 Hz for humidity, pressure and temperature, and 0.1 μA while in sleep mode.

3.3.6 Enclosures and Cabling

Various types of enclosures were tested during the field experiments (see Section 3.4): Experiment 1 used an inexpensive PVC wastewater pipe with waterproof sealed end caps; in Experiment 2, a Blue Robotics 7.62-cm (3-inch) enclosure was used with the standard end caps.

In the first experiment, a PVC pipe (with 5.08 cm (2 inches) diameter and 35 cm length) housed the main electronics and antenna, and a smaller PVC pipe (4 cm diameter with 15 cm length) held the in-water depth pressure sensor and some ancillary components (e.g., an I^2C differential converter). The two separate parts were connected using a waterproof ethernet cable that was sealed at both ends using epoxy resin. I^2C sensors are limited to using cable lengths of up to one meter; when using much longer cables, such as the 10-m cable (necessary because of the large tidal range), two I^2C differential converters must be incorporated at each end of the cable run.

In the second experiment, a Blue Robotics 5.08 cm (2 inches) diameter enclosure contained all the electronic components, antenna and batteries.

3.3.7 Converting in-Water Pressure Measurements to Water Depth

Using measurements of the water pressure and atmospheric pressure, a water depth can be calculated using the equation:

$$\text{water depth} = (P - P_{atm})/(\rho\, g) \quad (1)$$

where water depth is in cm, P is the total pressure at the sensor in millibars, P_{atm} is the atmospheric pressure in millibars, ρ is the density of the seawater in kg m^{-3}, and g is the gravitational acceleration 9.81 m s^{-2}.

The main errors in this calculation are associated with determining the seawater density and water temperature.

3.4 Field Experiment Locations and Configurations

Experiments were carried out to ascertain the accuracy of the IoT tide gauges compared with established tide gauges and also to demonstrate the versatility of an IoT tide gauge network with its different and complementary hardware and software configurations.

Two different locations were chosen (see Figure 3.3):

- Experiment 1—a sheltered location beside the dock wall at Liverpool (near to the Sandon Half-tide Dock entrance) on the tidal River Mersey is typical of most tide gauge installations;
- Experiment 2—a beach location at Blundellsands, Crosby, where there is a wide intertidal beach and sea defences to protect residential areas, with more exposure to waves.

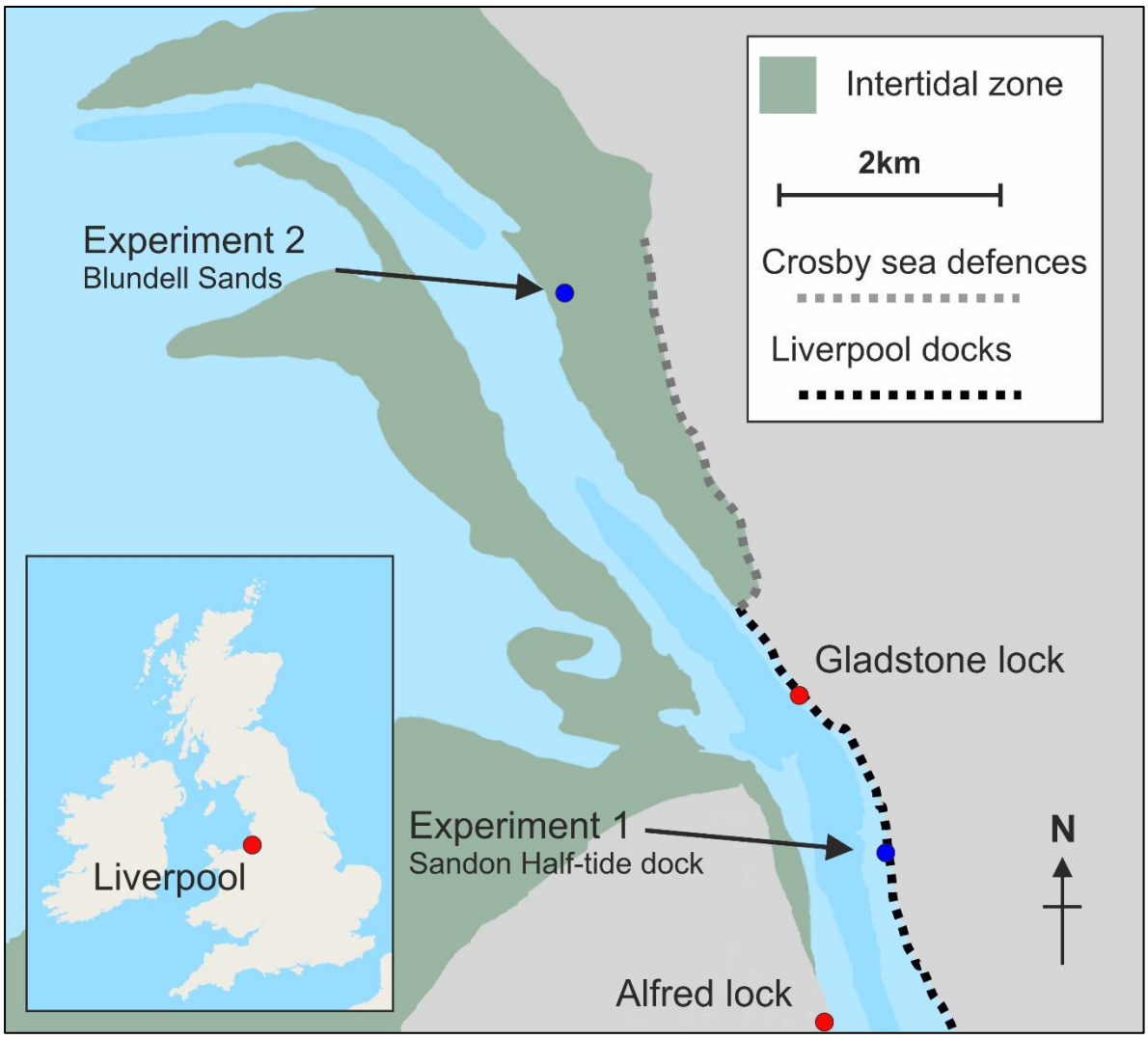

Figure 3.3: Fieldwork and local tide gauge locations in the Mersey Estuary; local tide gauges (red dots), experiments (blue dots).

In this macro-tidal region, the tidal range can exceed 10 m at spring tides; at Liverpool, the largest tidal range is 10.35 m, mean high water spring (MHWS) is 9.39 m above local chart datum (CD)

while mean low water spring (MLWS) is 1.12 m CD ("National Oceanography Centre, National Tidal & Sea Level Facility: Liverpool tide gauge statistics," 2020). The local chart datum is 4.93 m below the land-based ordnance datum Newlyn.

3.4.1 Experiment 1: River Mersey, Liverpool

This site near to the Sandon Half-tide Dock entrance (53°25′37.9″ N, 3°0′22.9″ W, WGS; British National Grid 333,227 392,738) is approximately 2.6 km upstream of the research-quality tide gauge at Gladstone Lock and about 2.6 km downstream of a port authority tide gauge across the river at Alfred Lock (see Figure 3.3). There are steps down to the water at this location (no public access), and the edge of the river bed is exposed at low water spring tides but not exposed at low water neaps.

The IoT tide gauge consisted of a Blue Robotics pressure sensor connected by cable to an enclosure containing the Bosch BME 280 sensor, Arduino micro-controller, I^2C differential converter and antenna. The enclosure was attached to safety railings on the dock wall along with a separate Voltaic Systems V44 battery (12,000 mAh) (see Figure 3.4). This battery supports the low-power sleep mode micro-controllers (i.e., it does not turn off if the current draw becomes small during the Arduino's sleep cycles), and Voltaic Systems solar panels can be added to provide continuous power. A valve was fitted to the top of the enclosure to allow for changes in air pressure. The Blue Robotics pressure sensor was located at the end of an external 10 m long ethernet cable at the bottom of the steps extending down the dock wall, to a couple of meters above the low watermark, in order to capture as much of the tidal range as possible. The installation was levelled to the local vertical datum by measuring the vertical distance from the pressure sensor to the top of the dock wall, the height of which was found using LiDAR data.

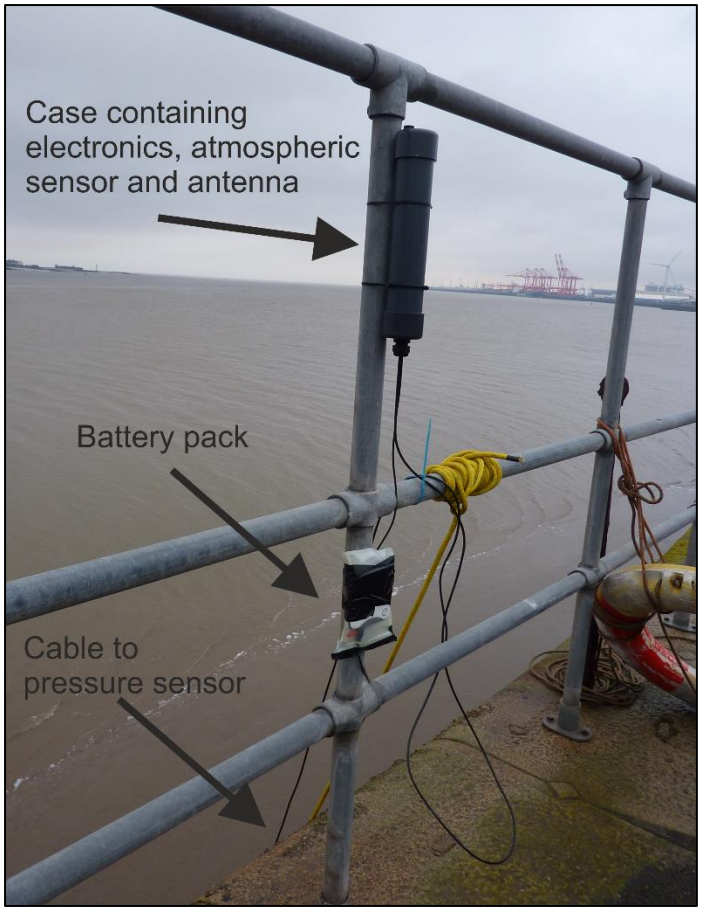

Figure 3.4: Sensor installation at Sandon Half-tide dock, Liverpool.

Configuration 1 (see Figure 3.2c) was used for this experiment: set to wake up every 15 min (to be within the 140 daily message limit for Sigfox and to be comparable with the 15 min sampling of the nearby Gladstone lock tide gauge (see Figure 3.3), record for 40 s (to allow for averaging out of high-frequency wind-generated waves), and then send the averaged pressure and temperature data for each sensor via the Sigfox network. The data package contained the status, BME temperature, BME pressure, BME humidity, Blue Robotics pressure and Blue Robotics temperature. Date/time was added at the Sigfox backend as soon as each message had been received. To save power, no SD card was installed, and hence no data were stored internally during the deployment period.

The IoT tide gauge was deployed for seven days between 1 and 8 November 2019, spanning the transition from spring to neap tides (peak spring tide occurred on 28 October, while lowest neap tide occurred on 6 November).

3.4.2 Experiment 2: Intertidal Zone, Crosby

The site on a wide intertidal beach at Blundellsands, Crosby (53°29′43.6″ N, 03°04′1.5″ W, WGS; British National Grid 329306, 400389), is 500 m from the sea defences and 6 km from Gladstone Lock tide gauge (see Figure 3.5). The IoT tide gauge was attached to a navigation channel marker post, close to a Nortek acoustic wave and current profiler (AWAC).

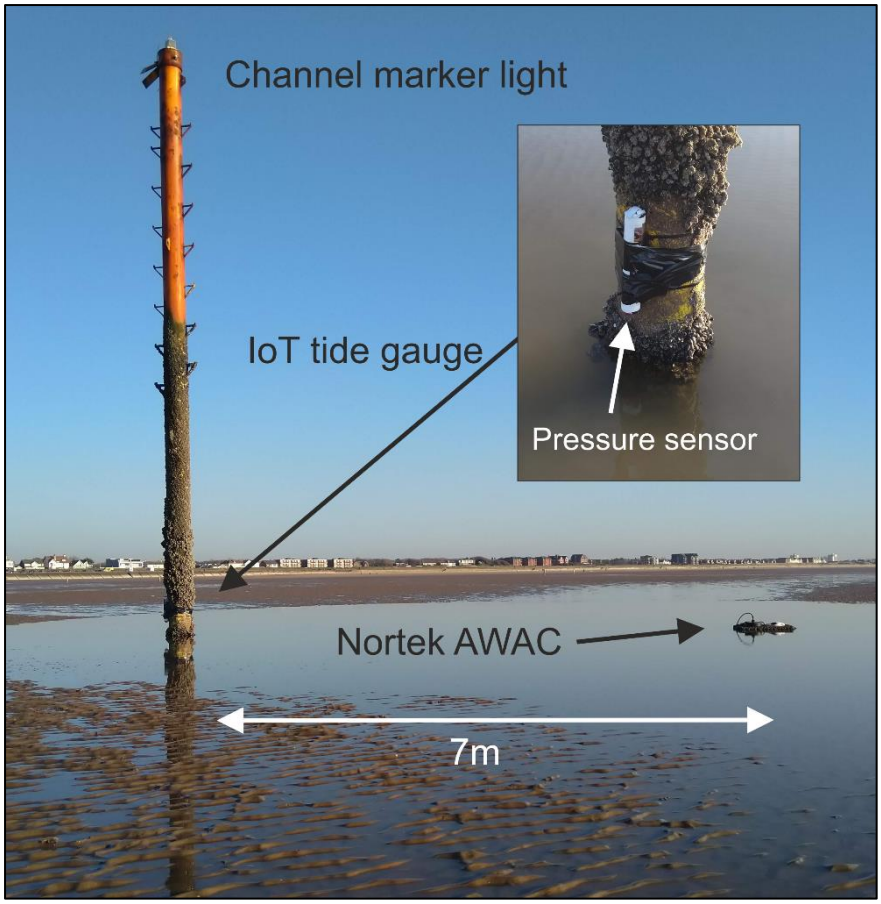

Figure 3.5: Sensor installation at Crosby (Blundellsands). The "Internet of Things" (IoT) tide gauge was attached to the channel marker, and the Nortek acoustic wave and current profiler (AWAC) was located 7 m away and attached with a chain.

The AWAC was part of a local government coastal monitoring study and provided a direct comparison with the measurements from the IoT tide gauge. It was set up to measure currents and sea levels every ten minutes and provide hourly wave measurements based on burst sampling; these data were recovered five months later. The IoT tide gauge was deployed to capture data during Storm Ciara, which arrived in the UK during 8–9 February 2020, to determine the quality of the sea-level data in an exposed intertidal location with expected large waves.

Configuration 2 (see Figure 3.2c) consisted of Blue Robotics waterproof case enclosing an Arduino micro-controller, MKR SD Proto Shield (with 2 Gb SD card) for storing data, a Blue Robotics pressure sensor with the electronics, two D-cell alkaline batteries and antenna. The Arduino's internal clock was used for timing, and it was set up to wake up every 15 min, record 40 s of 10-Hz data, calculate maximum, minimum and average values, store these data internally onto the SD card, store the 40-s averages into RAM memory, and send them back via the Sigfox network when the instrument was exposed at low tide (when underwater there was no data transmission). Each data package contained the month, day, hour, minute, and four Blue Robotics pressure values. This configuration allowed most of the sea-level data to be returned during the "dried out" period.

The IoT tide gauge (at the pressure sensor level) and AWAC were levelled to the local vertical datum using heights from GPS. In this experiment, the local atmospheric pressure was obtained from another device at the shoreline (it is envisaged that for an operational IoT tide network that these data would be provided by a weather station colocated with the X-band radar unit or using a cabled configuration as in Section 3.4.1). The IoT tide gauge was attached to the channel marker (see Figure 3.5) with cable ties and tape during low water on 6 February and then recovered immediately after the storm; last data were recorded at 00:50 on 10 February.

3.5 Field Experiment Results

3.5.1 Comparison of the IoT Tide Gauge and Local Tide Gauges

Figure 3.6a,b compares data from the IoT gauge near Sandon Dock (pressures converted to meters of water) and the local tide gauge records for two periods during the transition from spring to neap tides. Whereas Figure 3.6c shows the raw pressure data prior to conversion to sea-level values for the whole deployment period. The Gladstone Lock tide gauge records 15-min averages, while the Alfred Lock tide gauge records one-minute averages. At the beginning of the experiment, the tidal range close to the spring tide was large, which exposed the pressure sensor at low water; towards the neap tide, it was always underwater.

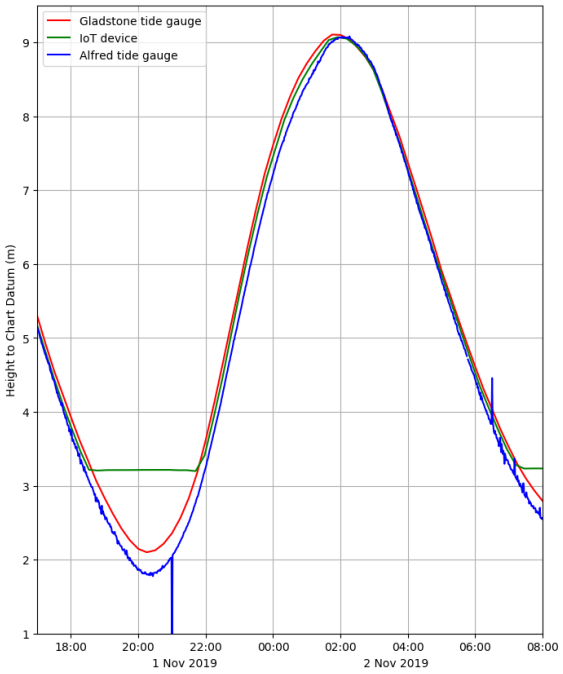

(**a**)

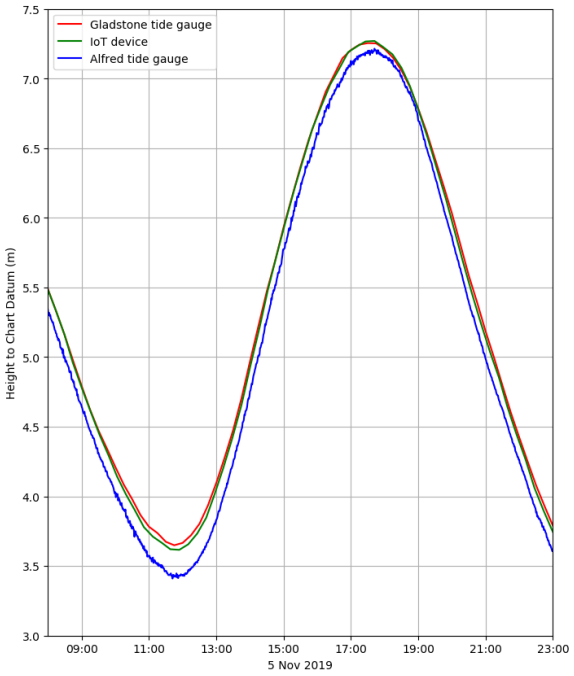

(**b**)

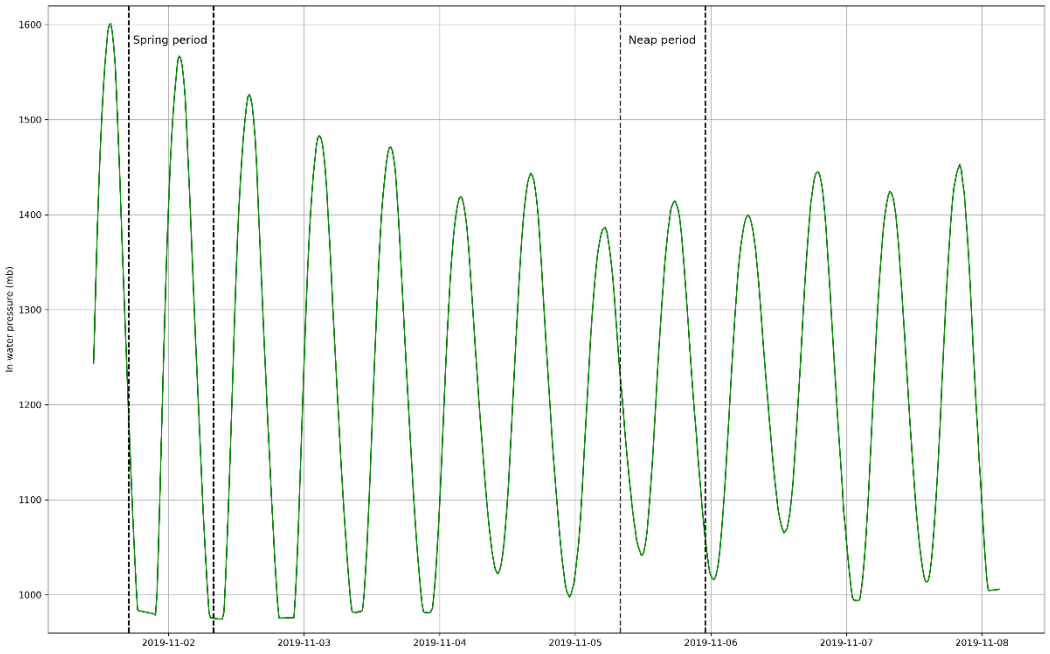

(**c**)

Figure 3.6: Liverpool tidal elevations (Gladstone Lock—red, IoT device—green, Alfred Lock—blue), (**a**) Spring period: 1 November 17:00–2 November 08:00, 2019, (**b**) Neap period: 5 November 08:00–23:00, 2019, (**c**) raw in-water pressures from the Blue Robotics pressure sensor for the whole deployment period.

The time lags (of a few minutes) in the tidal curves for Gladstone Lock and Alfred Lock reflect their relative locations along the estuary (Figure 3.6a,b). As the flood tide propagates up the estuary, it reaches Gladstone Lock first, then Sandon Half-tide Dock and Alfred Lock. This can be seen clearly during the approach of high water on 2 November (02:00), with high water at Alfred Lock occurring last. The differences in tidal height and time lag between Sandon Half-tide Dock and Gladstone Lock are smaller than in the corresponding Alfred Lock data, and this is likely because of their locations on the same side of the river/estuary; Figure 3.3 shows the narrow channel (~940 m at its narrowest part) which connects to an inner much wider part of the estuary (not shown on map), and the corresponding tidal flows are controlled by the cross-section and bed friction (Pugh et al., 2014).

The cabled pressure sensor configuration worked well, giving comparable sea-level data to the established tide gauges and having sent the data successfully via the Sigfox Cloud to the data processing server. The mean difference between the IoT device and the Gladstone lock data was 0.002 m, the standard deviation was 0.035 m, and the root-mean-square difference was 0.035 m (using all the recorded data and ignoring periods when the in-water pressure sensor is exposed to air, i.e., towards low water during Spring tides); the majority of these differences are likely to be due to the 2.6 km separation between locations. The battery pack also worked well; when coupled with solar panels, it would provide continuous power for the IoT tide gauge, necessary for long-term deployments.

3.5.2. Comparison of the IoT Device and AWAC—Sea Levels

Figure 3.7 compares sea-level data (with waves minimized by averaging) at Crosby from the IoT device and the AWAC for neap tides between 6 February 18:00 and 7 February 15:00, 2020, and during Storm Ciara on 9 February 05:00–23:59, 2020. The two instruments generally agree during the earlier period (see Figure 3.7a), but there are obvious differences close to high water during the storm when large waves were present (See Figure 3.7b). Differences in the last tidal level recorded before drying out and the first tidal level recorded on the flood are an artifact of the rolling 15-min sleep time (sleeps for 15 min, does 40 s measurement and goes to sleep again) and the exact 10-min AWAC data, and combined with the 27-cm vertical separation of the pressure sensors.

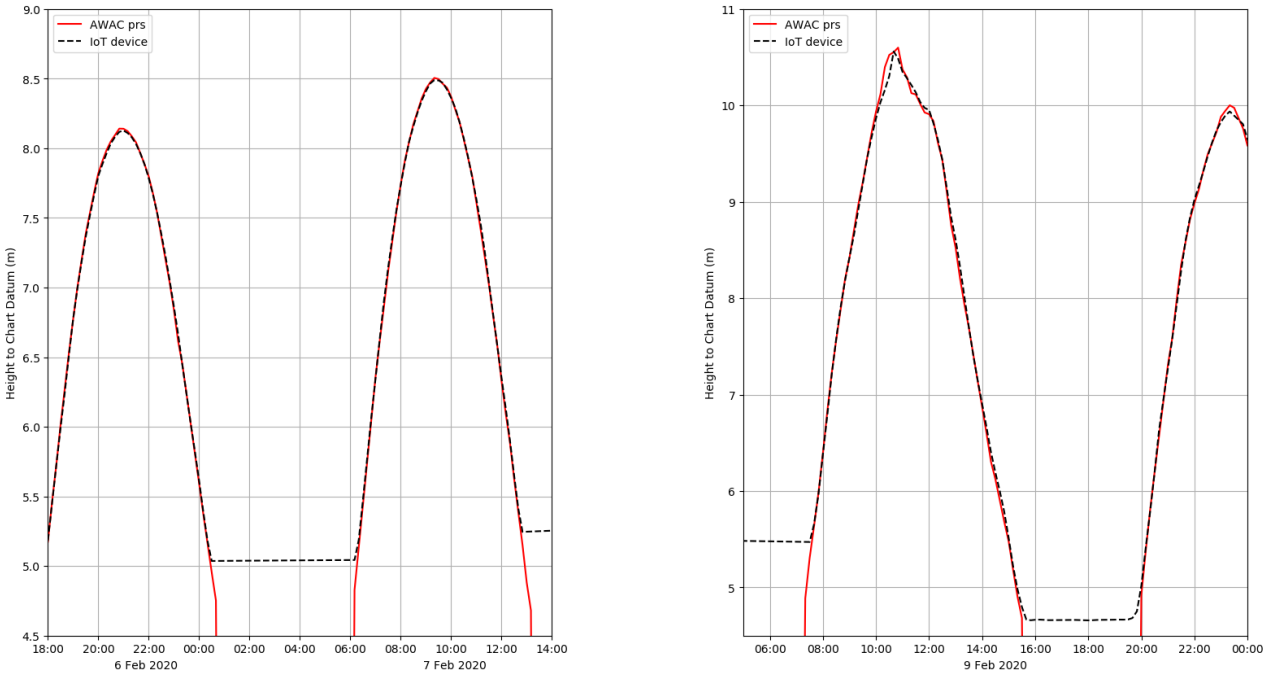

(**a**) (**b**)

Figure 3.7: Crosby tidal elevations (AWAC—red line, IoT tide gauge—black dashed line), (a) neap tides: 6 February 18:00–7 February 15:00, 2020, (b) Storm Ciara: 9 February 05:00–23:59, 2020.

The Van de Casteele Test (Miguez et al., 2008) can be applied to determine tide gauge performance. For example, Miguez et al. (Míguez et al., 2012) tested a variety of tide gauges and demonstrated the test's ability to highlight different types of tide gauge error, while André et al. (2013) used it to compare data from three different GNSS buoys for measuring sea level against a nearby radar tide gauge.

The method compares a reference tide gauge data set (data known to be an accurate measurement of sea level; in this case, the AWAC sea-level data are taken as the reference) to contemporaneous data from the tide gauge being tested (H'): the reference sea-level data (H) are plotted on the ordinate against the tide gauge difference (ΔH) on the abscissa (x-axis), where $\Delta H = H - H'$. The resulting

diagram would produce a straight vertical line centered on $x = 0$ for a perfect match between the two tide gauges.

Applying the Van de Casteele Test to the IoT tide gauge, using the AWAC data as the reference, the near-vertical alignment of the differences in the two data sets (see Figure 3.8a) between low water and high water, although not perfectly vertical, indicates that there are no timing offsets (which would result in an ellipsoidal pattern) and no obvious systematic errors (such as scale errors, which would introduce a large gradient from low water to high water). The mean difference between the IoT device and the AWAC data was −0.005 m, the standard deviation was 0.040 m, and the root-mean-square difference was 0.040 m (using all the recorded data and ignoring periods when the pressure sensor is exposed to air, i.e., towards low water).

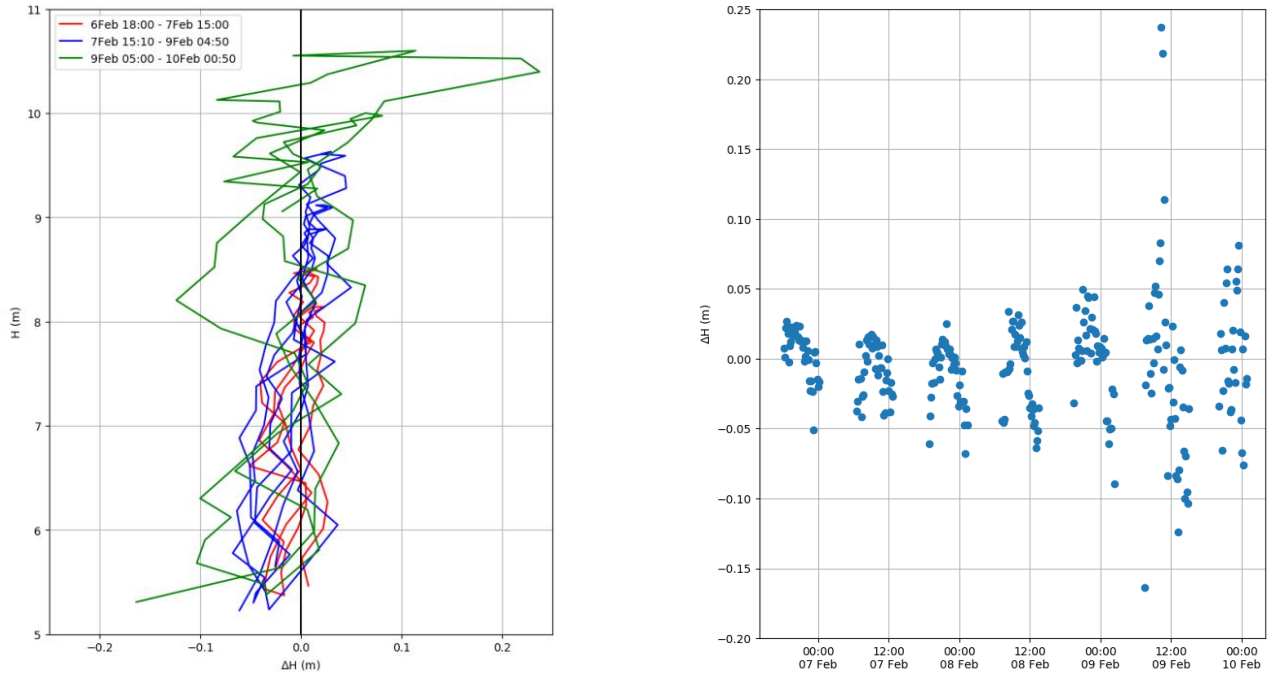

(**a**) (**b**)

Figure 3.8: Results of the Van de Casteele test: (**a**) for the IoT tide gauge using the AWAC tide gauge as a reference. (**b**) Time-series of tide gauge differences.

Although there is a slight gradient from low water to high water with larger offsets towards low water, it is unlikely to be due to density differences since both gauges use the same seawater density of 1025 kg m^{-3} for the conversion to meters of water. However, this small gradient may be a result of turbulence around the channel marker during the lower levels of flood and ebb. Another possible explanation could be air bubbles trapped on the pressure sensor membrane during drying out (this could occur with either pressure sensor); higher pressures towards high water may compress the bubble resulting in smaller pressure differences between them. One way to eliminate this would be to deploy the IoT device horizontally so that the pressure sensor is not facing downwards.

During Storm Ciara, large waves were present, and this can be seen in Figure 3.7b, Figure 3.8a,b and Figure 3.9. The pressure differences (seen within the corresponding sea-levels) become larger with increasing wave heights, and the largest offsets occur between 09:30 and 14:30 on 9 February. These could be caused by the different sampling rates; the IoT device measures for 40 s, and the average is taken for the sea-level measurement, while the AWAC ADCP takes the average over 10 min.

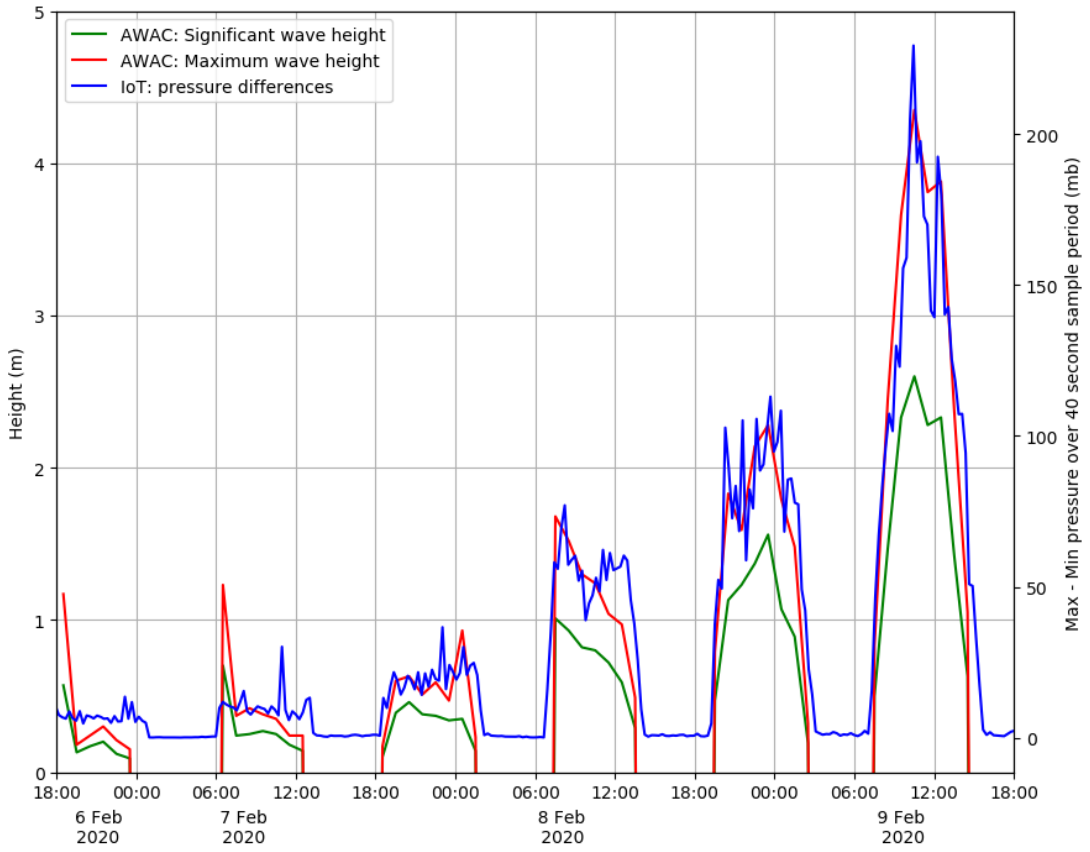

Figure 3.9: Time-series comparisons (**a**) left y-axis: significant and maximum wave heights from the AWAC ADCP (**b**) right y-axis: differences between maximum and minimum pressures recorded during the 40-s burst.

3.5.3 Comparison of the IoT Device and AWAC—Waves

In Experiment 2, the IoT tide gauge was set up to return sea-level data. However, the recovered data (i.e., 1-Hz data and 40-s period statistics) also demonstrated the capability to capture higher frequency water level variability due to waves. This is explored in this section to illustrate the wider application of the IoT sensor network for monitoring waves.

At this stage, no attempt is made to calculate the pressure attenuation factor, which is necessary to determine actual wave heights in meters of water (this type of processing would be beyond the Arduino micro-controller). However, postprocessing of the internally logged 10-Hz data using open source “R” and Matlab algorithms developed by Miller and Neumeier (Miller et al., 2019; Neumeier, 2020) (based on methods outlined by Tucker and Pitt (Tucker et al., 2001)) could be applied to

generate the wave height and wave period statistics. For example, Lyman et al. (2020) used similar pressure sensors deployed in water depths of 9 m and 18 m and were able to successfully calculate the wave statistics. The AWAC uses a different set of post-recovery algorithms ("Nortek manuals," 2020) utilizing both the pressure and current to derive the wave statistics.

Figure 3.9 shows the hourly wave statistics from the AWAC, measured during the 1000-s measurement time together with the corresponding differences between maximum and minimum pressure recorded during the 40-s bursts. Although the units of the *y*-axis scales are different, these IoT pressure statistics do align themselves closely with the maximum wave heights from the AWAC.

It is likely that the IoT pressure sensor is not resolving some of the larger waves since it is only recording for 40 s every 15 min, whereas the AWAC, setup in burst mode to record over 1000 s every hour, can measure the larger waves. While this Configuration 2 did not send these pressure differences via the SigFox network, the software could be modified easily to return them instead. In practice, one IoT tide gauge could send the sea-level data and another the 40-s period burst pressure statistics.

3.6 Discussion and Conclusions

Experiments 1 and 2 demonstrate the versatility of the Arduino-based devices, with each tide gauge being combined with built-in Sigfox IoT communications and low-cost pressure sensors. While the pressure sensors are capable of measuring sea levels accurately, exposure to waves can contaminate the measurement as the averaged data still appears to contain a contribution from waves, especially during stormy periods. The usual practice is to deploy tide gauges well away from wave exposure. A root-mean-square difference of 0.04 m between the IoT pressure sensor and the AWAC data is an acceptable result, considering the data spanned Storm Ciara. However, deploying the IoT gauge in a more exposed location demonstrates the potential for simultaneously providing valuable information on waves. In addition, the data were successfully transmitted over the Sigfox network and prove that a network of such devices would be feasible. For the proposed tide gauge network, a series of IoT tide gauges based on the Arduino with Sigfox and the pressure sensors would be installed, with a variety of software and hardware configurations.

Experiment 1 using the cabled system was the simplest approach and would be best suited to locations where the antenna (plus electronics) could be in “air” for the deployment period. This type of installation would require a structure such as a pier, breakwater, with either a pole already present or where one could easily be fitted. The navigation pole at the beach location could have been used with this configuration. This hardware with this configuration could be deployed for long periods when combined with solar panels for the battery pack.

The self-contained system used with Experiment 2 demonstrated how the IoT tide gauge would perform if located on a beach with no options for a cabled installation, e.g., attached to the beach with a screw anchor. The inexpensive Blue Robotics enclosure was waterproof and able to withstand the conditions of Storm Ciara; the case was completely watertight even with storm waves impacting it. In this configuration, the IoT device would send back data once the antenna is not underwater and able to transmit. This would allow deployments further offshore nearer to the low water mark and for instrumentation across a wider area of the intertidal zone.

The Van de Casteele test on data from Experiment 2 revealed a small-scale "error" (see small pressure difference gradient in Figure 3.8a) that may be the result of factors mentioned in Section 3.5 (bubbles on the pressure sensor membrane may be the main cause of errors). This could be easily verified by testing and deploying the IoT device with the pressure sensor in the horizontal position. The larger pressure differences between the IoT pressure sensor and the AWAC are most likely to have been caused by waves not being filtered out sufficiently by the data-averaging. In addition, the different sampling periods and times of sampling would result in the IoT missing some of the larger waves during its 15-min sleep period. In future experiments, this could be rectified by increasing the 40 s sampling period.

After the success of using off-the-shelf parts for the IoT tide gauge, it would be worthwhile experimenting with lower-powered micro-controllers such as the ATMega 328P driving the same pressure sensors. Lyman et al. (2020) have shown that the ATMega 328P is capable of three months of continuous internal logging (to microSD card) of pressures (using MS5803) with three AA batteries and more than a year with D-cell batteries. This would reduce the cost of future devices even more, especially if individual pressure sensors are used (and waterproofed) instead of using the off-the-shelf waterproofed Blue Robotics sensor. In addition, the continuous recording of data would allow for adaptive control to be incorporated into the software, e.g., to send more messages during extreme events.

The two contrasting configurations demonstrate that low-cost IoT tide gauges can provide good quality sea-level data in both real time and "delayed mode" using the Sigfox infrastructure. They can also provide the necessary sea-level data to supplement and enhance coastal monitoring strategies and to support safe port navigation. In addition, the latter configuration also shows the potential to deliver wave information, high-frequency data (after recovery) for post-recovery analysis and the option to transmit proxy wave data in near-real time. Furthermore, the IoT tide gauge network described here could also be used for port operations and to provide ground-truthing for hydrodynamic models of complex locations such as tidal inlets and estuaries.

3.7 Funding

The research is part of a PhD study funded by the “Low Carbon Eco-Innovatory (LCEI)—Liverpool University” (www.liverpool.ac.uk/environmental-sciences/working-with-business), with industrial partner MM Sensors Ltd.

3.8 Acknowledgments

The authors would like to thank Andrew Martin at Sefton Metropolitan Borough Council for data from the AWAC, Russell Bird at Peel Holdings (Mersey Dock and Harbour Company) for tidal data and access to the docks, and Colin Bell at the National Oceanography Centre for access to the POLTIPS-3 coastal tidal prediction software. The research is part of a PhD study funded by the “Low Carbon Eco-Innovatory (LCEI)—Liverpool University” (www.liverpool.ac.uk/environmental-sciences/working-with-business), with industrial partner MM Sensors Ltd. This paper contributes to Work Package 4 of the UK NERC-funded BLUEcoast project (NE/N015614/1).

4 Beach deployment of a low-cost GNSS buoy for determining sea-level and wave characteristics

This chapter was taken from the published research paper:

Knight, P. J., Bird, C. O., Sinclair, A., Higham, J., & Plater, A. J. (2021). Beach Deployment of a Low-Cost GNSS Buoy for Determining Sea-Level and Wave Characteristics. Geosciences, 11(12), 494. (see declaration section page 2 for contribution).

4.1 Abstract

Spatially explicit data on tidal and waves are required as part of coastal monitoring applications (e.g., radar monitoring of coastal change) for the design of interventions to mitigate the impacts of climate change. A deployment over two tidal cycles of a low-cost Global Navigation Satellite System (GNSS) buoy at Rossall (near Fleetwood), UK demonstrated the potential to record good quality sea level and wave data within the intertidal zone.

During each slack water and the following ebb tide, the sea level data were of good quality and comparable with data from nearby tide gauges on the national tide gauge network. Also, the GNSS receiver was able to capture wave information and these compared well with data from a commercial wave buoy situated 9.5 km offshore. Discontinuities were observed in the elevation data during flood tide, coincident with high accelerations and losing satellite signal lock. These were probably due to strong tidal currents, which, combined with spilling waves, would put the mooring line under tension and allow white water to spill over the antenna resulting in the periodic loss of GNSS signals, hence degrading the vertical solutions.

Keywords: sea-level, waves, intertidal zone

4.2 Introduction

Measuring coastal sea levels and waves is an important part of any observation programme, such as radar monitoring of coastal change (Bird et al., 2017), in order to assess the risks of projected climate change, storms and sea level rise to increasing populations, infrastructure, economies and ecosystems (Nicholls et al., 2007). Engineers routinely survey the coastal zone in front of sea defences to evaluate impacts of long-term erosion/deposition, as well as episodic erosion/deposition that can occur during large storms. They can review morphology changes and take action to decrease the flood risk (Spodar et al., 2018); beach replenishment, for example, can reduce the impact of storms on the main sea defences. Understanding sediment movement combined with frequent monitoring allows the scheduled redistribution of sand on popular recreational beaches which have tendencies to erode (Habel et al., 2016). Furthermore, the design of coastal defences (whether soft or hard) requires local

and timely data, often absent due to the limited distribution of instruments in established monitoring networks, and difficulty in measuring within dynamic intertidal zones.

This paper assesses the performance of an inexpensive GNSS buoy to derive both sea-level and wave data from a deployment within the intertidal zone. The resulting positional data to a local vertical datum were derived using RTKLIB software (RTKLIB, 2018), particularly the post-processed kinematic (PPK) method with a fixed geodetic GNSS base station on the shoreline. The advantage of this technique is that as well as producing results to a local datum, it also uses the derived dynamics from the Doppler shift to increase the accuracy of the positional solutions. Using the set-up with enabled Wi-Fi also allows transferring data in a timely manner without having to recover the GNSS buoy.

4.2.1 Measuring sea level

Methods for measuring sea level can be categorised into three types (Pugh et al., 2014): surface-following devices, fixed sensors, and remote or mobile sensors. Some established methods are not really suitable for the intertidal zone: surface following devices such as tide poles and float gauges in still wells, although robust, require attachment to significant vertical structures to function. Fixed sensors such as acoustic reflection and radar reflection, while low cost also require substantial vertical infrastructure. Another fixed sensor method, GPS reflectometry (Williams et al., 2020), uses the ratio of 'signal' (directly received satellite signal) to 'noise' (caused by satellite signals reflecting off the sea surface);this works best where water is present at all states of the tide, and is not as effective in wide intertidal zones (limiting the number of satellites used at low water). A more appropriate method for intertidal beaches is to use a pressure sensor mounted on the sea bed or attached to a structure (Knight et al., 2020). As well as sea-level data, pressure sensors can also record high frequency data for analysis of waves.

A remote/mobile sensor such as the GNSS buoy has been shown to work well in sheltered, shallow water locations and a number of different GNSS buoys with high-end expensive GPS receivers were tested (André et al., 2013). We have previously used a GNSS buoy equipped with a low-cost receiver that was capable of measuring accurate sea- level data and wave data within a semi-enclosed harbour (Knight et al., 2020). However, analysis of sea-level from a GNSS buoy deployment in the North Sea (Stal et al., 2016) concluded that in the presence of large waves the received GNSS signal contained significant noise.

4.2.2 Measuring waves

As with sea-level measurements, waves can be measured by fixed sensors, remote sensors and surface-following devices. Acoustic Doppler Current Profilers with pressure sensors can be deployed either on the sea bed, and/or within the intertidal zone to measure waves by combining information on water velocity and pressure data to derive wave information, but they are expensive (~USD20,000–

30,000). Radar reflection (Fiorentino et al., 2019) and terrestrial LiDAR (Martins et al., 2017) can also be used to derive wave data, although they need to be mounted on suitable vertical structures at the shoreline or to existing infrastructure, e.g. piers.

There are two main types of wave buoy: systems using inertia-based sensors, and those using GNSS receivers. Since the early 1960s, wave buoys have been built using multiple inertia-based sensors. These are robust, reliable, and therefore commonly used in national wave buoy networks. Examples include the Datawell Directional Waverider Mk III ("Datawell, Directional Waverider MkIII, brochure," 2021) and the TRIAXYS Direction Wave Buoy (MacIsaac et al., 2013); both incorporate accelerometers, gyros, and flux gate compass sensors to derive wave data. These are expensive, require calibration (Andrews et al., 2019), and in the larger sizes are difficult to deploy with small boats.

Over the past twenty years GNSS receivers have been installed on buoys and developed especially for measuring waves using data from a single GNSS receiver. Examples include the Datawell Mini Direction Waverider GPS ("Datawell, Mini Directional Waverider GPS," 2021) and the Sofar Spotter Wave Buoy ("Spotter: the agile metocean buoy," 2021), which can be easily deployed from a small boat. Wave statistics from single receiver set-ups can be calculated using three velocity components derived from the Doppler shift of satellite signal frequency. The advantages of using GNSS buoys as wave buoys are that the resulting wave data already have a reference frame, are lower in cost than inertial-based wave buoys and are smaller, (e.g., the Sofar Spotter is USD5000 list price in July 2021, weighs 5.4kg and has size of 0.42m × 0.31m). However, the main disadvantage is that GNSS receivers can suffer from satellite drop outs during extreme conditions like spilling or breaking waves covering the antenna.

Wave buoys are not routinely deployed within the inertial zone; coastal deployments are often in deeper offshore water. However, a low-cost wave buoy using an electronic inertial measurement unit (IMU) sensor, deployed in the surf zone, was capable of detecting breaking waves (Brown et al., 2021). A small buoy was deployed for short periods at different water depths within the surf zone from 1.0 m to 9.0 m; the mooring was secured to the sea-bed with a drag anchor.

4.3 Materials and method

4.3.1 GNSS buoy set-up and mooring design

Our GNSS buoy configuration was the same as that used at Holyhead harbour (Knight et al., 2020), with the GNSS antenna, receiver and battery attached to the top of the platform and secured between the yellow trawl floats (Figure 4.1a). The overall cost was around USD400 (buoy parts GBP140, GPS/logger USD260). The GNSS system consisted of a U-blox M8T (U-blox, 2019b) single frequency receiver (embedded on the Emlid Reach ("Emlid Reach M+ RTK GNSS module for precise

navigation and UAV mapping," 2019)) using a Tallysman patch antenna, with a 10-cm square aluminium ground plane. The ground plane is essential to reduce multi-path reflections and increase the antenna gain (U-blox, 2019a); its optimum dimensions (often supplied with antenna manufacturer's specifications) are determined by the antenna size. An EasyAcc 20,000 mAh battery pack was used with the Emlid Reach, which provided enough power to cover the period of the experiment; the expected endurance based on the power requirements is up to 4 days. The Emlid Reach was also Wi-Fi-enabled, and this is the method used for downloading data to a laptop after the deployment (typically ~100Mb of zipped raw U-blox format data per day). In trials with an Alpha network antenna (AC1200 USB Wireless Adapter) connected to a laptop, a distance of up to 500m was achieved for successful downloads with the mooring still floating in the water (without needing to recover, and open the electronics enclosure).

GPS and GLONASS raw satellite data were recorded at 5Hz, including the carrier phase information in the U-blox binary format (ubx). To reduce the chance of water ingress into the electronics box, cable ties were applied around the lid to provide additional support to the clamped lid-closure catch.

To allow for more free movement of the buoy, the mooring used two additional surface floats (Figure 4.1a), with the GNSS buoy attached directly to a small Gael Force trawl float and then to a larger yellow polyform A3 buoy. This mooring set-up allows the GNSS buoy to float on the horizonal water level and reduces any angled inclination towards the anchor point. Figure 4.1a shows the top part of the mooring with the GNSS buoy, trawl float and polyform buoy (~5m of rope between the GNSS buoy and the polyform buoy). Small 200g weights were attached to the middle sections of each rope segment to keep the connections under water and to reduce the chance of tangling with the GNSS buoy float arms. Figure 4.1b shows the 15m of rope connected to the ground anchor (1m in length) which was screwed into the sand (the swivel helps to prevent the main mooring line from twisting). Figure 4.1c shows the two different parts of the mooring connected together on the beach at low water.

Figure 4.1: (a) Top part of mooring together with the GNSS buoy, **(b)** ground anchor with swivel, **(c)** complete mooring installed and laid out on the beach at low water.

4.3.2 Buoy testing at Rossall

Rossall, near Fleetwood in NW England, (Figure 4.2) was chosen for the beach deployment. This location is macro-tidal and has dissipative beach characteristics (Scott et al., 2011; Wright et al., 1984) since it consists of fine sand, has a gentle profile gradient (e.g., 1:50) and has a medium intertidal zone (~300m). It is likely that spilling waves would be present, which typically dissipate their energy gradually over a wide surf zone. The location of the GNSS buoy was adjacent to an existing coastal monitoring system (consisting of a deployed X-band radar), and would provide a realistic 'typical' setting for an assessment of its capability.

The buoy was attached to the ground anchor (Figure 4.1b) and laid flat on the beach (deployed position: WGS: 53° 54′ 48.6″N, 03° 03′ 14.3″W). It was approximately 250m from the foot of the concrete sea defences, and between two rock armour groynes that are perpendicular to the sea defences and around 100m in length. The returned sea level and wave data indicate that a semi-permanent deployment of this GNSS buoy would provide the necessary data for analysis of X-band radar data, which would in turn improve the accuracy of the derived spatial and temporal beach morphology (Bird et al., 2017).

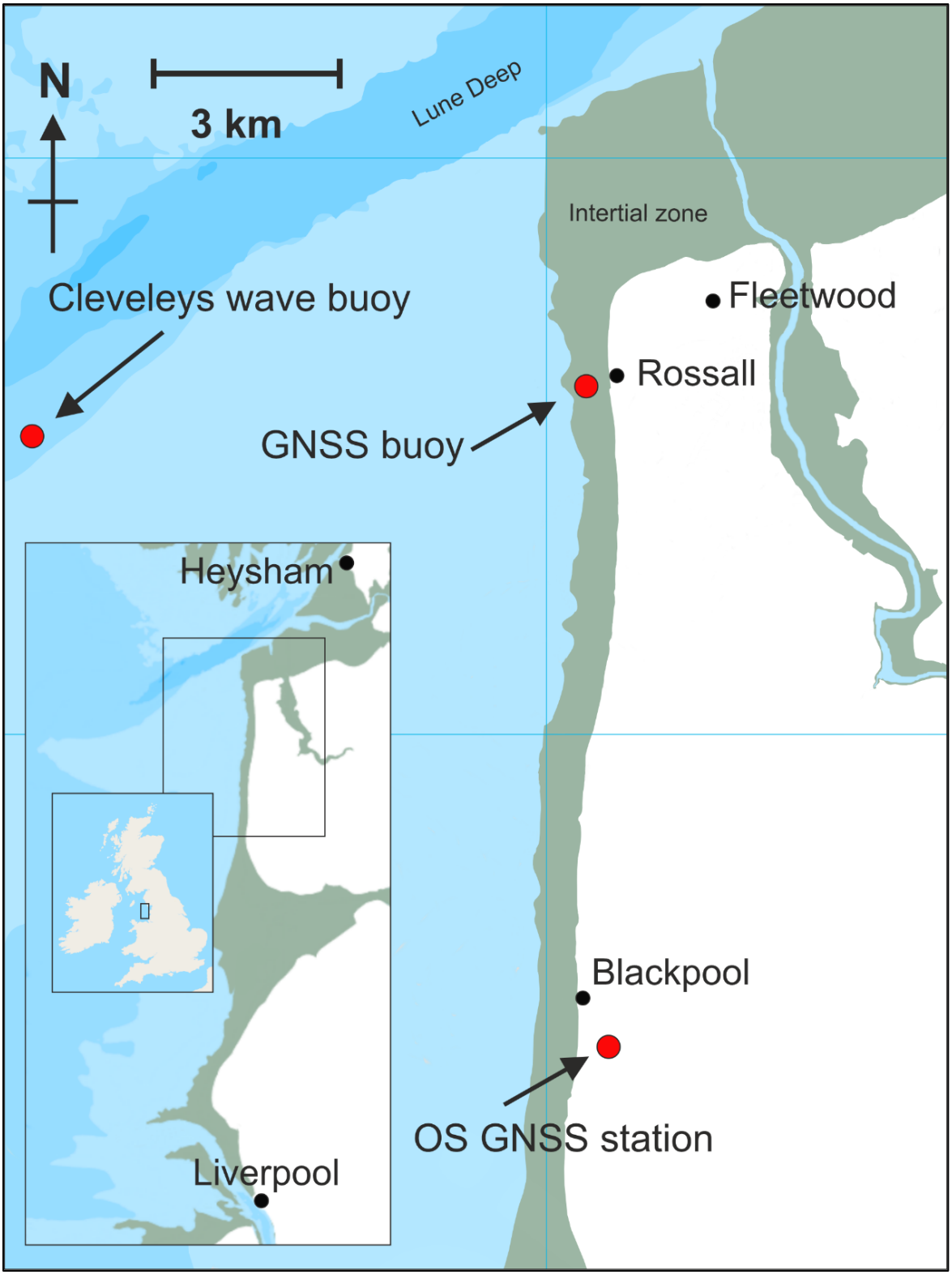

Figure 4.2: Location of Rossall experiment (Lancashire, UK); GNSS buoy, Ordnance Survey GNSS station, Cleveleys wave buoy. Base map source: EDINA Marine Digimap Service (http://edina.ac.uk/digimap).

4.3.3 Local tide and storm surge data

Tidal data for comparison with the GNSS buoy results were obtained from the UK Environment Agency (EA) tide gauges at Liverpool (WGS: 53° 26′ 58.9″N, 03° 01′ 5.2″W, British National Grid: SJ 3248 9525) 50 km to the south, and Heysham (WGS: 54° 01′ 54.5″N, 02° 55′ 13.4″W, British National Grid: SD 3982 5993) 15 km to the north-east, downloaded from British Oceanographic Data Centre (BODC) website www.bodc.ac.uk. The EA tidal data were recorded as 15-minute averages; the EA gauges are part of the UK National Tide Gauge Network ("UK National Tide Gauge Network," 2019). Both of these tide gauges are full-tide bubbler tide gauge systems (Woodworth et al., 2003). The datum used throughout is local chart datum (CD), which at Rossall is 4.90 m below Ordnance Datum Newlyn (ODN).

Tidal predictions of high water (HW) and low water (LW) (National Oceanography Centre 2019) are shown in Table 4.1. At Blackpool, high water was predicted to be 8.87m at 21:23 on 28 August 2019 and 9.01m at 10:42 on 29 August. The highest predicted tide of the spring cycle was 10.27 m on 2 September at 12:64, hence the tides during the experiment were close to the peak springs. Tide gauge data at Liverpool and Heysham show that leading up to these high waters, the storm surge heights were relatively small; ~0.1 m for the first tidal cycle and ~0.3 m for the second tidal cycle ("Archived model surge outputs," 2021).

Table 4.1: Tidal predictions for Liverpool (Gladstone Lock), Blackpool and Heysham (from POLTIPS 2009) for 28–29 August 2019.

	Liverpool		**Blackpool**		**Heysham**	
	Time	**Ht (m)**	**Time**	**Ht (m)**	**Time**	**Ht (m)**
Wed 28 August	15:52	2.00 LW	15:38	2.17 LW	15:51	1.97 LW
	21:32	**8.92 HW**	**21:23**	**8.87 HW**	**21:42**	**9.10 LW**
Thu 29 August	04:30	1.49 LW	04:14	1.60 LW	04:29	1.49 LW
	10:00	**9.12 HW**	**09:55**	**9.01 HW**	**10:11**	**9.33 HW**
	16:48	1.49 LW	16:32	1.61 LW	16:45	1.49 LW

4.3.4 Offshore Wave data

Wave data, for comparison with the GNSS buoy data, were obtained (via the Channel Observatory, 2019), from the Cleveleys wave buoy (WGS: 53° 53.70’N 03° 11.78’W) owned by Sefton Council and situated 9.5 km to the west (Figure 4.2) of the GNSS deployment site at Rossall. The wave data were recorded as thirty-minute values by the Datawell Directional Waverider Mk III buoy deployed in

approximately 10 m of water depth. For reference, and to contrast with the wave heights encountered during the experiment in August 2019, the mean significant wave height (Hs) was 1.0m, standard deviation was 0.60m, with minimum value of 0.09m and maximum value of 2.67m.

4.3.5 GNSS base station and satellite ephemerides data

There is a UK Ordnance Survey (OS) geodetic GNSS site located at Blackpool airport (WGS: 53° 46′ 36.9″N, 03° 02′ 05.9″W, British National Grid: SD 31891 31673), 14.5 km to the south of the deployment site; a source of research-quality GNSS data which can be applied to the post-processed kinematic (PPK) solution. Initial processing used base station data at 30-second intervals from the Ordnance Survey. Once the 1 Hz-data became available (after a delay of 45 days) these were used in the final positioning solution instead. The archived 1-Hz GNSS data were obtained from the British Isles continuous GNSS facility (BIGF) ("NERC, British Isles continuous GNSS facility (BIGF)," 2021).

To improve the overall solution, satellite ephemerides for precise orbit corrections and satellite and station clock error corrections were applied. These were obtained from the Crustal Dynamics Data Information System ("CDDIS, NASA's Archive of Space Geodesy Data. ," 2021; Noll, 2010). The corrections are delivered with increasing accuracy in the form of 'ultra', 'rapid' and 'final' correction files; available between 3–9 hours, 17–41 hours and 11–17 days, respectively. The results in this paper use the final products.

4.4 Results and interpretation

The raw data were downloaded via Wi-Fi using the set-up mentioned in section 4.3.1; this was tested at around 250m range to demonstrate that data could be downloaded with the buoy in the water. If deployed further out towards the low water mark it could be free-floating at times during the spring-neap tidal cycle (e.g., during neap tidal cycles). Data were recorded from 14:10 on 28 August until 15:25 on 29 August over two tidal cycles. The data were subdivided according to when the buoy was free-floating during the tidal cycle such that:

• tidal cycle A refers to data between 18:00 on the 28 August 02:00 on the 29 August

• tidal cycle B refers to data between 06:00–14:30 on the 29 August.

4.4.1 GNSS-derived tidal heights

The RTKLIB software (RTKLIB, 2018) has a number of options for post-processing GNSS data. Table 4.2 shows the general settings that produced the best overall solutions. GNSS data from GPS and global navigation satellite system (GLONASS) satellites were post-processed in 'kinematic mode' with respect to a land-based reference station Post-processed kinematic (PPK) mode is an alternative technique to real-time kinematic (RTK) and differs in that the solution algorithms can be

applied both forward and backward (to increase the accuracy of the overall solution) and more accurate timing corrections can be applied later. Also, the elevation mask was set to 15° above the horizon (i.e., only using satellite data with angles from horizon greater or equal to 15°). The difference to a previous set-up (Knight et al., 2020) was to allow the RTKLIB software to use the GLONASS data to resolve ambiguities; this did slightly improve the results with ~5% more fixed solutions.

Table 4.2: Parameter settings for the post-processing using RTKLIB

Parameter	**Value**
Solution	Kinematic
Frequency	L1
Sensor dynamics	On
Earth tides	Off
Ionosphere	Broadcast
Troposphere	Saastamoinen
Ephemerides	Precise
Satellite system	GPS + GLONASS
Ambiguities GPS	Fix & Hold
Ambiguities GLONASS	On

To produce centimetre-accurate solutions, the RTKLIB software uses both the code phase and, in particular, the carrier phase satellite data recorded by the base (static GNSS site at Blackpool) and rover (GNSS buoy) receivers. The software processes the data with an algorithm to determine the exact number of radio wavelengths between the satellites and the base station antenna (a method known as 'ambiguity resolution') and yield either a fixed or float solution. In a fixed solution (referred to as Q=1, this is generally an indicator of a more accurate positional result), the number of wavelengths is a whole number, or integer, and the algorithm is constrained to yield a whole number. A low number of visible satellites, poor satellite constellation geometry, and distance between the rover and the base station is likely to prevent a fixed solution. If the algorithm does not yield an acceptable fixed solution, then the ambiguity is allowed to be a decimal or floating-point number and the solution is known as a float solution (Q=2). Generally, results with Q1 solutions should indicate more accurate positional data than Q2 solutions.

Poorer solutions are often due to cycle slips which occur when the GNSS receiver loses its lock with a satellite; this results in a miss count of carrier phase cycles. These are more likely to occur when the receiver is moving, such as on the GNSS buoy with its horizontal and vertical movements. Cycle slips can be caused by obstructions, high accelerations, reflections, vibration or lack of a suitable antenna ground plane. Once the cycle count is lost the phase-bias estimate (within the RTKLIB software) must be reset and re-converged and this can take up to a minute or longer to recover.

The satellite data recorded in Rinex format from both the rover and base stations were processed in two parts; covering tidal cycle A and tidal cycle B respectively. Table 4.3 shows the percentage of fixed to float solutions. Q1 percentages shown in Table 4.3, ranging from 48.4% to 57.0% indicate that at times during the deployment the GNSS receiver on the buoy was being affected by one or more of the conditions mentioned above. In contrast, the same GNSS buoy was used in a previous deployment in a relatively sheltered part of the harbour at Holyhead (Knight et al., 2020) and obtained almost 100% of Q1 solutions. Therefore, to further explore the cause of these lower Q1 percentages, the track (East-West versus North-South), individual positional components (North-South, East-West and Up-Down) and vertical accelerations for tidal cycle A and tidal cycle B have been plotted in Figures 4.3, 4.4, 4.5, 4.6, 4.7, 4.8 respectively (Q1 solutions are shown in green, and Q2 solutions shown in orange).

Table 4.3: Percentage of Fixed and Float solutions.

	Fixed Q1 %	**Float Q2 %**
Tidal cycle A	57.0	43.0
Tidal cycle B	48.4	51.6

4.4.2 GNSS buoy track

The buoy tracks during tidal cycles A and B (Figures 4.3 and 4.4, respectively) each display a rotational movement around the anchor point. There is a consistent northerly component during both flood tides (tidal cycle A 18:00–21:30, tidal cycle B 06:30–10:30) with a small increasing component towards the shore suggesting strong alongshore currents during the flood tide. During tidal cycle A, there was a consistent moderate breeze (11–15 knots) from the west; during tidal cycle B, there was an increasing fresh breeze (17–21 knots) from the south-west. The weather conditions also would have contributed to the dominant northerly orientation during the flood tide.

Shortly after high water in tidal cycle A, the rotation increases clockwise towards the shoreline, with its closest position to the shore being around 22:00, around 90 minutes after high water. It then continues to rotate clockwise until 23:00 when it then begins an anti-clockwise rotation passing the

same position around 00:30. A similar pattern can also be seen with tidal cycle B. This could indicate water recirculation as tidal currents decrease, and being constrained by the short length (~100m) rock groynes both to the north and south of the site. It is interesting to note that the majority of good consistent solutions (Q1) occurred shortly after high water and during the ebb tide, while the poorer solutions (Q2) occurred during the flood tide.

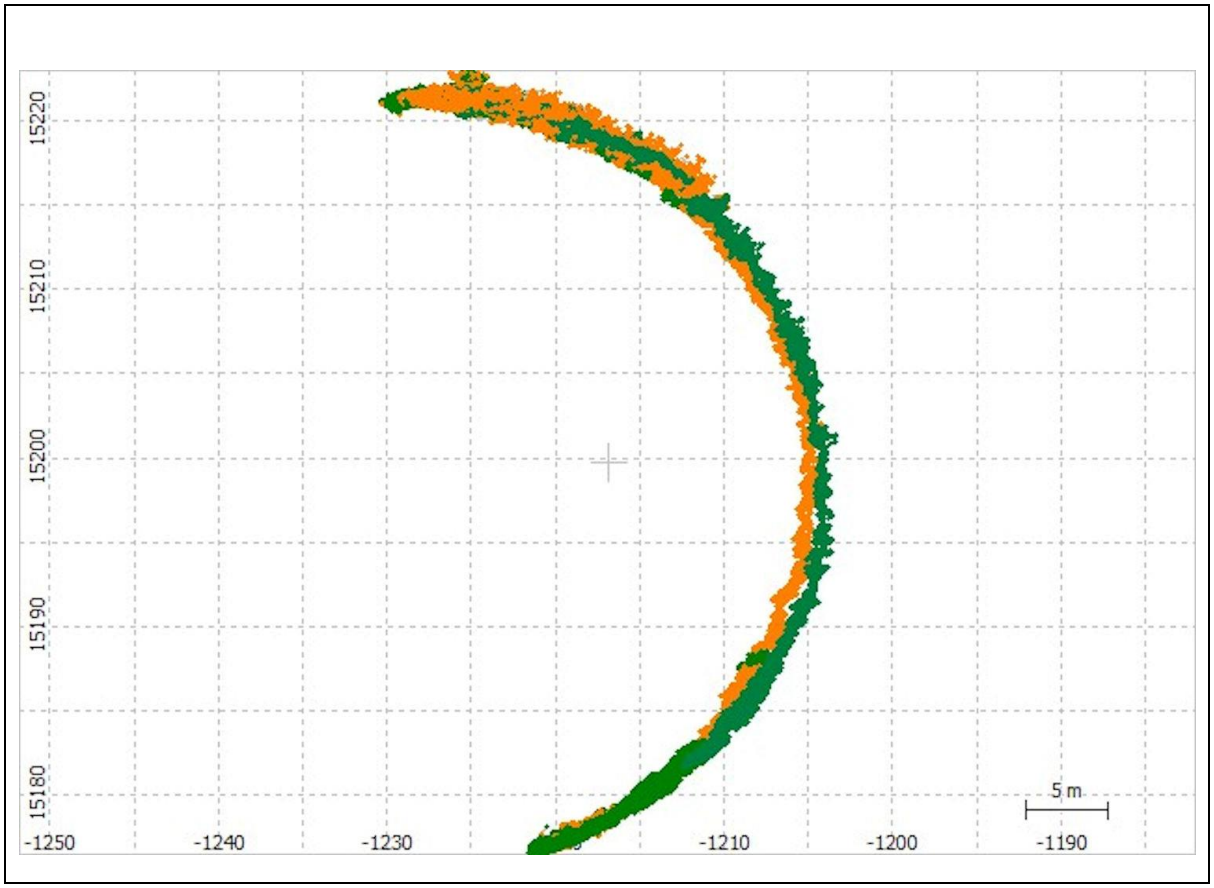

Figure 4.3: Buoy track during tidal cycle A, 18:00 28 August – 02:00 29 August. Fixed solutions (Q1) are shown in green, and float solutions (Q2) are shown in orange. X-Y scale in metre units based upon origin of base station.

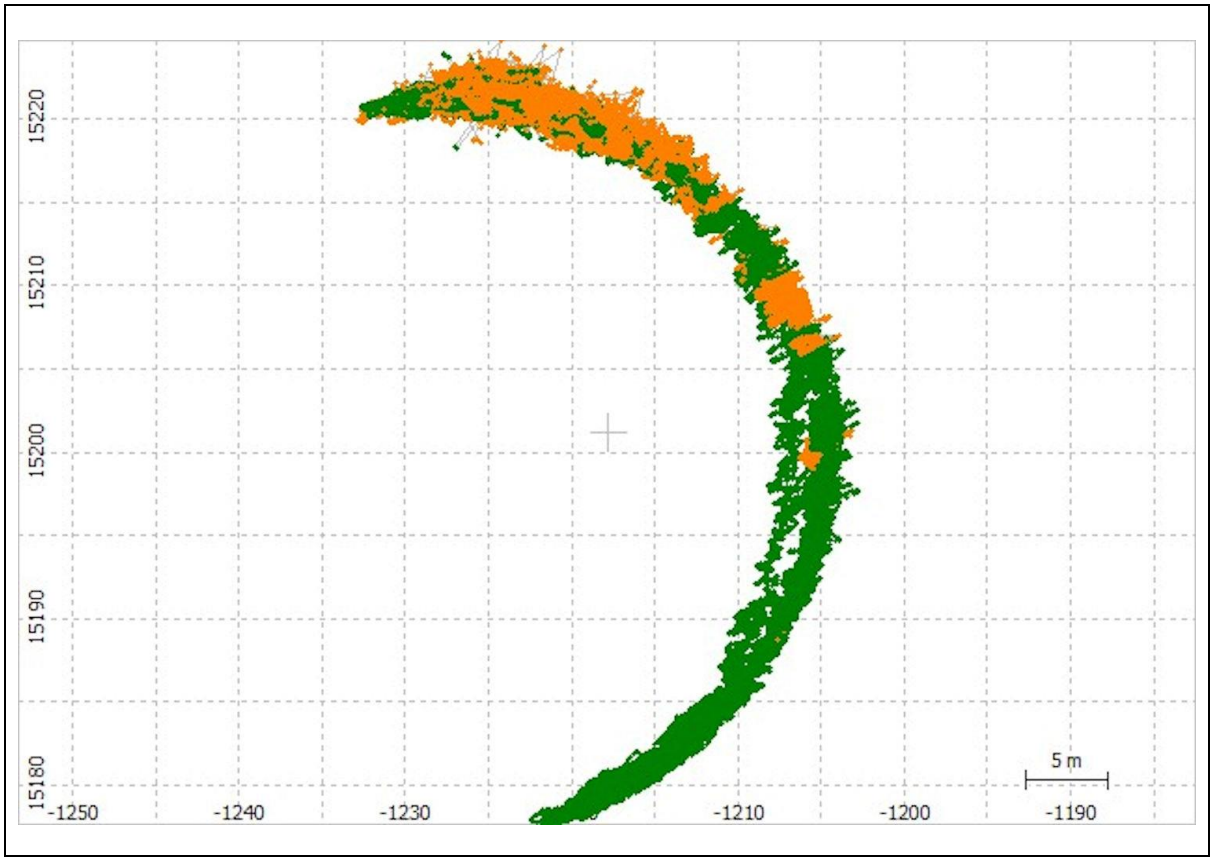

Figure 4.4: Buoy track during tidal cycle B, 29 August 2019 06:00–14:30. Fixed solutions (Q1) are shown in green, and float solutions (Q2) are shown in orange. X-Y scale in metre units based upon origin of base station.

4.4.3 GNSS buoy positional components

The buoy's positional components during tidal cycles A and B are in Figures 4.5 and 4.6, with East-West (E-W), North-South (N-S) and Up-Down (U-D) components. The poorest (Q2) solutions occurred more frequently during each flood tide: at maximum tidal current and on the approach towards high water. Also, it is likely that the poor solutions at the start and end of both tidal cycles A and B were caused by the buoy being buffeted by small waves before becoming free-floating, i.e., with the central vertical bar catching the sand as the buoy moved with the small breaking waves.

The poorest Q2 solutions occurred during each flood tide and when the buoy was within the surf zone, and being affected by spilling waves. The buoy tracks (Figures 4.3 and 4.4) suggest that the mooring line was under tension during the peak tidal flows on the flood tide, which may indicate the presence of relatively strong alongshore currents. When coincident with spilling waves this would briefly allow water to cover the antenna, resulting in loss of satellite lock; this type of effect can be seen clearly within the sea-level data.

Some Q1 solutions were obviously erroneous with large jumps (e.g., Figure 4.5, U-D ~ 00:45 29 August). This was likely due to the processing software not recovering from poor and limited satellite

data, and the subsequent offset feeding into the following positional solutions; therefore, Q1 solutions are not always an indication of good sea-level data.

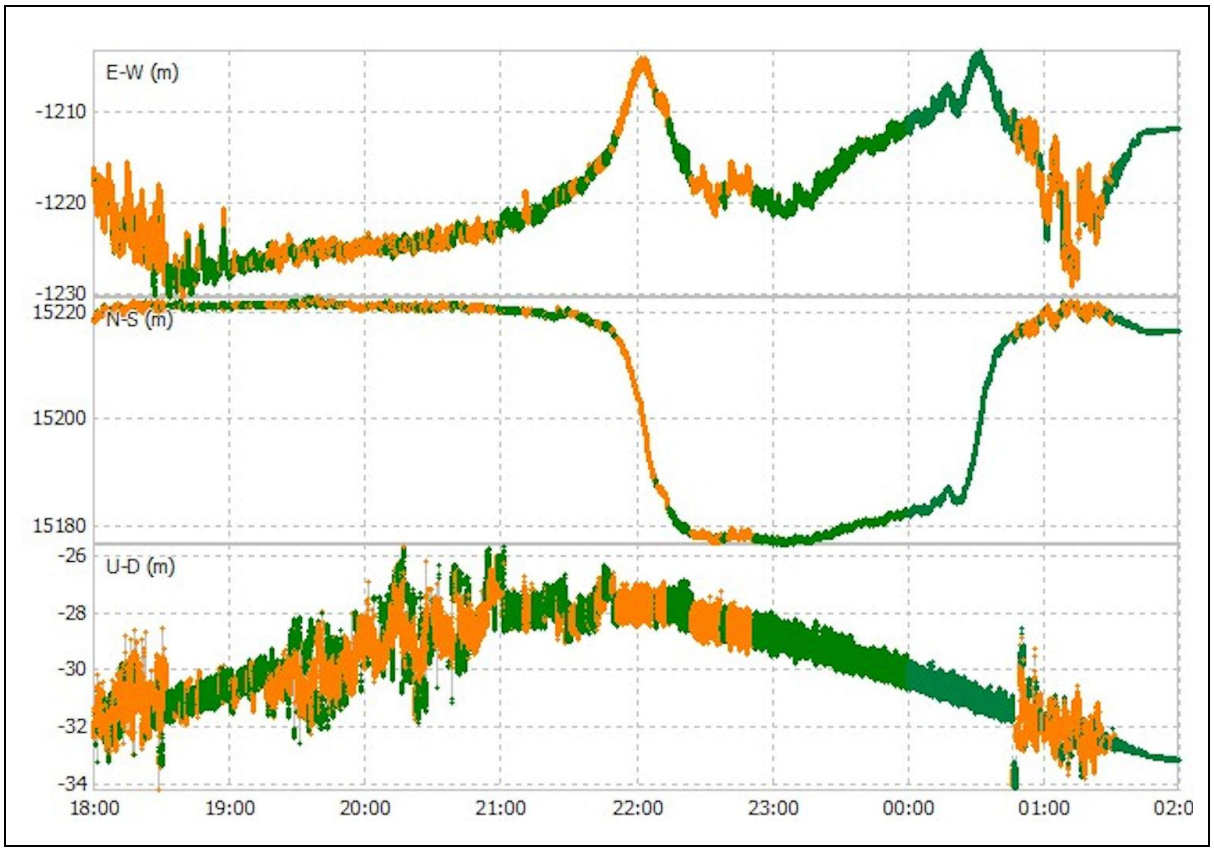

Figure 4.5: Buoy positional components during tidal cycle A; East-West (E-W), North-South (N-S) and Up-Down (U-D), 18:00 28 August – 02:00 29 August. Fixed solutions (Q1) are shown in green, and float solutions (Q2) are shown in orange.

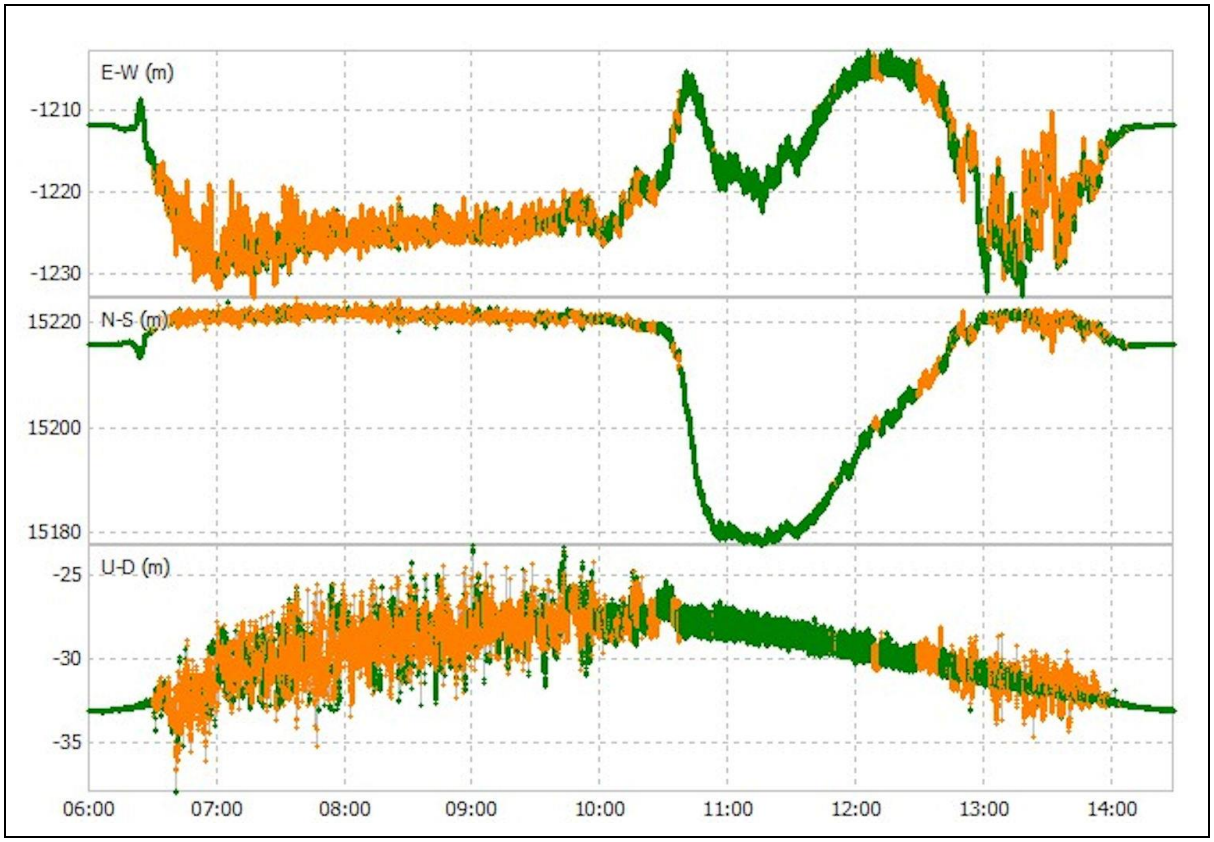

Figure 4.6: Buoy positional components during tidal cycle B; East-West (E-W), North-South (N-S) and Up-Down (U-D), August 29 2019 06:00–14:00. Fixed solutions (Q1) are shown in green, and float solutions (Q2) are shown in orange.

4.4.4 GNSS buoy vertical accelerations

Most of the poor solutions, with the greatest vertical differences, coincide with very large accelerations (Figures 4.7, 4.8), mainly during the flood tides and when the buoy is in shallower water. When large accelerations occurred, the GNSS receiver Rinex data also indicated loss of satellite lock for the majority of visible satellites. Normal practice to improve the analysis when this happens is to experiment with increasing the satellite angle cut off, e.g., 16°, 17°, 18° etc., ignoring any data with lower satellite angles. Unfortunately, this did not improve the solutions since the lock problem was occurring simultaneously on all the satellites. In fact, it produced progressively poorer solutions due to smaller numbers of useable satellites for the RTKLIB software. It is likely that these poor solutions are occurring when the antenna is becoming covered in water from spilling waves, which were observed on a number of occasions from the shore; the mooring could be seen to be physically jerked backwards as the wave passed through. For example, the GNSS buoy (photograph in Figure 4.9) prior to recovery on the 29 August at 13:24: large accelerations were observed in the satellite data (Figure 4.8). In this case, white water was seen behind the buoy and it eventually washed over it and this coincided with the high recorded accelerations and loss of satellite lock, and thus a poor positional solution.

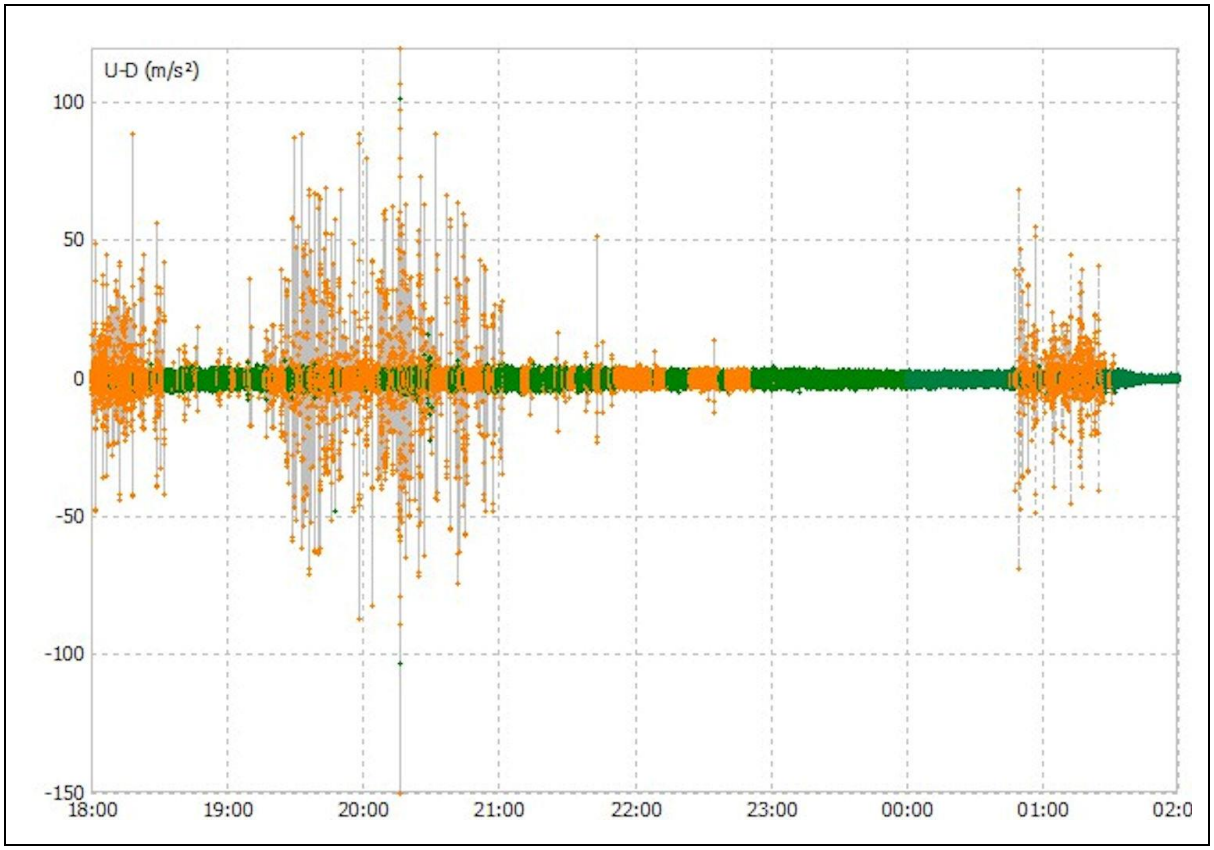

Figure 4.7: Buoy vertical accelerations during tidal cycle A; 18:00 28 August – 02:00 29 August. Fixed solutions (Q1) are shown in green, and float solutions (Q2) are shown in orange.

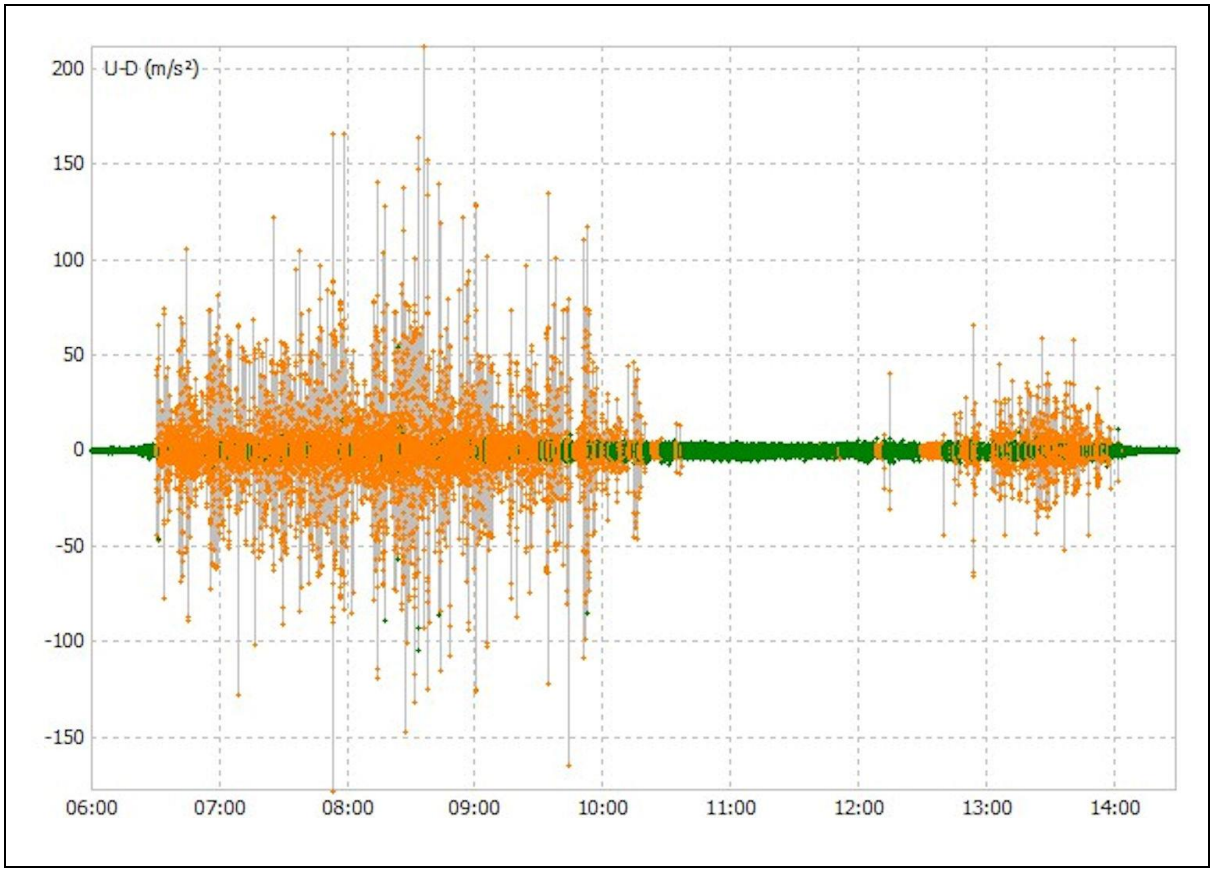

Figure 4.8: Buoy vertical accelerations during tidal cycle B; Up-Down (U-D), 29 August 06:00 – 14:30. Fixed solutions (Q1) are shown in green, and float solutions (Q2) are shown in orange.

Figure 4.9: GNSS buoy at 13:24 on 29 August, prior to recovery; spilling waves can be seen in the background.

4.5 Analysis and discussion

4.5.1 Buoy performance

On recovery, there were a number of twists in the rope connection between the GNSS buoy and the trawl float. An additional swivel on the end of the GNSS buoy connection would probably have reduced this and may lead to a more stable and free-floating platform. The use of a rubber bungee directly below the wave buoy mooring (Brown et al., 2021) might be worth incorporating in this mooring in future. Both these suggestions may allow more free movement in the strong alongshore currents during the flood tide and thus improve data quality. Also, the anchor point was completely covered with about 0.25m of sand over just a couple of tidal cycles, so the bottom swivel was probably not working as intended by the end of this period. Overall, the mooring arrangement appears to have worked well and coped without being damaged in a very dynamic part of the intertidal beach. If the deployment was further away from the sea defences and nearer the low water mark, then spilling waves may have less impact on the results due to spending less time in the surf zone. Other

authors observed the reverse (Brown et al., 2021) since they had to site their mooring closer to shore so as to pick up the breaking/spilling waves.

4.5.2 GNSS receiver performance

Instead of a single frequency (L1) receiver, a dual frequency (L1, L2) receiver could be substituted and this would improve accuracy by providing more data for processing by the RTKLIB software. Since this experiment was conducted, Emlid Reach have produced an upgrade to the receiver for a similar cost (e.g., using a F9 U-blox dual frequency GNSS receiver). It also supplies a helix antenna, an improvement on the patch antenna; its larger design would reduce the problem with spilling waves, and be less susceptible to reflections (which increase the Signal to Noise ratio). Use of a duplicate set-up for both rover and base station, both recording at 5Hz (in this experiment, the base station was recording at 1Hz) would eliminate problems associated with unknown antenna bias (with the patch antenna) (Knight et al., 2020), and would allow additional options in the RTLKLIB software to be used, which would then likely improve the position solutions.

4.5.3 Sea levels

Derived tidal heights relative to chart datum for tidal cycle A are in Figure 4.10, while Figure 4.11 shows the corresponding results for tidal cycle B. Tide gauge data from Liverpool and Heysham have been added for comparison with those obtained from the GNSS buoy. A 15-minute (900-second 'boxcar') moving average was applied to the buoy data before comparison with the 15-minute Liverpool and Heysham tide gauge data. Both Figures 4.10 and 4.11 emphasise the periods of good data during the ebb tide (e.g., comparison with GNSS 900s average and Liverpool 15-minute data; mean difference -0.02m, standard deviation difference 0.03m and RMSE difference 0.04m) and poorer data during the flood tide. While the tidal characteristics between Liverpool, Heysham and Rossall are similar, there are small but significant differences in the tidal elevations and times of LW and HW (Table 4.1), thus these comparisons are considered indicative of data quality, i.e., good data quality during the ebb periods.

During the ebb tide the 15-minute GNSS buoy data matches the Liverpool tide gauge data more closely in both timing and elevation, even though the Heysham tide gauge is nearer. The larger differences between the GNSS buoy and the Heysham tide gauge data are probably due to Heysham being at the edge of Morecambe Bay (with the accompanying dynamics of a larger intertidal zone, and the water being initially directed along the Lune Deep channel at low water). However, on the ebb tide there are some good data between 18:30–19:30 on 28 August (Figure 4.10) which indicate timing differences compared with the Liverpool tidal data. Again, both Figures 4.10 and 4.11 show there are poorer data as the water at the buoy approaches 'drying out'.

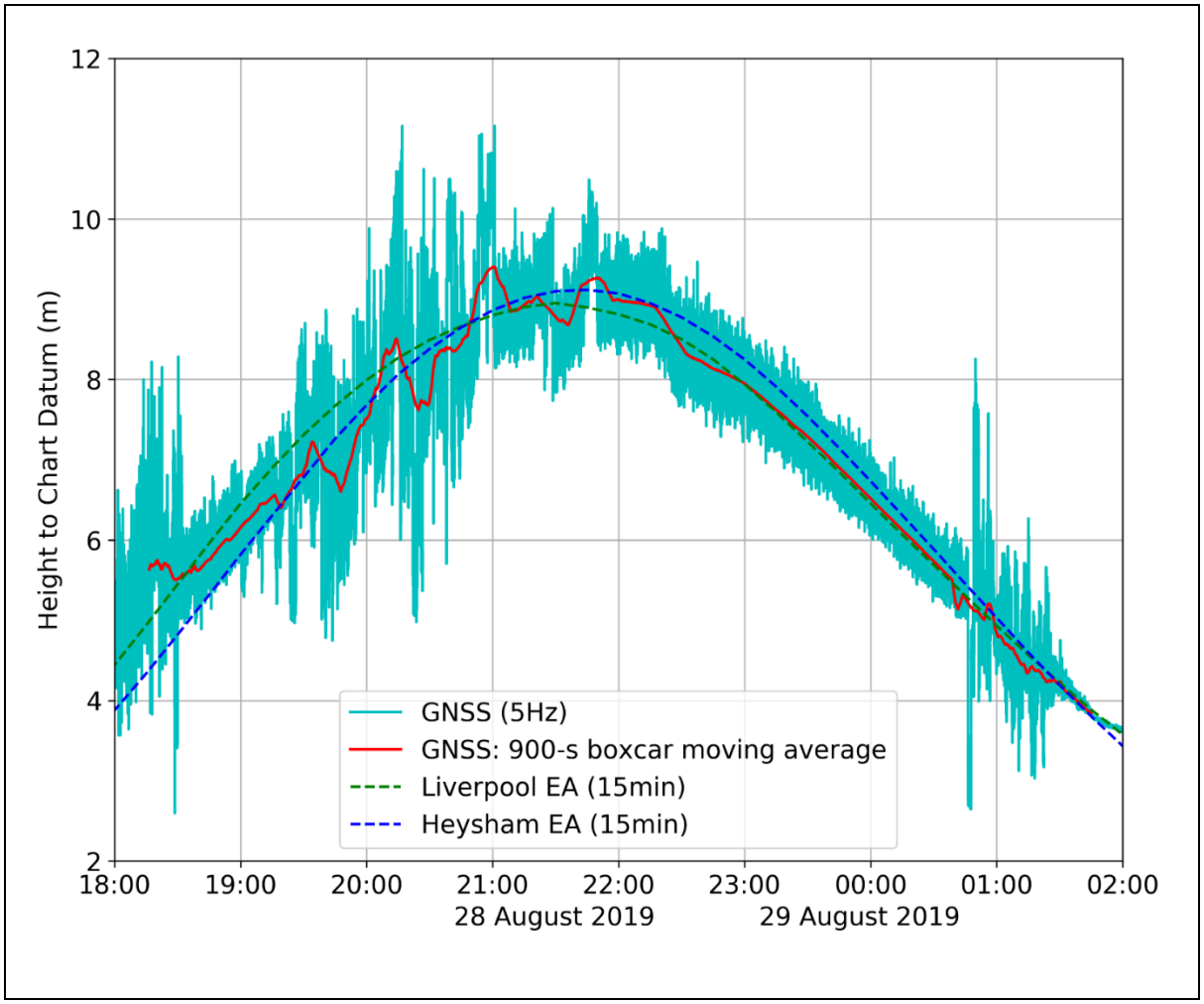

Figure 4.10: Comparison of the GNSS buoy derived sea levels for **tidal cycle A** and established tide gauges at Liverpool and Heysham. Note: after high water the 900-s boxcar moving average can be seen to match the 15-minute Liverpool tidal data.

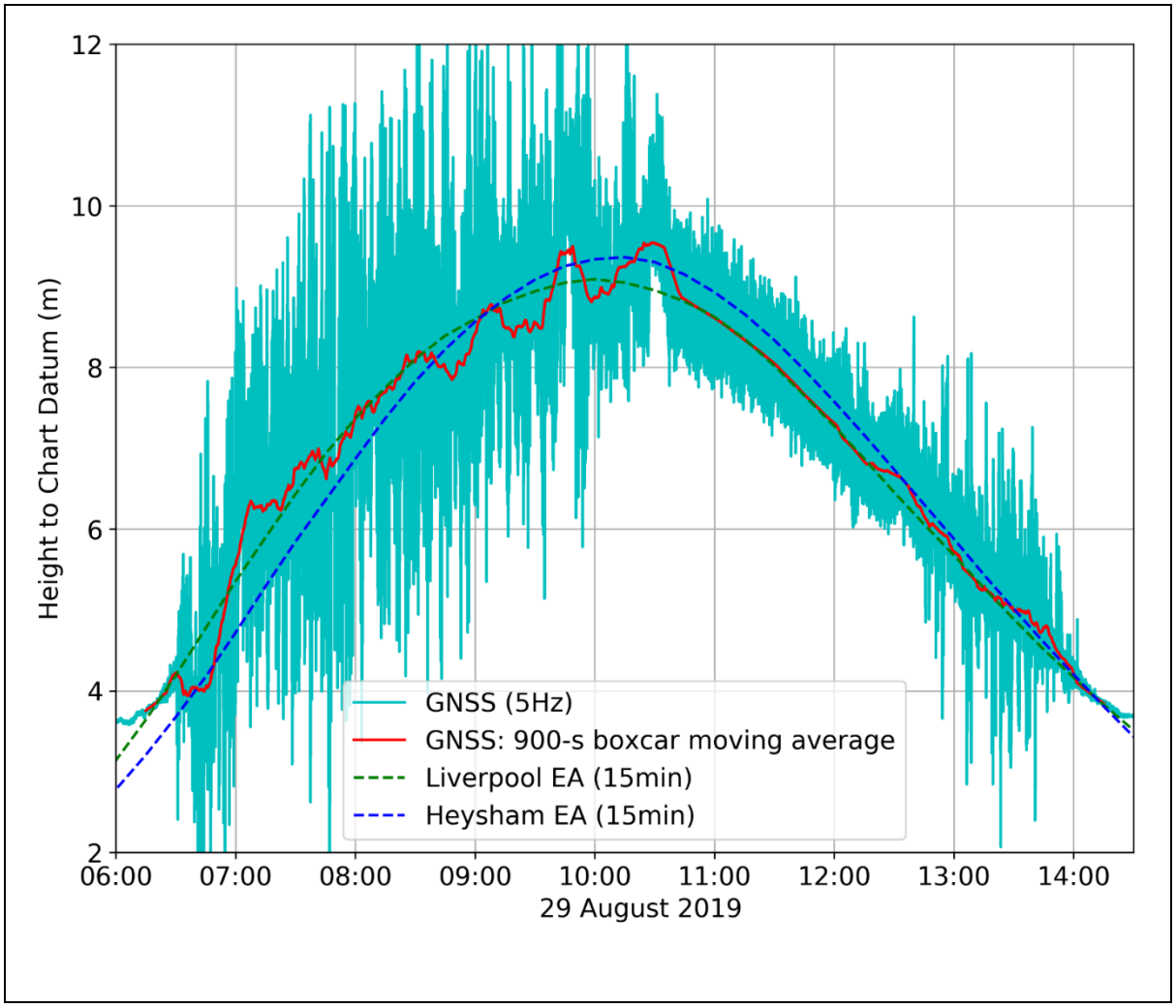

Figure 4.11: Comparison of the GNSS buoy derived sea levels for **tidal cycle B** and established tide gauges at Liverpool and Heysham. Note: after high water the 900-s boxcar moving average can be seen to match the 15-minute Liverpool tidal data.

4.5.4 Wave characteristics

The power spectral density of GNSS buoy tidal elevations (Figure 4.12) show that for tidal cycle A, the resultant peak frequency corresponds to a wave period of 5.3 seconds, whereas tidal cycle B has a peak frequency corresponding to a wave period of 5.1 seconds.

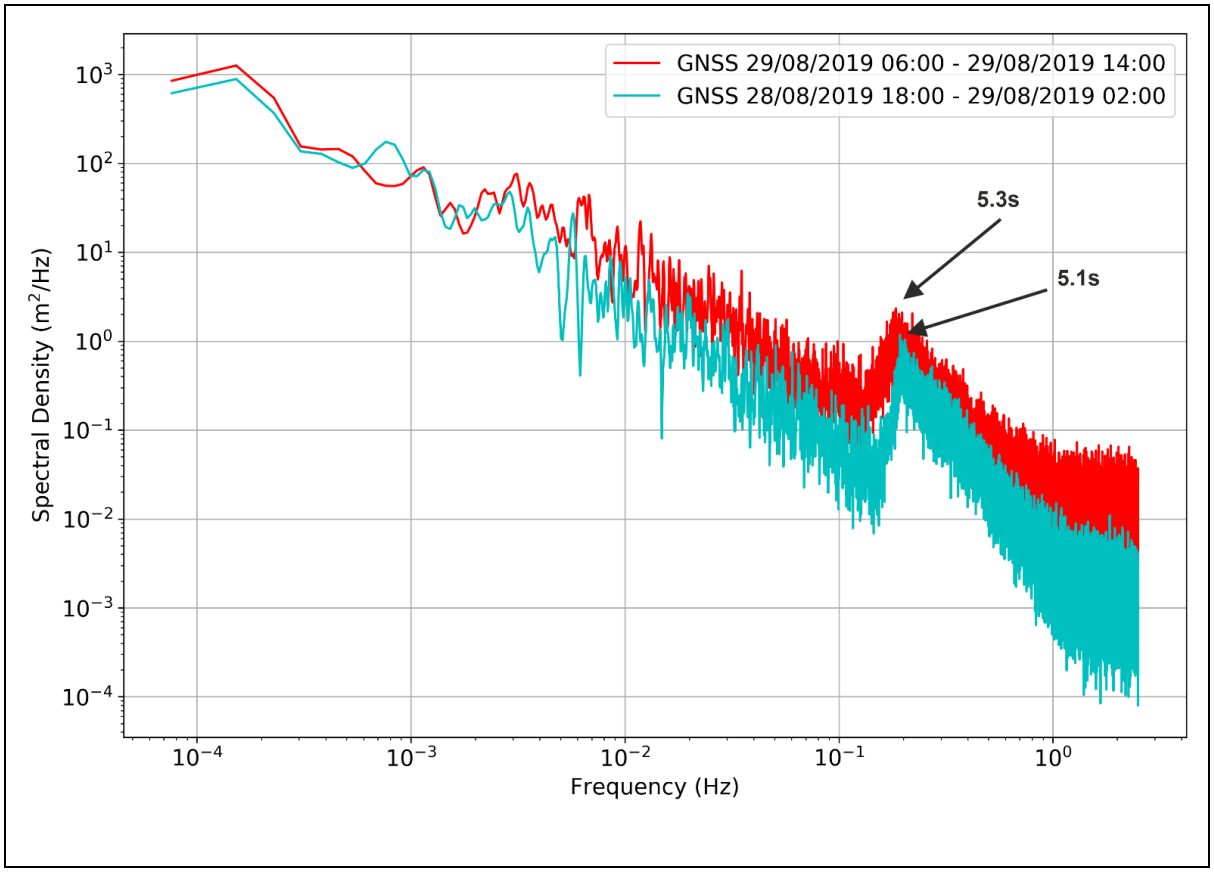

Figure 4.12: Spectral density for tidal cycle A (cyan) and tidal cycle B (red).

Figure 4.13 a-d shows the power spectral density results from the Cleveleys wave buoy over two-hour periods before and after high water for comparison with the GNSS buoy (see Table 4.4). The significant wave heights were estimated by calculating four times the square root of the area from under the peak of spectral density (Fiorentino et al., 2019) between the frequency bands 0.5 Hz and 0.125 Hz.

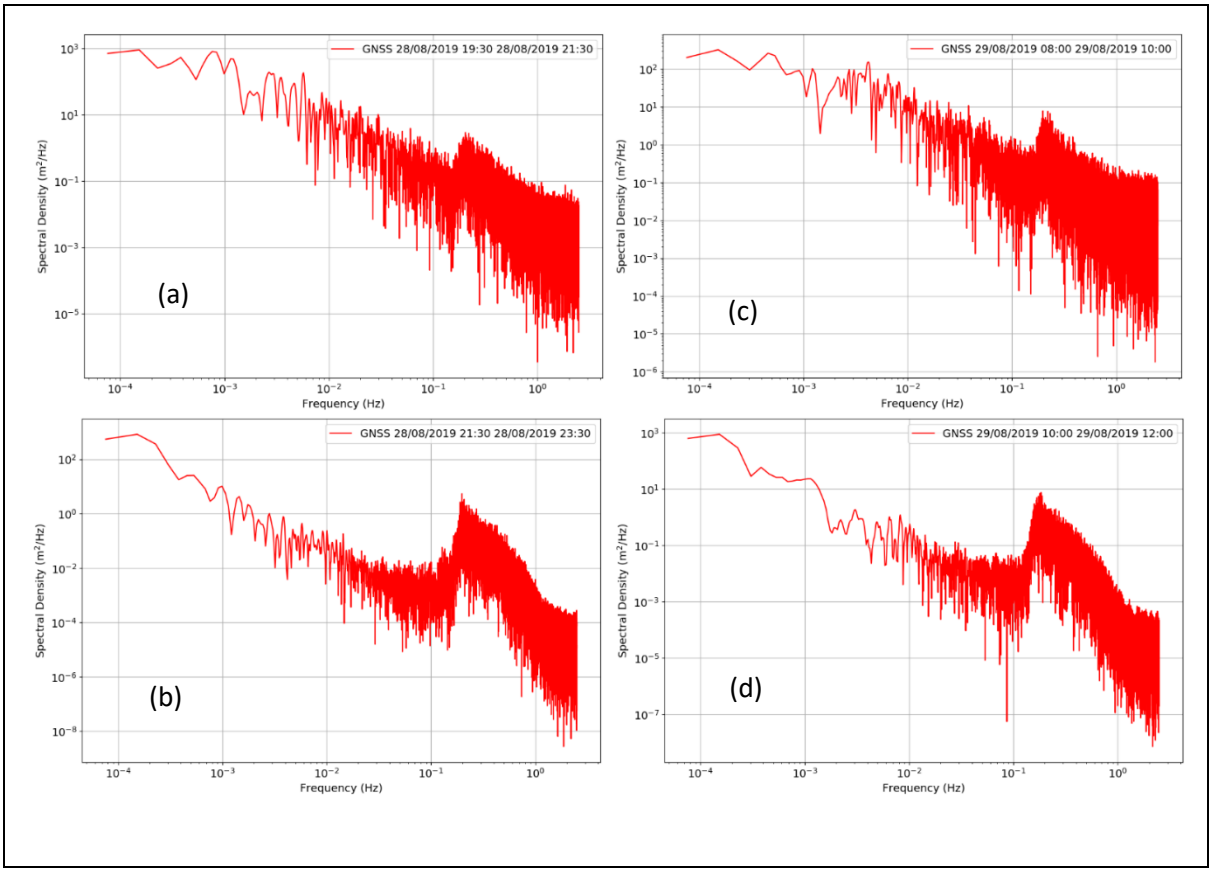

Figure 4. 13: Spectral density for tidal cycle A - (a) 2 hr period before HW, (b) 2 hr period after HW, and tidal cycle B - (c) 2 hr period before HW, (d) 2 hr period after HW.

Table 4.4: Wave parameter comparisons between the GNSS buoy and the Cleveleys wave buoy for two-hour periods either side of High Water (HW).

		Significant wave height		**Spectral peak period**	
		GNSS buoy	**Cleveleys buoy**	**GNSS buoy**	**Cleveleys buoy**
Tidal cycle A	2 hr period before HW	1.1m	0.9m	4.8s	5.0s
	2 hr period after HW	1.0m	1.0m	5.0s	4.8s
Tidal cycle B	2 hr period before HW	1.5m	1.5m	4.7m	4.8s
	2 hr period after HW	1.3m	1.6m	5.4m	5.3s

The GNSS buoy results compare well with the Cleveleys wave buoy data, giving similar significant wave heights and spectral peak periods. Significant wave height differences vary between 0.0 and 0.3m, however in general they are a very close match and indicate that the GNSS buoy is capable of measuring waves as well as a commercial wave buoy. Differences in spectral peak periods within 0.1 seconds are also very similar. The results here also indicate that wave heights and wave periods increased over the two tidal cycles, and this can also be seen in the sea level data variations (Figures 4.10 and 4.11).

4.6 Conclusion

The GNSS buoy recorded data in very challenging conditions and provided both sea-level and wave data. These GNSS data show that the tidal elevations are a closer match to tide gauge data at Liverpool than at Heysham, although there may be subtle differences especially the during the flood tide, however during the ebb periods the comparison with GNSS 900-s average and Liverpool 15-minute data produced a mean difference −0.02m, standard deviation difference 0.03m and RMSE difference 0.04m. Also, the GNSS buoy recorded almost indistinguishable significant wave heights (differences between 0.0 and 0.3m; Table 4.4) and wave periods (differences between 0.1 and 0.2 seconds; Table 4.4) to that measured by the Cleveleys wave buoy. It was possible to extract wave data from the poorer positional solutions during the flood tide and when there were large accelerations in the GNSS buoy.

Overall, the deployment over two tidal cycles has shown that the GNSS buoy can perform within the intertidal zone, and provide acceptable sea-level and good quality wave data. In addition, it was demonstrated that these data can also be downloaded remotely which would allow for timely analysis. This approach offers considerable efficacy for determining local hydrodynamics in support of coastal monitoring or defence scheme implementation.

4.7 Funding

The research is part of a PhD study funded by the “Low Carbon Eco-Innovatory (LCEI)—Liverpool University” (www.liverpool.ac.uk/environmental-sciences/working-with-business), with industrial partner MM Sensors Ltd.

4.8 Acknowledgments

The authors would like to thank Carl Green and Chris Atherton at Wyre Council for general support, and Colin Bell at the National Oceanography Centre for access to the POLTIPS-3 coastal tidal prediction software. The research is part of a PhD study funded by the “Low Carbon Eco-Innovatory (LCEI)—Liverpool University” (www.liverpool.ac.uk/environmental-sciences/working-with-business), with industrial partner MM Sensors Ltd. This paper contributes to Work Package 4 of the UK NERC-funded BLUEcoast project (NE/N015614/1).

5 Characterising temporal and spatial change in intertidal morphology using LiDAR and radar derived Digital Elevation Models (DEMs)

5.1 Abstract

A combination of LiDAR and X-Band radar-derived digital elevation models have been used to characterise the intertidal zone of a macro-tidal estuary. Over the three-year study period, cycles of deposition and erosion ranged from gains of 0.40 m per masked area, to losses of 0.14 m per masked area. Morphological changes on the tidal flats around Hilbre Island appear to be related to the tidal range and number of 'geomorphologically significant days' (days with >=0.9 m waves heights with tidal heights >= mean high water neap levels). Also, an analysis of the DEMs reveals the presence of low-amplitude ridges about 0.5 m high and 25–50 m wide, which propagate towards the shoreline at rates of 25–75 m per year. These are located mainly between the mean sea level (MSL) and the mean high water neap (MHWN) tidal level. While mobile, they appear to be permanent features within these bounds.

5.2 Introduction

The intertidal zone is an important part of the coastline and provides the first line of defence against storms and extreme sea levels (Turner et al., 2007). Where the intertidal zone takes the form of sandy beaches and tidal flats it can be affected by a combination of winds, waves, currents and tides. This can result in episodes of erosion and deposition lasting from days to weeks, some due to individual storm events and others as part of seasonal patterns of change. Coastal engineers therefore routinely monitor beaches around vulnerable areas and use the information to make decisions about interventions such as beach replenishment (Spodar et al., 2018). Understanding how these natural forcing factors interact with each other to affect intertidal morphology can provide the critical information to carry out or to delay interventions.

Monitoring of beaches has a history extending back to the early 20th century, however experiments have been ongoing since the 1850s (Ton et al., 2020), providing insights into the processes governing the movements of sediment around the intertidal zone. Early work focused on simple techniques such as using 'beach poles' to determine coastline position, which later developed into taking regular profiles along beaches using geographic surveying techniques (Larson et al., 1994). Recent technology development allows less laborious and more spatially extensive techniques to measure the changing beach profiles, and produce digital elevation models (DEMs) mapping the whole beach area.

Beach height measurement methods include: ground survey along transects, stereo-photogrammetry from both aircraft and satellite platforms, airborne scanner laser altimetry using Light Detection And Ranging (LiDAR), Synthetic Aperture radar (SAR) interferometry from both aircraft and satellite, the satellite based waterline, and bathymetry measurement by SAR imaging of water current interaction

(Mason et al., 2000). These methods have evolved and new ones developed over the past twenty years, for example, beach profiles are carried out routinely using terrestrial ground-based LiDAR, and hand-held GPS devices are used extensively for beach surveying by walking the beach or by deploying them with small four-wheel-drive vehicles. Other techniques include using unmanned aerial vehicles (UAV) or 'drones' to fly survey grids while photographing the ground (Zanutta et al., 2020), and using fixed video cameras to monitor the beach (Stringari et al., 2022).

Annual and twice a year Airborne LiDAR data have previously been used to characterise intertidal bar morphodynamics (Miles et al., 2019; Montreuil et al., 2020). Intertidal bars are common features on macro-tidal sandy beaches with low to moderate wave energy environments (Biausque et al., 2020; Masselink et al., 2006). Intertidal bars are shore-parallel features which comprise at least one intertidal bar crest and shoreward trough or depression. Classification, based on tidal range and beach slope or width, separates these features into swash bars, sand waves, and ridges and runnels. Ridges and runnels are also classified as low-amplitude ridges (Masselink et al., 2006).

Analysis of nine LiDAR surveys, spanning 17 years, at a beach in northwest England showed that intertidal bars were obliquely orientated with the alignment of dominant wave direction, and became narrower and steeper as they migrated onshore (Miles et al., 2019). Furthermore, analysis of seven years of twice-yearly LiDAR data from a beach in Belgium revealed that while intertidal bar morphology is permanently present on the beach, individual features were dynamic and highly mobile over the survey periods (Montreuil et al., 2020). The authors reported the most dynamic part of the beach was between the mean sea level (MSL) and mean high water neap (MHWN) tide level, and that seasonal variability of the bar morphology was moderately related to seasonal storm and wave forcing parameters.

Airborne LiDAR surveys are expensive to undertake and this often restricts their temporal availability, and surveys of macro tidal beaches have to be flown during low spring tides to gain maximum coverage of the intertidal zone. These surveys provide very accurate vertical elevation data, and the associated vertical errors are consistent across the full spatial extent (Saye et al., 2005).

Supplementing the periodic LiDAR surveys, marine X-Band radar allows continuous monitoring of coastal morphology and morphological change over timescales from days to years (Bird et al., 2017). The morphology of beaches and tidal flats can be characterised in terms of their instantaneous and long-term behaviours by applying a water-line method (Bell et al., 2016), where the advancing and retreating shoreline during the tidal cycle can be assigned an altitude based on the corresponding tidal level.

In contrast to the LiDAR method, X-band radar can provide many more DEMs at a much lower cost, but the vertical errors are inconsistent across the full spatial extent. The accuracy can vary from an over-estimation of 0.12 m within the first 0.75 km of the radar, to an approximate over-estimation of

0.5m further away (Bell et al., 2016). However, the elevation errors at each cell in the DEM appear to be relatively stable over time. This was verified using fixed rock targets within the spatial domain, and would thus provide confidence in the relative changes in beach morphology identified between subsequent composite X-Band radar DEMs (Bell et al., 2016; Bird et al., 2017).

This research uses DEMs derived from data collected between 2006–2008 (Bell et al., 2016) along with annual LiDAR data and forcing parameters such as waves, tides and storm surges, to characterise morphological change during the three-year survey period. Finally, it outlines how additional localised tidal and wave measurements would improve data quality, and hence the usefulness of X-band radar technology in a coastal monitoring programme.

5.3 Dee Estuary and study area

The Dee estuary is a macro-tidal, funnel-shaped coastal-plain estuary in the eastern Irish Sea (Figure 5.1). It has an exceptionally large tidal range: for example, at Hilbre Island, the difference between highest astronomical tide (HAT) and lowest astronomical tide (LAT) levels is 9.72m. During the experiment period (1 March 2006 to 30 November 2008) the highest predicted tide was 10.03 m, the lowest predicted tide was 0.23 m, and the largest range was 9.64 m. The vertical datum used in this paper is chart datum (CD), where CD is 4.93 m below ordnance datum Newlyn (ODN).

The estuary exhibits flood-dominated asymmetry (Moore et al., 2009) with an average flood time of around 5 hours 40 minutes, and an average ebb time of around 6 hours 44 minutes (National Oceanography Centre 2019). This particular tidal distortion produces higher flow velocities during the flood compared to the ebb, which can lead to greater sediment resuspension, leading to net sediment transport into the estuary. In the outer part of the estuary the main channel bifurcates, resulting in two deep channels extending into Liverpool Bay. One of these channels is located on the southwestern side of Hilbre Island, and currents can reach $0.75 ms^{-1}$ during Spring Tides (Bolaños et al., 2010).

While the Irish Sea is subject to severe winter storms and wind speeds that are often greater than 20 ms^{-1}, the waves in Liverpool Bay are mainly generated locally so that long period swell is absent (Wolf et al., 2011). Significant waves heights are below 5.5 m, and the largest waves are associated with winds from the west and northwest (where the fetch is the longest), with the peak wave period less than 12 s and the mean wave period less than 8 s (Wolf, 2008).

The study area focuses on 6 km^2 of the intertidal zone on the northeast corner of the Dee Estuary (Figure 5.1). This area can be categorised into three distinct regions based on the local geology: regions A and C to the north of the island chain, and region B to the south.

Region A

Located to the northeast of a ridge of rocky outcrops, this region extends diagonally from the northwest to southeast, and along a line incorporating Hilbre Island, Little Hilbre, Little Eye and Tanskey Rocks. On the northern side of this ridge a small channel extends from Little Eye to Hilbre Island; the channel drains this part of the beach during the ebb tide in the direction of Hilbre Island and completely dries out to the low water mark. The north-eastern part of this area is exposed to the northwest, the biggest fetch, and thus the largest waves.

Region B

This region is exposed to the west and northwest, and is situated to the southwest of the ridge of higher ground which constitutes the island chain. This area also runs parallel to the Hilbre Channel, a relatively deep channel (~18 m below CD); one of two main channels extending into Liverpool Bay. As well as being exposed to the northwest it is also subject to waves from westerly directions.

Region C

Generally contained above the 8 m CD contour, this region is the closest to the mainland, encompassing the beach adjacent to the Royal Liverpool Golf Club. This part of the beach is relatively flat and is dominated by sand with a small component of mud (Thorne et al., 2021). Parallel to the golf course, there are sporadic clumps of beach grass, which becomes denser landwards, and eventually there is a small dune system with a developing reed bed complex. At the southern end there is a man-made marine lake which is refreshed during large high tides. While this part of the beach is protected by the ridge and islands it can be still be affected by large waves during spring tides.

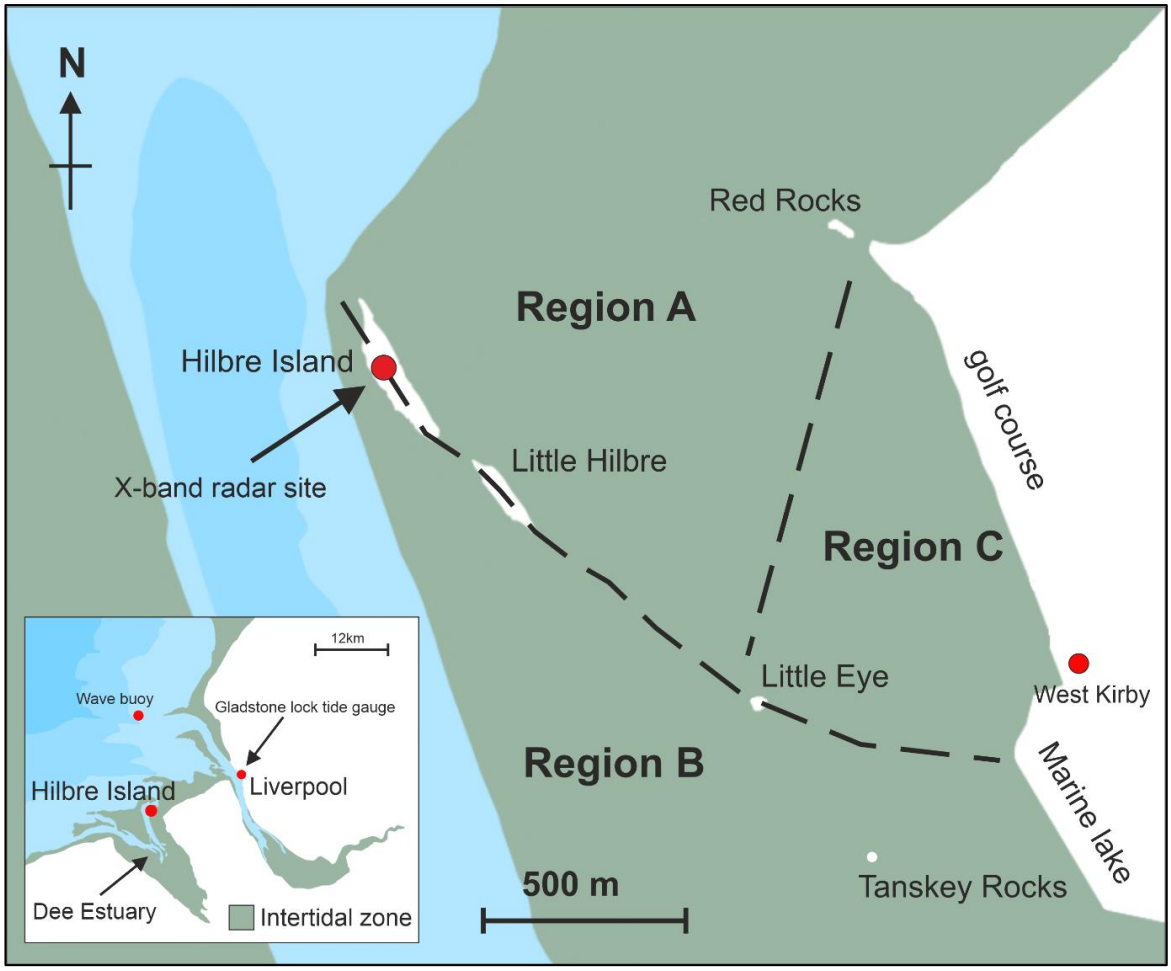

Figure 5.1: Hilbre Island and surrounding intertidal region area; area split into three regions A, B and C, and site of the X-band radar installation. Base map source: EDINA Marine Digimap Service (https://edina.ac.uk/digimap).

5.4 Data analysis and results

5.4.1 LiDAR-derived morphological maps

Airborne LiDAR surveys of the northwest part of the Dee Estuary (Area 136 km^2) were carried out by the Environment Agency in 2006, 2007 and 2008 (EA, 2019a) using an Optech ALTM 3100 system. The resulting morphological maps (Figures 5.2, 5.3 & 5.4) show the elevation contours from 3 to 9m CD. These were flown at times of low water during spring tides to maximise the exposure of the intertidal beach. The 2006 and 2007 surveys were flown on 8 October 2006 and 24 October 2007. The 2008 survey was based on a composite of surveys taken between 18 October and 16 November 2008. The two earlier surveys have horizonal resolutions of 2 m while the latter survey was at 0.25 m resolution, with a quoted vertical accuracy of 0.15 m or better (1x standard deviation); The Environment Agency conducted a ground truth survey of the data which resulted in a RMSE of 0.071 m between the LiDAR and a GPS ground survey (Bell et al., 2016; EA, 2019a).

The LiDAR data were averaged using the ‘average’ resampling algorithm from the Geospatial Data Abstraction Library (GDAL/OGR_contributors, 2022) to allow direct comparison with the following X-Band radar-derived morphological images. “No data” values and data corresponding to the sea surface were passed as ‘−9999’, and converted to “Not a Number” values in MATLAB. These resampled surveys data for 2006, 2007 and 2008 will be now be referred to as the LiDAR-derived Digital Elevations Models (DEM).

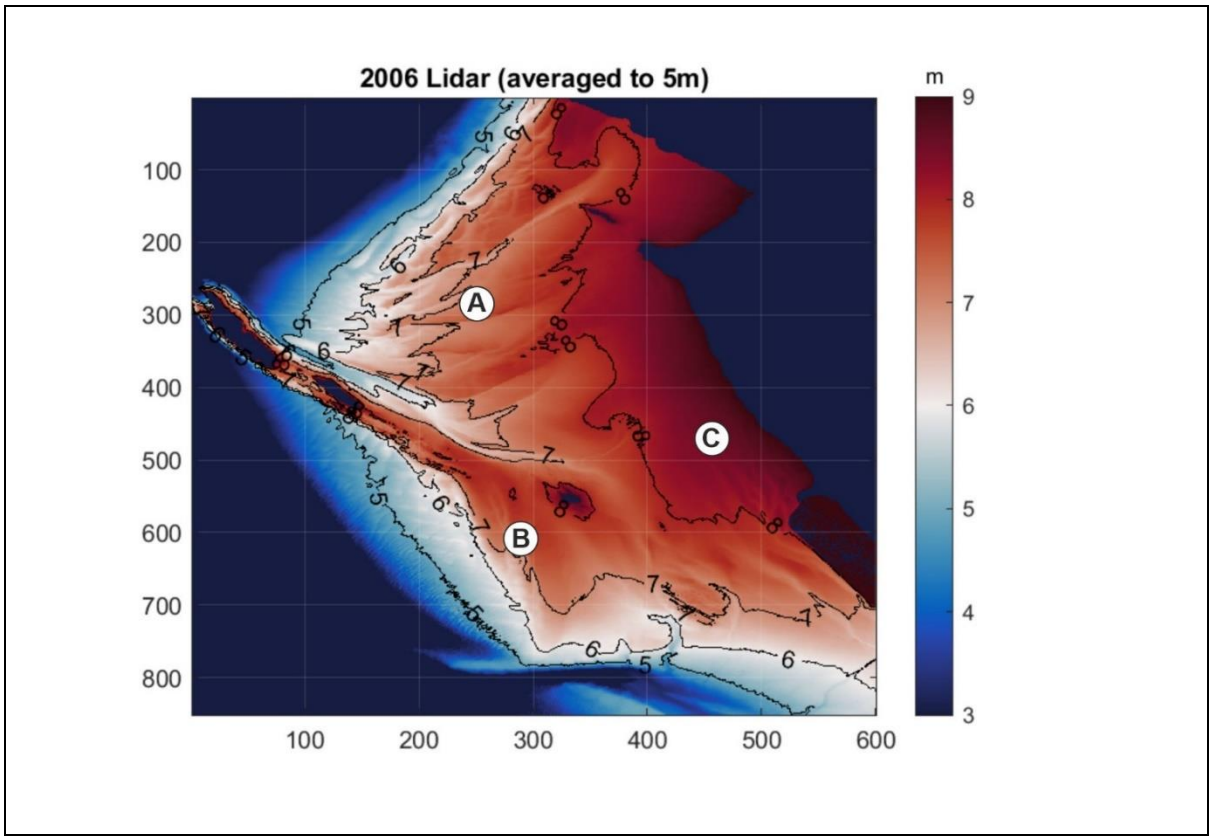

Figure 5.2: Digital Elevation Models derived from 2006 (Oct) LiDAR (Dark blue represents no data, each pixel represents 5m×5m, contours to Admiralty Chart Datum).

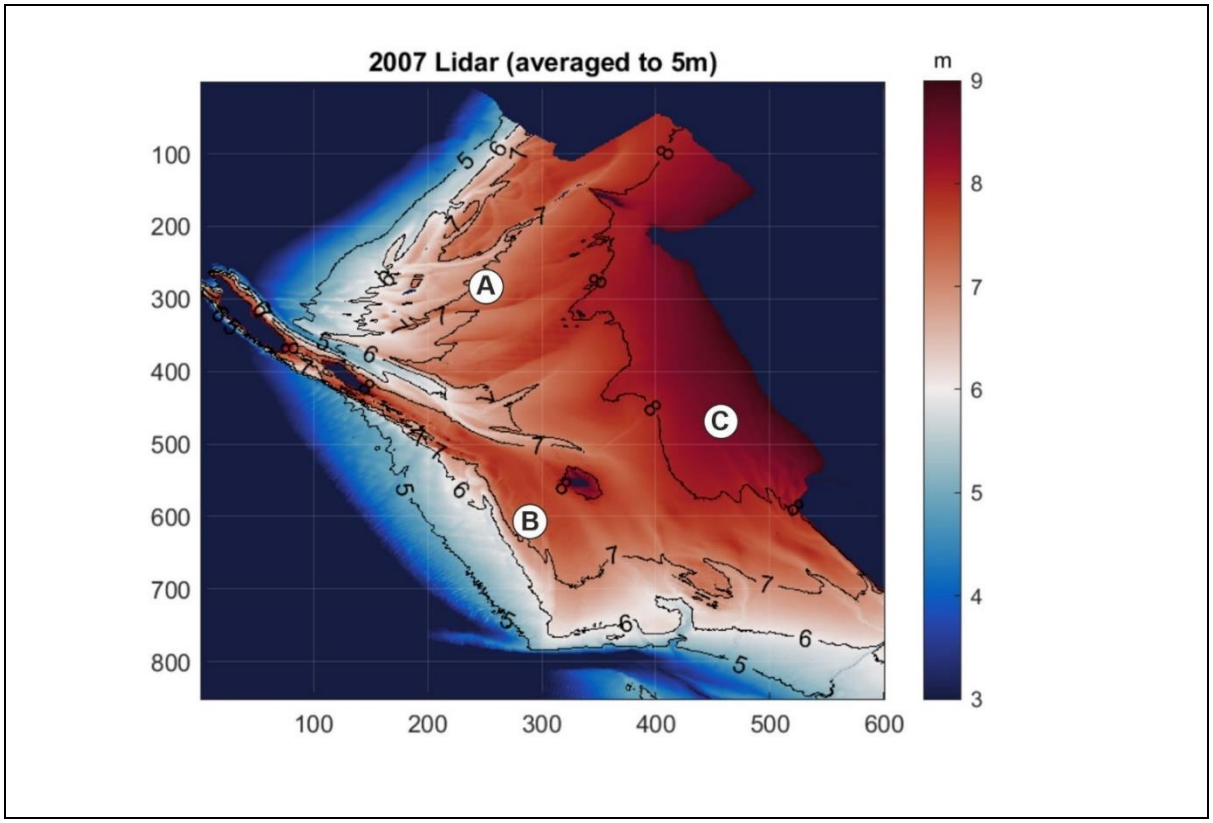

Figure 5.3: Digital Elevation Models derived from 2007 (Oct) LiDAR (Dark blue represents no data, each pixel represents 5m×5m, contours to Admiralty Chart Datum).

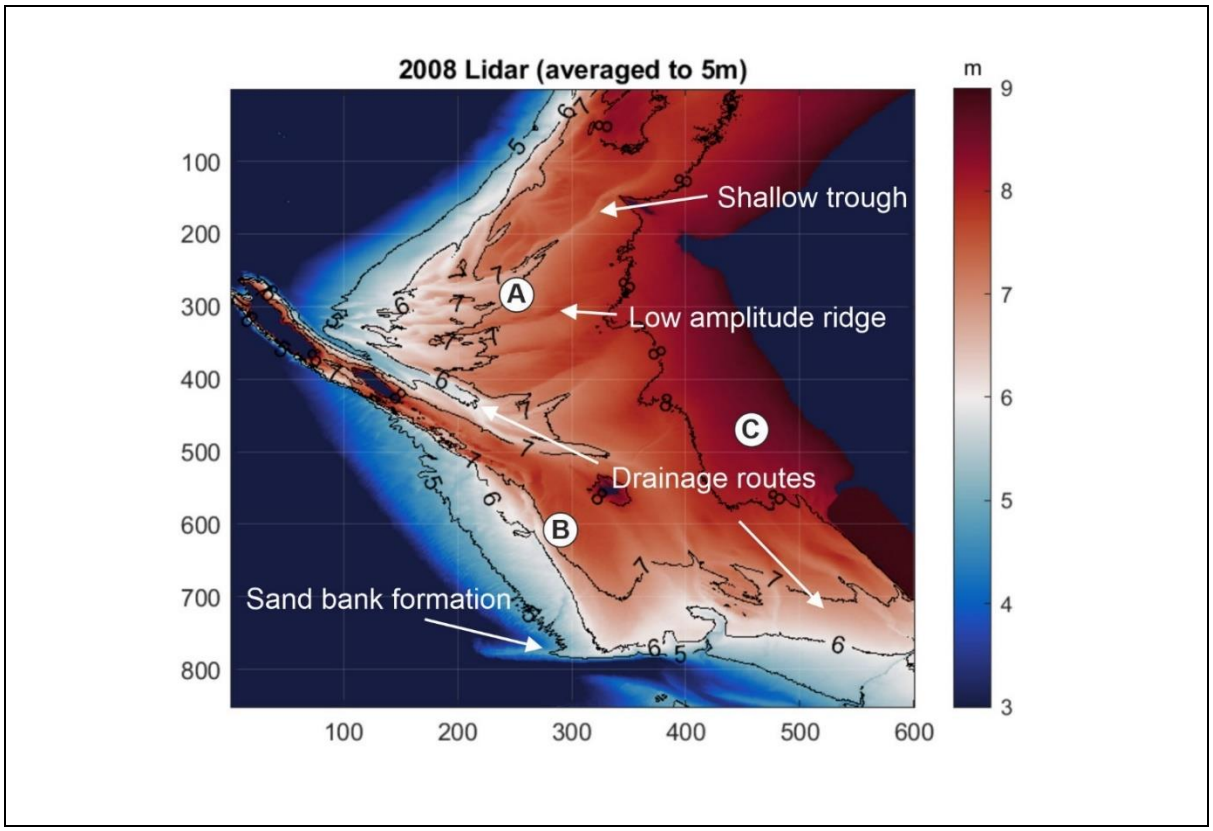

Figure 5.4: Digital Elevation Models derived from 2008 (Oct–Nov) LiDAR (Dark blue represents no data, each pixel represents 5m×5m, contours to Admiralty Chart Datum).

The main features of regions A, B and C described in section 5.3, can be seen quite clearly in each of the three LiDAR survey DEMs (Figures 5.2, 5.3 & 5.4). Detailed fine features can also be seen in each DEM with subtle differences evident between each survey year, for example, low amplitude ridges separated by shallow troughs can be seen in region A. Most of these low amplitude ridges have crest orientations in a northeast direction, with the troughs aligned towards the main drainage channel; the differences between the crests and troughs of these features vary between 0.5–1.0 m

In region B to the south and west of Little Eye there are indications of year-to-year deposition and erosion change. Also, there are channels aligned parallel to the West Kirby marine lake that indicate another direction of drainage to the south east. Region C appears to be relatively stable, with only small changes between each survey; the 8m CD contour (Region C) has a more or less fixed position for the three survey years.

To investigate these subtle changes, the differences have been computed between October 2007 and October 2006, and October/November 2008 and October 2007 respectively (Figures 5.5 and 5.7). These differences have been also been expressed as histograms of the number of differences with the bin size set to a uniform value (0.01 m) in the range of elevation differences (Figures 5.6 and 5.8). Figures 5.5 and 5.7 clearly show sediment movement within regions A and B, and the relative stability of region C. Feature movement towards the southeast, in region A, are represented as bars of erosion and deposition between surveys. In region B, there are erosion and deposition features (with a relatively wide erosion feature) orientated north-south, and an east-west orientated deposition feature region, which appears to be a sand bank.

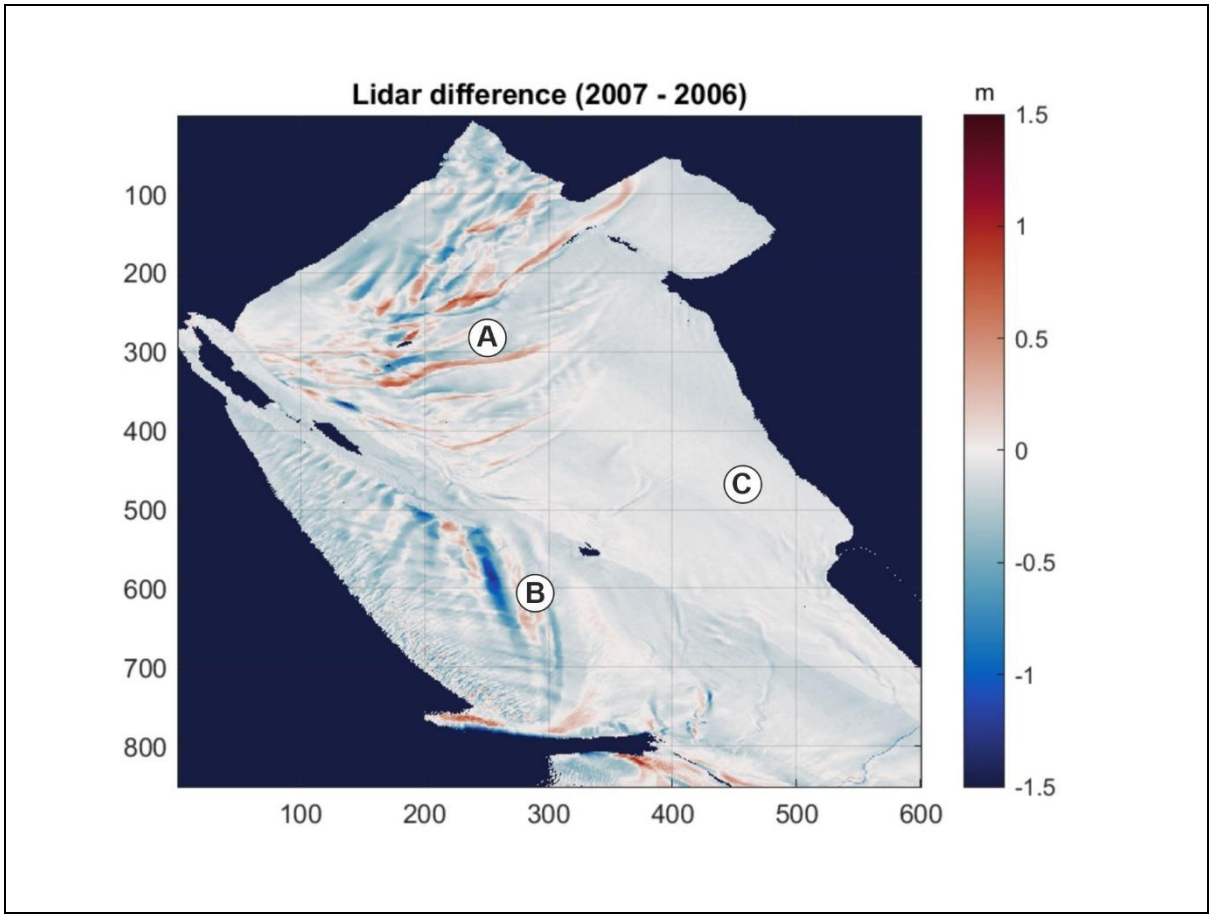

Figure 5.5: Morphological differences between Oct 2007 and Oct 2006 LiDAR surveys (Dark blue represents no data, each pixel represents 5m×5m).

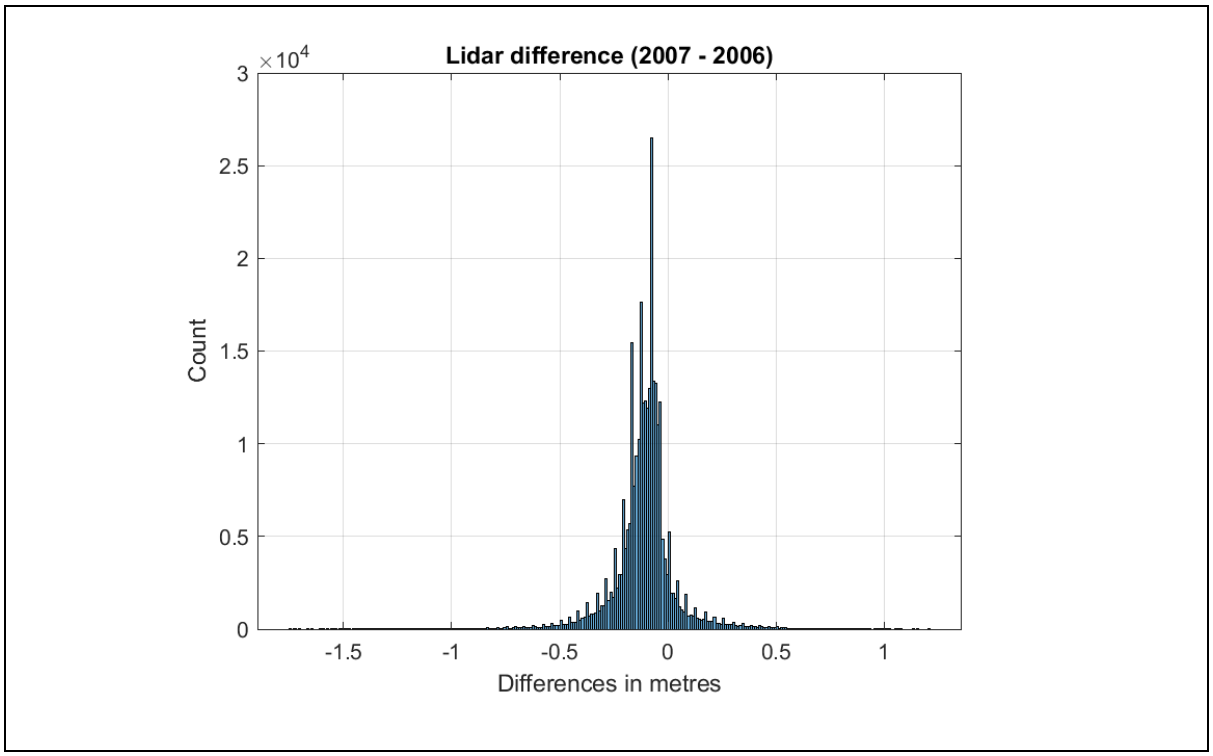

Figure 5.6: Histogram of the morphological differences between Oct 2007 and Oct 2006.

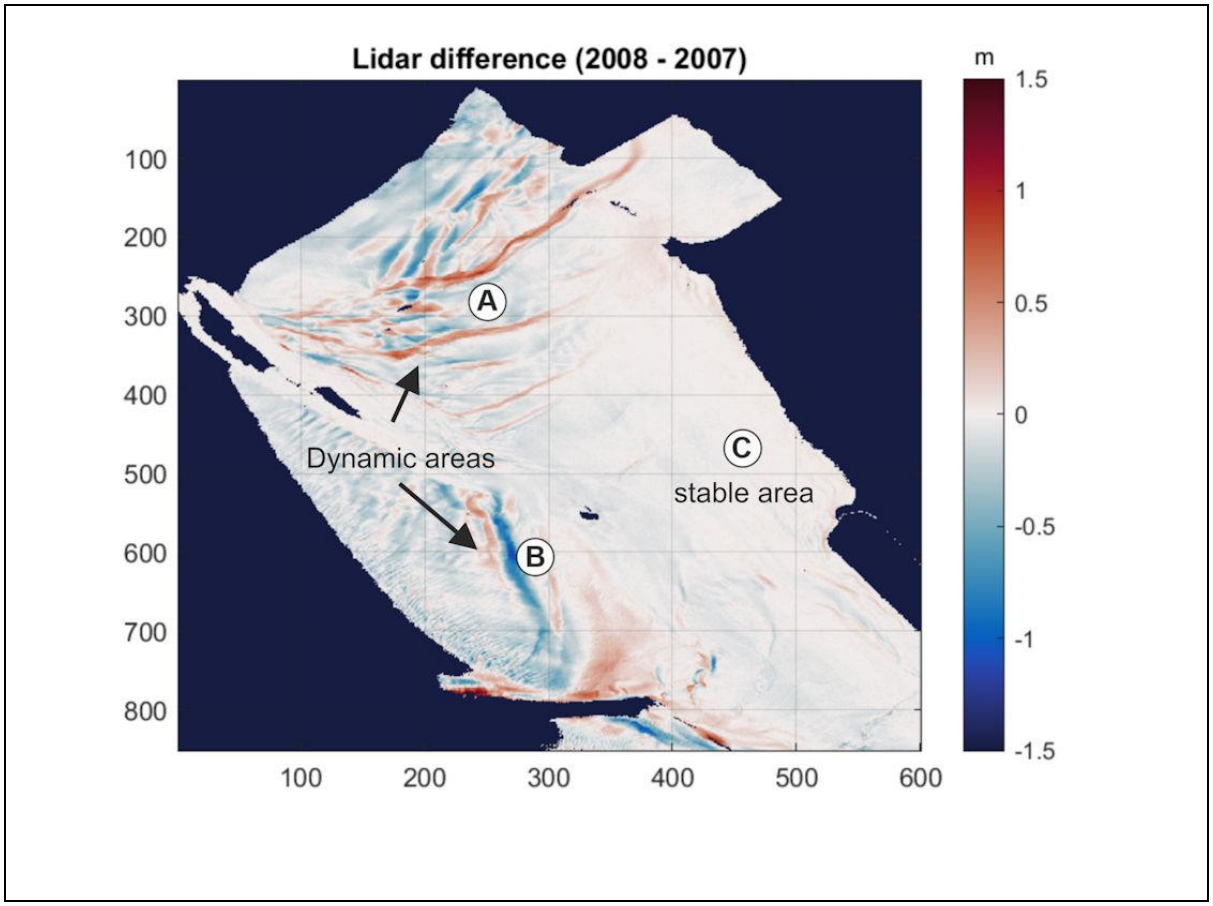

Figure 5.7: Morphological differences between Oct–Nov 2008 and Oct 2007 LiDAR surveys (Dark blue represents no data, each pixel represents 5m×5m).

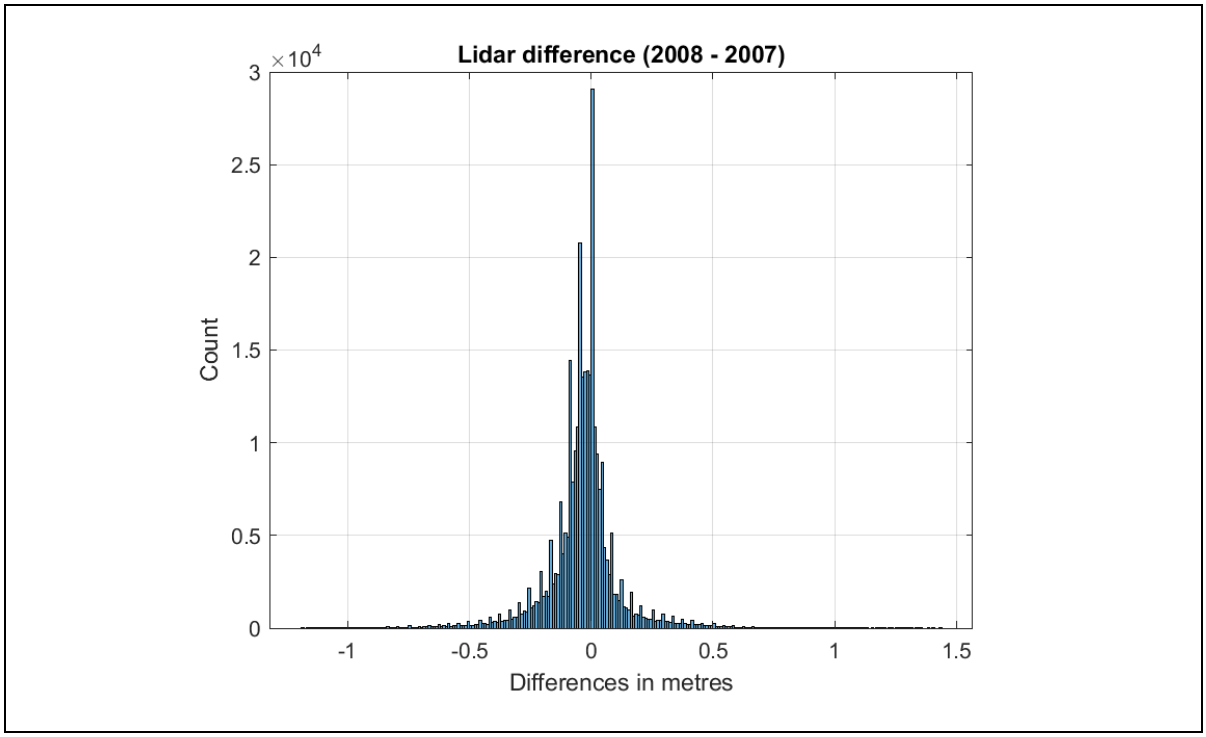

Figure 5.8: Histogram of the morphological differences between Oct–Nov 2008 and Oct 2007.

These maps show evidence of feature migration such as adjacent features of sediment loss and gain, however, the histograms of morphological differences (Figures 5.6 and 5.8) indicate that there is overall loss of sediment between each year, with the majority of counts of sediment differences falling below zero. This is equivalent to a sediment loss of 0.11 m and 0.04 m over the entire area with data (values taken from average height differences over all valid pixel values) between Oct 2007 and Oct 2006, and between Oct–Nov 2008 and Oct 2007 respectively – more sediment was lost during the first year than the second year. Other available LiDAR data (from 2013 and 2017, not shown here) also indicate a negative sediment budget from the 2006 baseline survey.

The differences in LiDAR surveys between 2008, 2007 and 2006 highlight areas of deposition and erosion between each survey. Lines representing the maximum deposition from the LiDAR differences; 2007 and 2006 (black), 2008 and 2007 (red) respectively are shown in Figure 5.9. These lines denote the spatial progression of the low-profile sand ridges towards the shoreline; mainly towards the southeast, and westwards near Little Eye (island). These low-profile sand ridges are generally moving between 25 m and 75 m per year.

Figure 5.9: Lines indicating maximum deposition from LiDAR differences; 2007 and 2006 (black), 2008 and 2007 (red), showing progression of sand features in a shoreward direction.

5.4.2 X-Band radar derived morphological maps

The X-band radar was sited at the top of a tower on Hilbre Island (approximately 25 m above Mean Sea Level) with a clear 360-degree view of the surrounding intertidal areas. It consisted of a Kelvin Hughes marine radar operating at the X-band frequency of 9.4 Hz with complete rotations every 2.4 seconds. It was part of the Liverpool Bay Coastal Observatory project (Howarth et al., 2011) and recorded data between March 2006 and December 2008. These data were processed by (Bell et al., 2016) using the Temporal Waterline method to produce 62 morphological DEMs. Each DEM image was constructed from data over 14-days covering the Spring Neap tidal cycle. Three of these DEMs (Figures 5.10, 5.11 & 5.12) coincided with the 2006, 2007 and 2008 LiDAR surveys; however, note that the LiDAR images are daily snap-shots whereas the radar-derived DEMs are 14-day composites.

Figures 5.10, 5.11 & 5.12 display three of the radar derived DEMs which are the closest temporal match with the LiDAR DEMs shown in Figures 5.2, 5.3 & 5.4. The low amplitude ridges and shallow troughs identified in Figures 5.2, 5.3 & 5.4 can also be seen in these corresponding radar DEMs (Figures 5.10, 5.11 & 5.12). However, there are prominent spatial differences in vertical elevation, evident from comparison with the contour lines on both sets of DEMs. For example, the 8 m CD contour level in the LiDAR data (Figure 5.4) is further inshore than in the corresponding X-band data (Figure 5.12). Also, the radar images appear to have much lower elevations for the some of the shallow trough features shown in region A. Furthermore, region C has variations in elevation not seen in the corresponding LiDAR data (these consist of ‘missing data’ and spatial differences between adjacent cells, which appear as patchy areas in the DEM). There is also a consistent horizontal feature running west to east from Little Eye (island) to the mainland (Figures 5.10, 5.11 & 5.12, more obvious in Figure 5.11), which does not appear in the Lidar data.

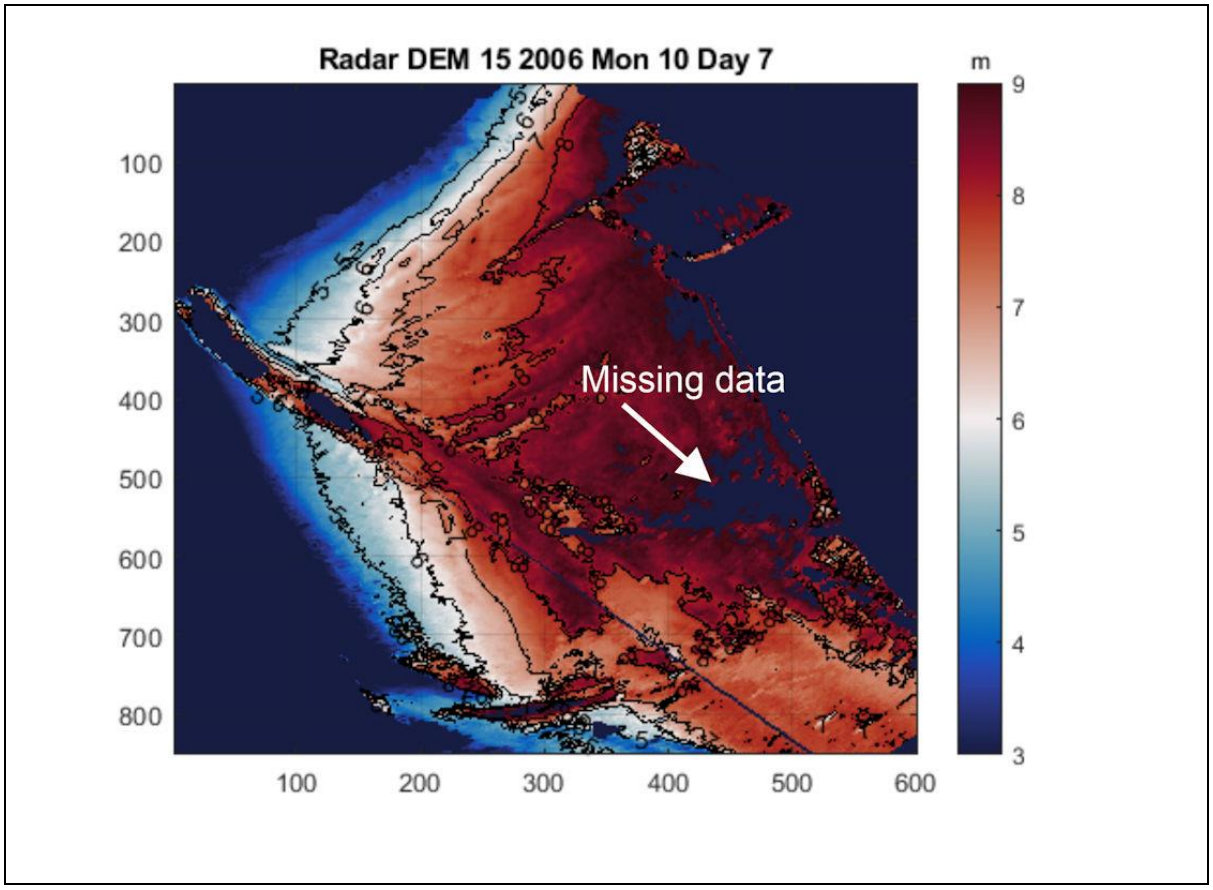

Figure 5.10: Two-week X-band radar composite (radar images until 7 October 2006).

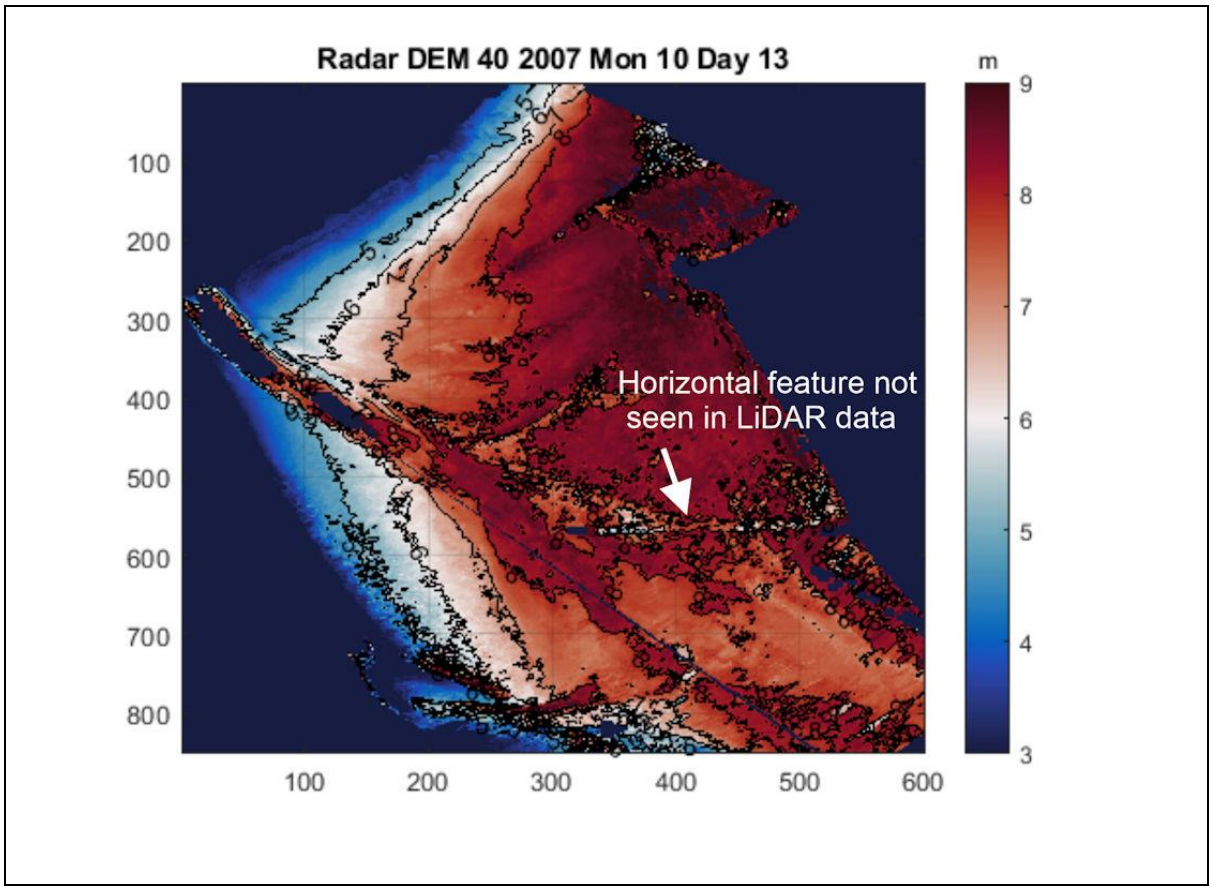

Figure 5.11: Two-week X-band radar composite (radar images until 13 October 2007).

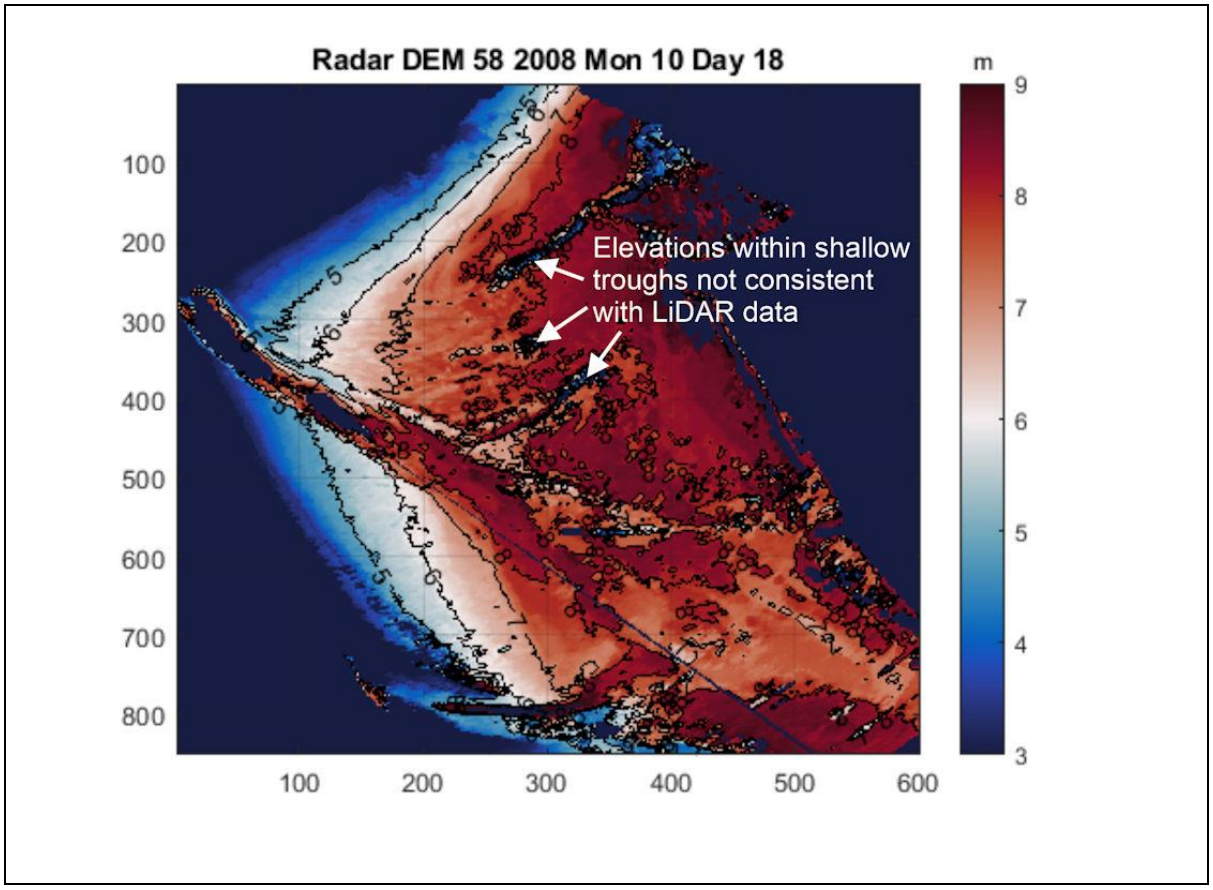

Figure 5.12: Two-week X-band radar composite (radar images until 18 October 2008).

The lower elevations in the trough features are likely caused by the effect of shadowing on the radar signal and this is further emphasised in the differences between the X-band radar DEMs from October 2007–October 2006, and October 2008 and October 2007, respectively (Figures 5.13 and 5.14).

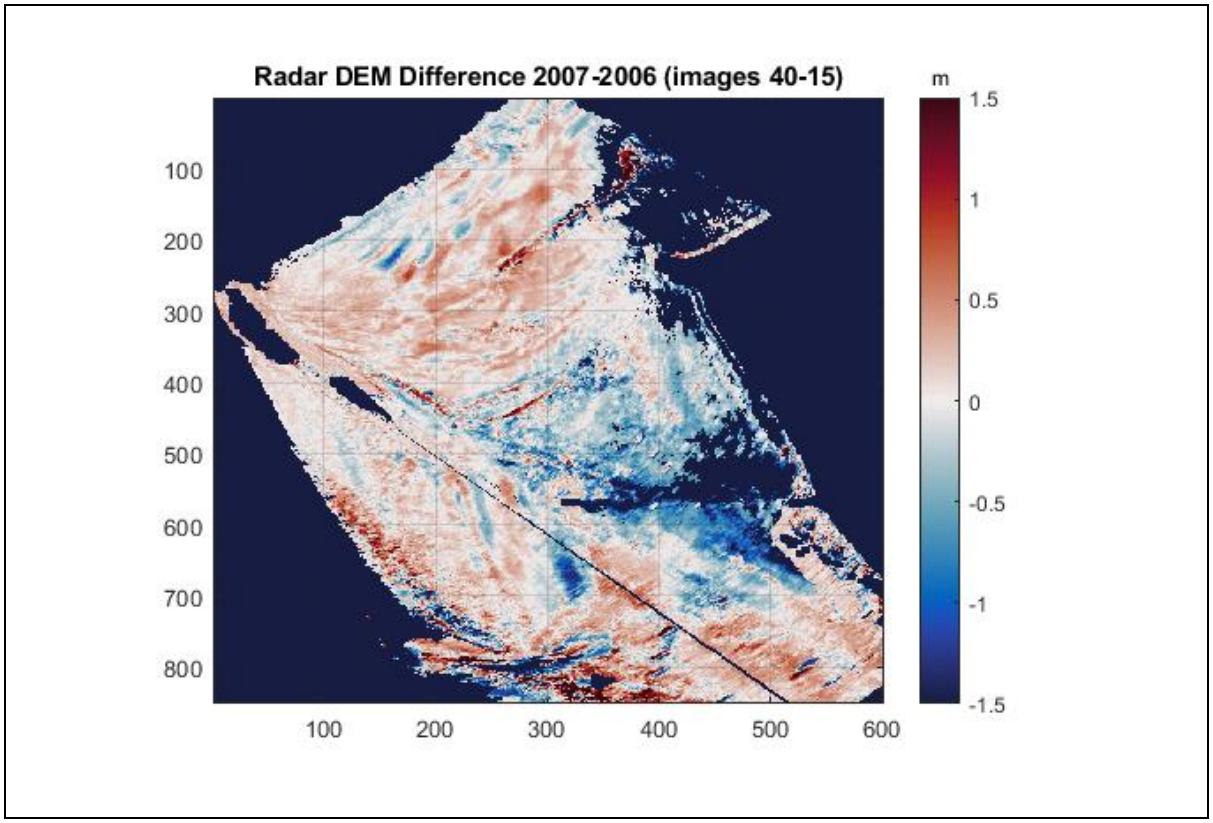

Figure 5.13: Differences between X-Band radar composites between October 2007 and October 2006.

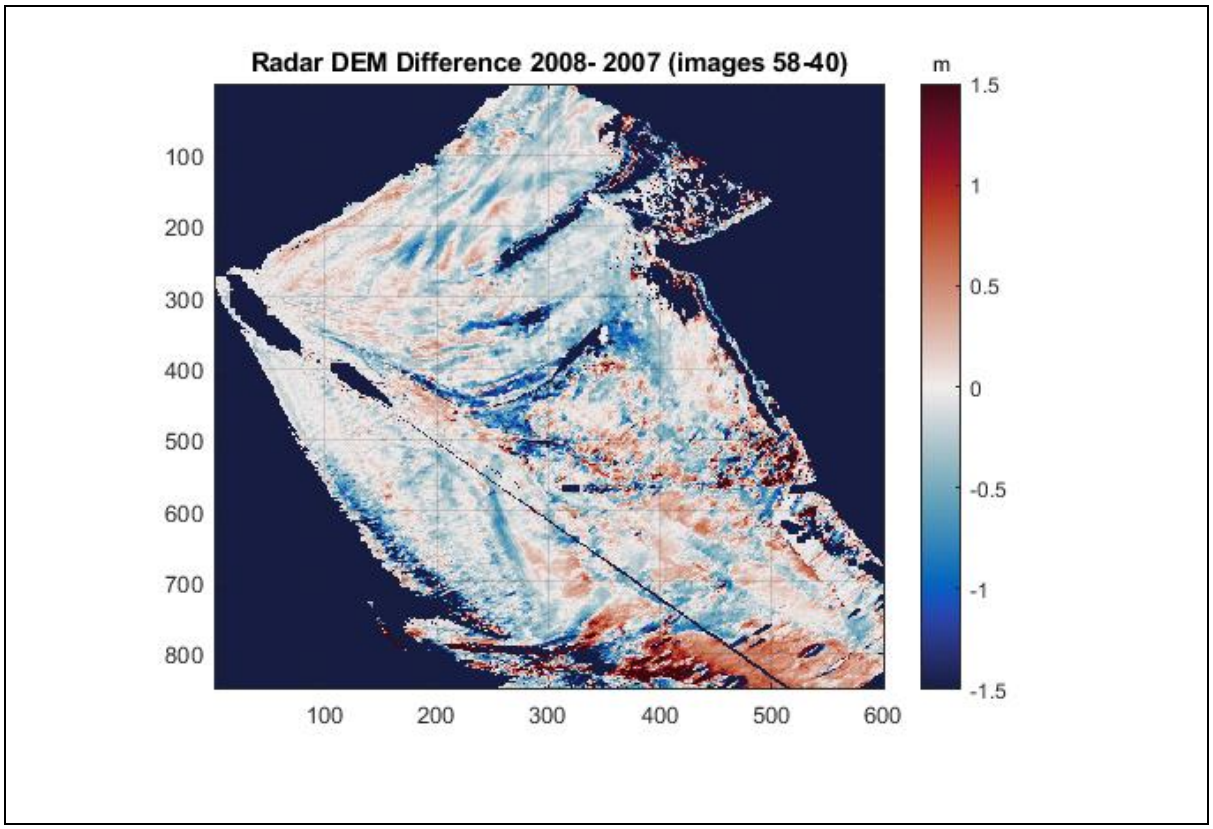

Figure 5.14: Differences between X-Band radar composites between October 2008 and October 2007.

Since comparable LiDAR data were not available for every radar DEM, a statistical analysis of all the X-Band radar DEMs was performed to highlight morphological change over the three-year period, and to help identify spatial errors in the derived vertical elevations. Figures 5.15, 5.16 & 5.17 show the mean elevation, the range and standard deviation for each grid point from the 62 composite X-Band radar images. The mean elevation image (Figure 5.15) shows the large-scale character of the intertidal area, and persistent features which occur across both regions A, B and C. The features identified with the LiDAR DEM data are present, as well as the horizontal feature (east-west, of Little Eye) which only appear in the radar DEM data. The range image (Figure 5.16) identifies areas of likely radar shadowing as well as areas of realistic morphological change, when compared with the annual LiDAR DEMs. Likewise, the standard deviation (Figure 5.17) highlights individual DEM data quality issues; the same areas were identified as areas of low confidence in some of the derived elevations (Bell et al., 2016). The horizontal feature (in Figure 5.16) is likely an artefact of the processing; it is interesting that this coincides with the main routes for walking to Little Eye from the mainland and for authorised four-wheel-drive vehicles to and from Hilbre Island.

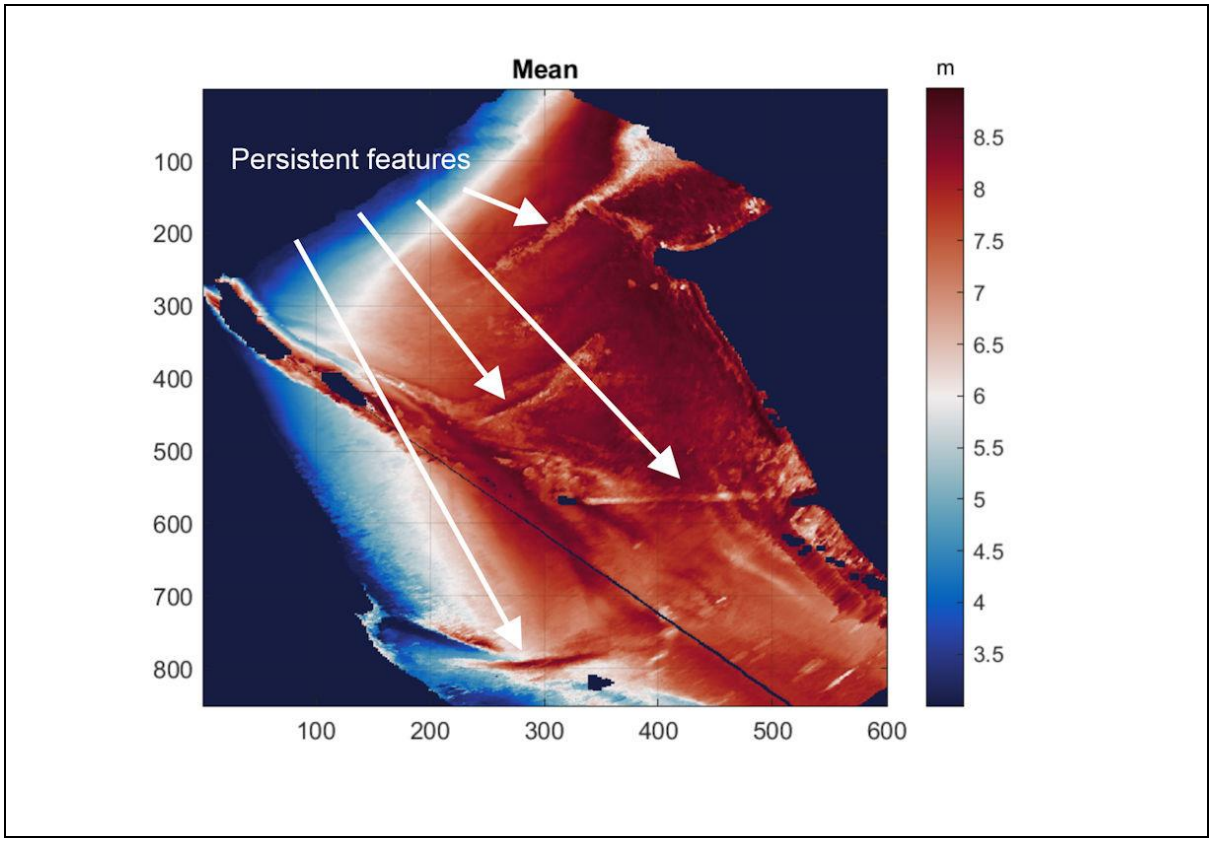

Figure 5.15: The mean of the 62 composite X-Band radar images; mean elevations.

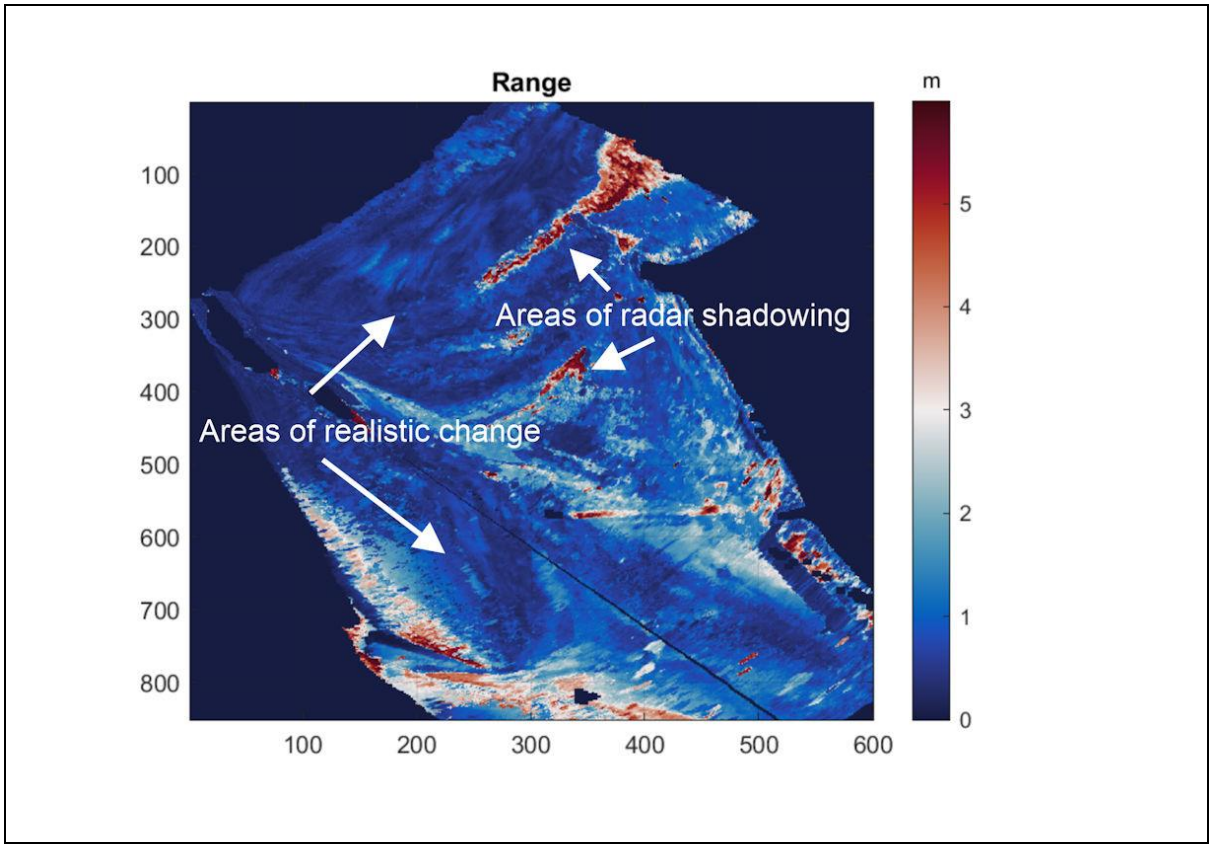

Figure 5.16: The elevation range of the 62 composite X-Band radar images.

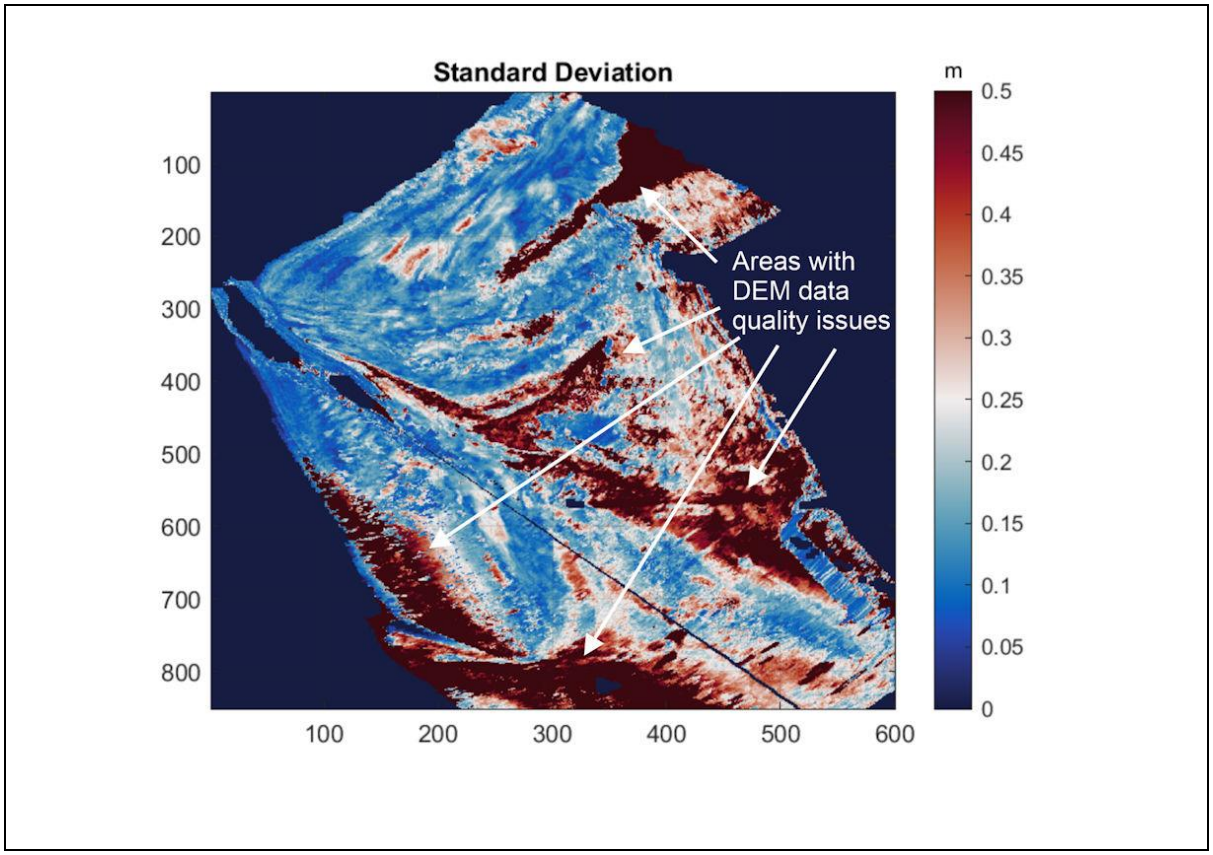

Figure 5.17: The standard deviation of the 62 composite X-Band radar images.

5.4.3 Mask generation

The spatial limitations of the X-band radar data mentioned above require the use of ‘masks’ to exclude potential problem areas in the data, as determined from the ‘range’ and ‘standard deviation’ results. These masks are necessary for subsequent temporal sediment change calculations. Four data masks (Figure 5.18) were created with the QGIS GIS package to first generate outlines which represented good data, i.e., creation of ESRI GIS mapping software shapefiles. These were produced by tracing overlays from the X-band/LiDAR differences (Figures. 5.5 & 5.7 and Figures 5.13 & 5.14) and the X-band radar composite image statistics (Figures 5.15, 5.16 & 5.17) to exclude potential problematic areas in the data. The resulting GIS shapefiles were then converted to ASCII raster masks using the Graphical Abstract Library translator library (GDAL/OGR_contributors, 2022); here, a value of ‘1’ represents ‘good to use’ data and a ‘0’ represents ‘ignore’ data.

Two masks cover the intertidal zone to the northeast side of the Hilbre islands; north site and north site extended: the ‘north site’ mask coincides with the best overall data quality as described from previous analysis (Bird et al., 2017), and the ‘north site extended’ mask includes more of the low amplitude ridge and shallow trough features identified in the X-band and LiDAR DEMs (Figure 5.4).

Another two ‘south site’ and ‘south site extended’ masks were also created. The south site mask covers the area of erosion/deposition to the west of Little Eye (Figure 5.1). The south site extended mask covers a slightly larger area to the south, which contained some poorer data; an animation of the X-Band radar DEMs (not shown here) indicated potential seasonal east-west sand bank formation.

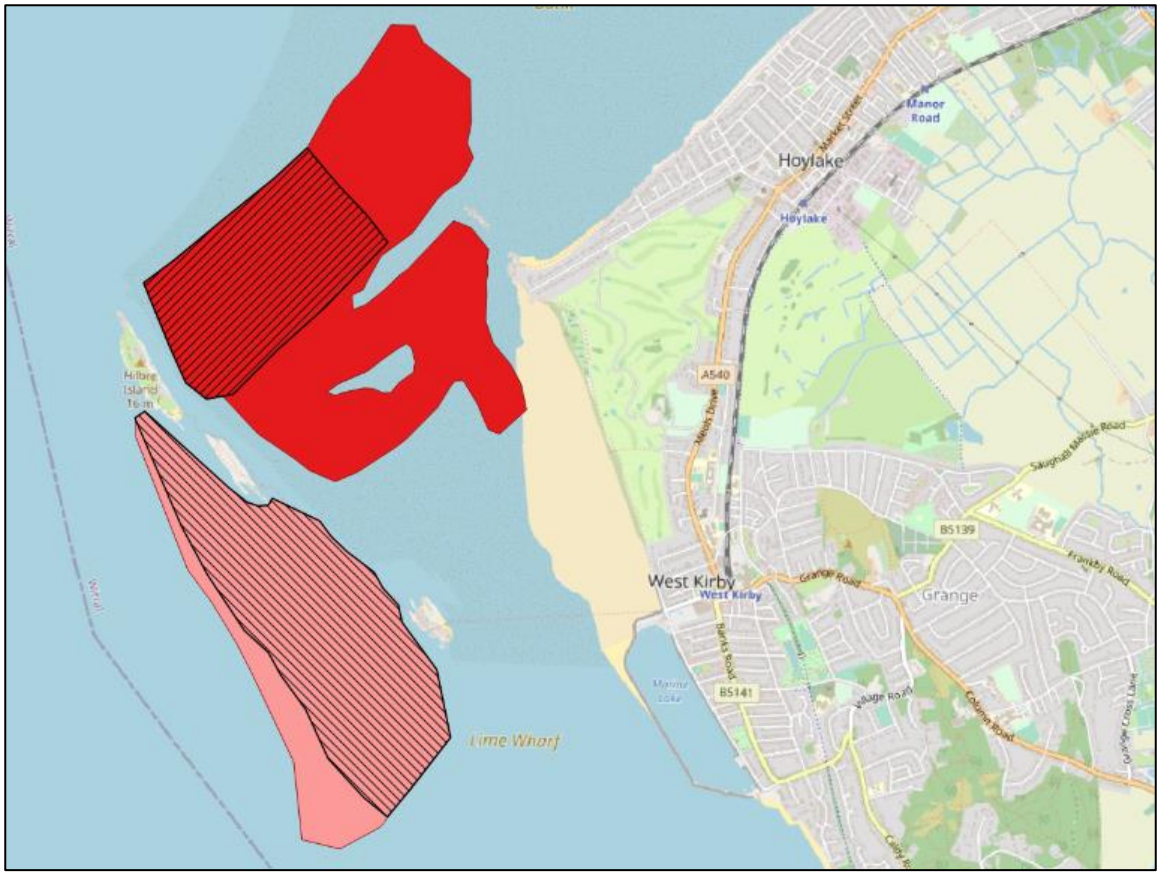

Figure 5.18: Outlines used to create the data masks for north site (black hash lines SW to NE), north site extended (red), south site (black hash lines SE to NW) and south site extended (pink).

5.4.4 Temporal and spatial morphological changes

Applying the masks to the data, estimates of the morphological change over time were calculated between each X-band Radar DEM and the baseline X-band radar DEM. The method is to calculate the average height change in metres for all valid pixels in each of the generated masks. This produced a set of time series of sediment height change in metres for each masked area, for the 'north site', 'north site extended', 'south site' and 'south side extended' (Figure 5.19).

The time series show three cycles of erosion and deposition during the three-year period, with the peak deposition in late spring/early summer 2007 and the peak erosion in mid-winter 2006/2007. At the southern sites the sediment change ranged between 0.40 m per masked area and −0.12 m per masked area, while at the northern sites the sediment change ranged between 0.13 m per masked area and −0.14 m per masked area, i.e., a larger range of annual change at southern sites as compared with northern sites.

The deposition phase begins in spring 2006 and peaks in mid-summer, and then an erosion phase begins until mid-winter 2006/2007. Deposition then returns and peaks at the end of Spring 2007,

followed by erosion until early winter 2007/2008. A small change in deposition occurs up to mid-spring before plateauing until early summer 2008, before the erosion cycle starts again. During this latter period the signals between the northern and southern sites are slightly different, however there is a general increased erosion trend towards the end of 2008. Also, the peaks and low points of average height change (Figure 5.19) are slightly out of phase with each other. For example, the peak change in summer 2006 is seen first in the northern sites, whereas, the peak change in summer 2007 is led by the southern sites. In addition, the peak in 2008 is much flatter than the previous two years.

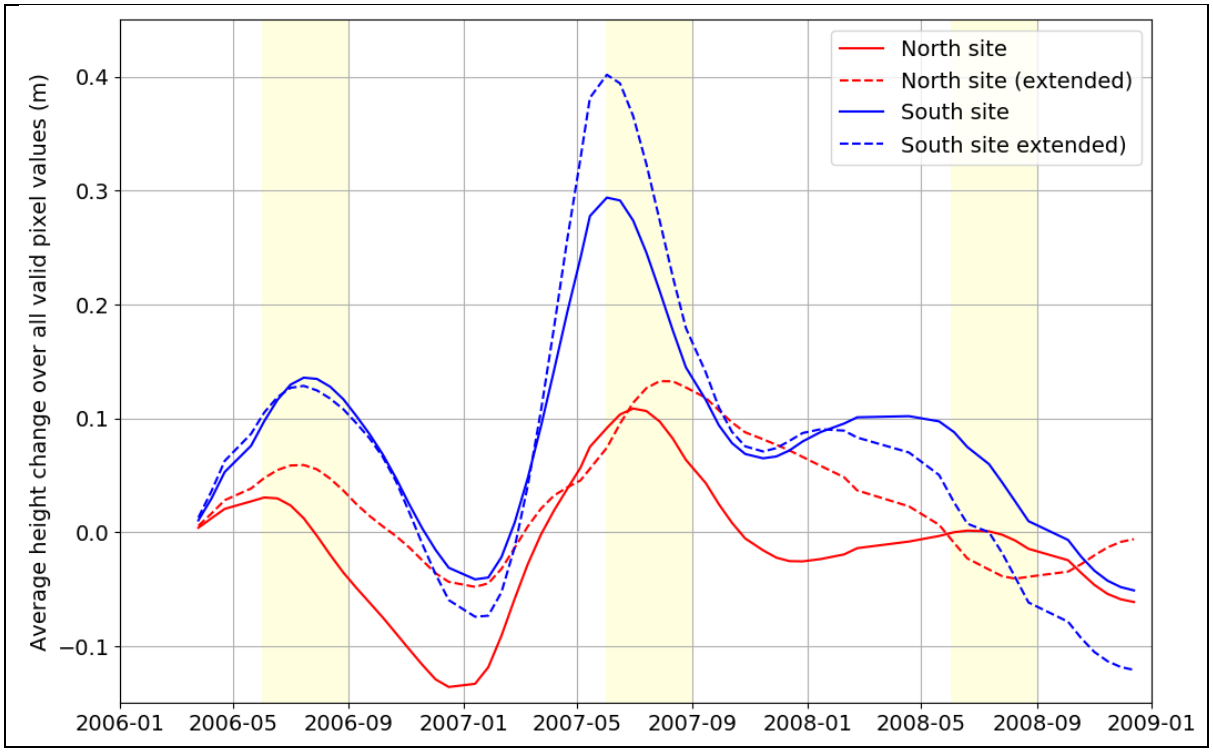

Figure 5.19: Morphological changes expressed as average height change over all valid pixel values. Yellow shading indicates the summer months (June, July and August).

5.4.5 Wave and tidal data

Wave data were obtained from the WaveNet buoy (Cefas, 2019) situated 19 km to the northwest, in Liverpool Bay (Figure 5.1). During the experiment the majority of the large waves were from the west and northwest with significant wave heights less than 5.5m (Figure 5.20).

Tidal data were obtained from the UK Environment Agency (EA) (EA, 2019b) tide gauge at Liverpool Gladstone Lock (WGS: 53° 26′ 58.9″N, 03° 01′ 5.2″W, British National Grid: SJ 3248 9525) which is situated 16 km to the west (Figure 5.1); data were downloaded from British Oceanographic Data Centre (BODC) website www.bodc.ac.uk. A localised tidal record was created

using tidal predictions for Hilbre Island, plus the additional non-tidal element (i.e., storm surge) extracted from the Liverpool tidal observations; this method was also used to derive the X-band radar DEMs (Bell et al., 2016). The highest spring tides of the year occur after the equinoxes in March (about 20th March) and September (about 22nd September). Daily mean significant wave heights and maximum daily tidal heights time series are shown in Figure 5.20. The daily mean significant wave heights are generally larger between September and May, and this also coincides with larger tides.

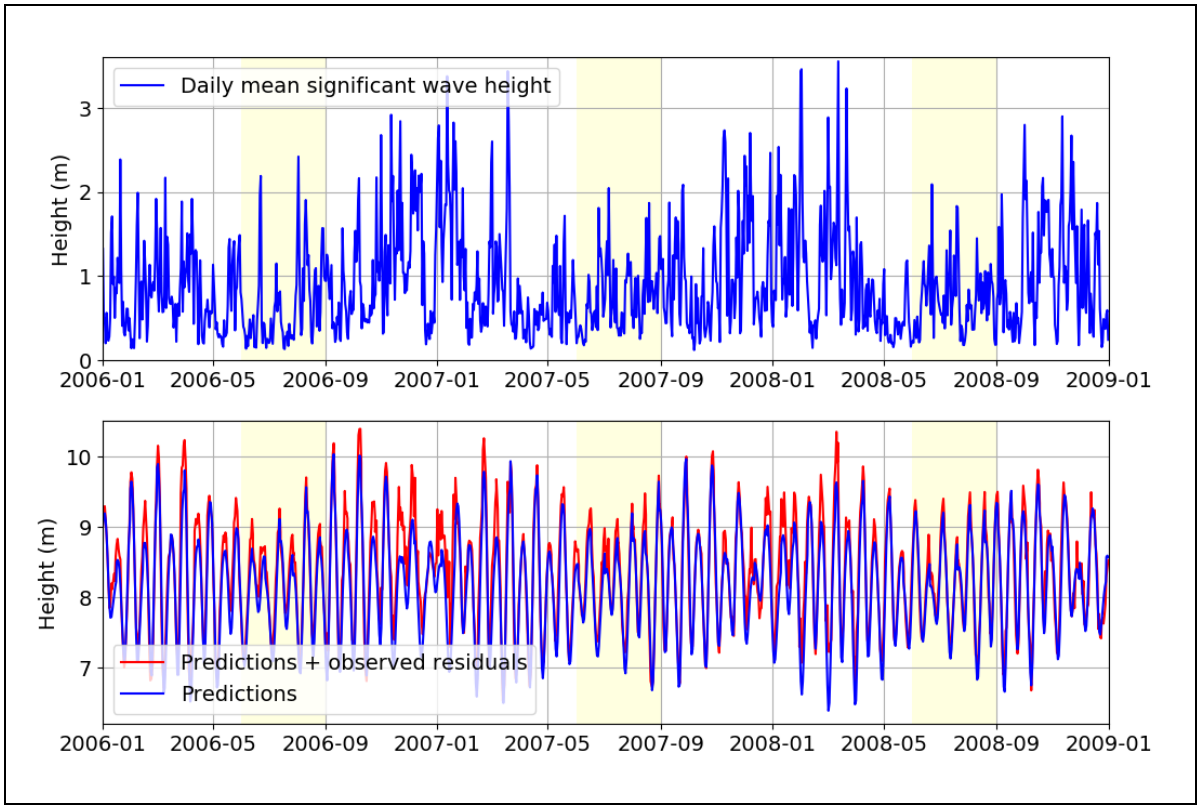

Figure 5.20: Daily mean significant wave height and maximum daily tidal heights. Yellow shading indicates the summer months (June, July and August).

In order to explore the contribution of tidal, surge and waves (Figure 5.20) to the cycles of deposition and erosion (Figure 5.19), a times series of data have been generated of counts of days (over two-week periods) when the daily maximum tidal level was greater than the mean high water neap (MHWN of 7.12m), and the mean significant wave height was greater than 0.9 m and 2.0 m (Figure 5.21). The MHWN threshold of 7.12m was chosen since most tides above this would cover the masked areas, and thus contribute to either erosion or deposition. The wave thresholds were chosen to compare average wave conditions against much larger storm events with significant wave heights greater than 2.0 m. For the 0.9 m cut-off time series, the day counts are now referred to as 'geomorphologically significant days' in terms of likely response to the prevailing hydrodynamics; days where the hydrodynamics are capable of making a change to the coastal geomorphology.

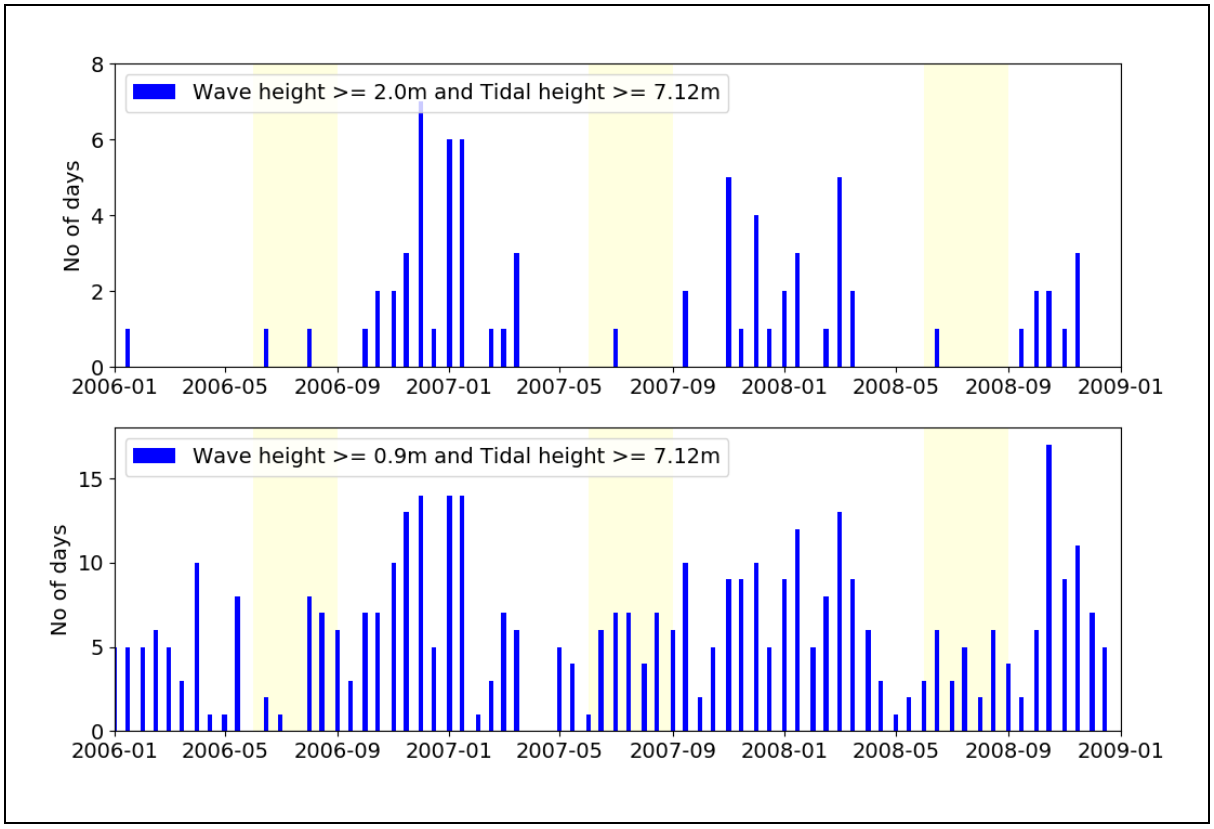

Figure 5.21: Top: Number of days when waves heights ≥ 2.0 m and tidal height greater than the mean high water neap level (7.12 m), **bottom**: Number of days when waves heights ≥ 0.9 m and tidal height greater than the mean high water neap level (7.12 m). Yellow shading indicates the summer months (June, July and August).

There are three depositional and erosion episodes throughout the three-year study, with the first two peaks well defined, whereas the final peak is much flatter. The first deposition cycle (Figure 5.19) starts from early April to late July 2006 and over this time period there were only 13 'geomorphologically significant' days (Figure 5.21) when the mean tidal heights were greater than the mean high water neaps and mean significant wave heights were greater than 0.9m. The first erosion cycle starts from August 2006 to mid-January 2007 with 108 geomorphologically significant days. The second deposition cycle starts from mid-January 2007 to end of May with 27 geomorphologically significant days. The second erosion cycle starts from June 2007 until November/December 2007 with geomorphologically significant 82 days. The third depositional cycle starts from December 2007 until April 2008 (south site), June 2008 (north site) with approximately 67 geomorphological significant days; this deposition is less obvious in the south site extended data and not apparent in the north site extended data. The third erosion cycle starts from the end of April 2008 (south site), end of July 2008 (north site) with approximately 92 geomorphological significant days; All the sites show

the third erosion cycle except for the north-site extended which shows the start of deposition from mid-August onwards.

5.5 Discussion

The annual LiDAR surveys produced good quality spatial data over the intertidal area (Bell et al., 2016; EA, 2019a), and the differences between each year indicate an overall loss of sediment. These data provide a relatively accurate calculation of volumetric change in sedimentation between each year. Between Oct 2007 and Oct 2006 there was an overall loss of 0.11 m over the entire area, while between Oct/Nov 2008 and Oct 2007 there was an overall loss of 0.04 m over the entire area. They also showed the presence of low-amplitude ridges which appear to move shoreward at speeds between 25 m and 75 m per year. North of the island chain, these intertidal bars move towards the southeast, between Hilbre Island and Red Rocks. They mainly appear from mean sea level (MSL) to the mean high water neap (MHWN) level, as observed by using other monitoring techniques e.g., video (Masselink et al., 2001), and to a lesser degree higher up the beach. They appear to require the higher flow velocities at mid-tide to form, and that further towards the shoreline they are obliterated when they reach shallow water, largely due to the influence of breaking waves.

To the south of Hilbre Island, these bedforms also appear to propagate towards the southeast along the edge of the island chain, however they are smaller in size. In addition, directly to the west of Little Eye there is a relatively wide low-amplitude ridge which has an eastward movement of 75 m per year. This southern area is more exposed to the open to the estuary, and is adjacent to the Hilbre Channel. This particular low-amplitude ridge is likely constrained by the increasing beach levels further towards the east. Furthermore, this particular intertidal bar is just to the south of the gap between Little Hilbre and Little Eye; this gap allows the tide to flow and ebb through to the northern part of the beach once the tidal level progresses above 7 m CD. When this occurs, diffracted/refracted waves (Houser et al., 2008; Thomas et al., 2011) can pass between the gaps and interact with waves coming from the northeast. Also, at the start of the ebb tide, the flow would be directed southwards through the gap and would increase erosion in the trough of the intertidal bar.

While these LiDAR data are useful in characterising the morphology of the beach, they do not provide the necessary temporal data with which to determine seasonal deposition and erosion variations. Analysis of the X-band radar produced sixty-two morphological maps, one for nearly every two weeks of the three-year study. The low-amplitude ridges mentioned above can also be seen in X-band radar-derived images, and indicate a progressive movement over time to the positions shown by the LiDAR data. Also, the data shows that there are significant variations in beach volume throughout the year, with cycles of both deposition and erosion. For example, during the three-year period the morphological change ranged between 0.40 m per masked area and −0.14 m per masked area, whereas the LiDAR annual differences are −0.11 m over the entire area and −0.03 m over the entire

area respectively (note, that the LiDAR data are for the whole area including regions A, B and C; Figures 5.2, 5.3 & 5.4 show the extent over which these particular data were calculated, whereas the X-radar derived data are for the masked areas). The temporal X-band radar derived data differences (Figure 5.19) provide evidence of the cyclic changes in morphology and the importance of regular monitoring over reliance on annual surveys.

Beach morphology is predominantly influenced by wave action, with a small but important tidal contribution (Masselink et al., 1993): Beach sediments tend to accumulate shoreward during the summer months (less stormy periods), with the opposite occurring during the winter months (more stormy periods). However, the study area is a tidal flat, and in these environments the tides tend to dominate over other hydrodynamic processes (Gao, 2019), and together with moderate waves, this might explain the temporal pattern of cyclic morphological change observed at the four areas (Figure 5.19).

The first two cycles of deposition occur with a combination of both smaller tides and less geomorphologically significant days (13 and 27 days respectively). In contrast, the first two cycles of erosion coincide with larger tides and more geomorphological significant days (108 and 82 days respectively). Overall, the results appear to be more like those observed by Gao (2019) than by Masselink et al. (1993), with tides being more influential than waves. Towards the end of the experiment the erosion and deposition cycles are less well defined, since two of the sites show a small flat depositional peak followed by erosion, while the other two sites show erosion from January 2008 until the autumn period; larger tides and more geomorphological significant days are present (approximately 67 days during the depositional period, and about 92 days during the erosional period). It is also interesting to note that the sand bank identified in the south site extended (Figure 5.4) follows the first two cycles of deposition and erosion (from observation of animation of X-band radar DEMs), however it starts to develop again in May 2008 and continues until the end of the data in December 2008. During this period the south site extended data indicate the erosional cycle, and thus sediment has moved from this area, while enhancing the sand bank. Again, there is probably a strong influence from tides in the migration of this larger morphological feature.

The larger erosion/deposition range at the southern sites could be a result of a combination of stronger tidal currents together with more exposure to waves. This location is close to the Hilbre Channel, where tidal currents are known to reach 0.75 ms^{-1} (Bolaños et al., 2010) during flood and ebb, and the beach is slightly steeper and lower than the north of the island chain. In contrast, the smaller erosion/depositional range at the northern sites could be due the islands providing protection from waves (Thomas et al., 2011) as well as reduced tidal currents. The phase differences of temporal morphological changes between the peaks between both north and south sites (Figure 5.19) could be due to the position of the intertidal bars within the masked study area i.e. intertidal bars forming and

moving shoreward. Although not included in this research, aeolian sand transport could be an additional factor in affecting the upper tidal flat morphology; it is reported to have an effect on morphological change on tidal flats and beaches if sediments are allowed to dry out between tides (He et al., 2022).

5.6 Recommendations for future X-band radar deployments

Measurements of local sea level within the radar footprint would reduce the vertical errors such as observed in the composite X-band radar DEMs from this experiment. However, the recommendation would be to incorporate a network of tide gauges, distributed in key areas, for future X-band radar installations. For example, low-cost IOT pressure sensors (Knight et al., 2021) combined with other fixed tidal gauges would be able to pick up the different tidal symmetries which occur across complex intertidal areas such as experienced at this location. These spatial sea level data would then feed into the water-line method, and thus improve the overall DEM data quality.

Local wave measurement (Knight et al., 2020) would also aid in the understanding of wave modulation and wave interaction, and thus identify in more detail the role of waves in morphological change. This is especially important where wave refraction occurs. For example, at Hilbre Island, a complex sea state occurs on the northern beach when waves from the northwest meet with waves crossing in between the islands, and identifying when this occurs would provide more insight into the role of waves.

These spatially distributed tidal data would also be useful for incorporating into the waterline methodology to derive DEMs over 1–7 days, rather than 2-week intervals. Previous analysis of intertidal bars shows a tendency for enhanced morphological change during neap tides (Masselink et al., 2006), and thus composite images based on fewer days would provide the necessary data to explore this in more detail. The data reported here are 2-week composites which smooth out any neap/spring morphological variation. Also, the effect of individual storms could be explored in more detail with 1-day composite images.

5.7 Conclusions

Annual LiDAR surveys provided accurate elevation data over the wider intertidal areas around Hilbre Island. Differences between these surveys highlighted the most dynamic areas within the study area. For example, the low-amplitude ridges and troughs to the northeast of Hilbre Island, and the intertidal bars and the wide sand ridge feature to the south of Little Eye (island). These features were present between the tidal mean low water and mean low water neap limits. To the north of the island chain the troughs were orientated southwards towards the main flow route for the ebb tide.

To investigate morphology changes over shorter time scales, two-week composite DEMs were derived from X-band radar, and these were analysed alongside the LiDAR data. Data masks were used to generate 'best data' by removing errors associated with radar shadowing and other effects, and those introduced in the water-line methodology from using regional tidal data.

These two-week masked composite DEMs derived from the X-band radar showed that over the three-year study period there were three cycles of deposition and erosion. These ranged from gains of up 0.4m per masked area, to losses of 0.14 m per masked area. This contrasts with the volume differences calculated from the annual LiDAR surveys, which showed losses of 0.11 m and 0.03 m over the entire area, between Oct 2007 / Oct 2006 and Oct-Nov 2008 / Oct 2007, respectively. The deposition peaks in mid-summer in 2006, early summer in 2007 and between late spring/early summer in 2008. During this latter period the peak was noticeably flatter than the previous peaks and occurred earlier at the southern site than at the northern site.

The erosion/deposition cycles appear to be controlled by the tidal elevation range, including the storm surge, with moderate waves contributing to the process. The depositional cycles occur during times which have smaller tides and less geomorphologically significant days, whereas, the erosional cycles occur during times which have larger tides and more geomorphologically significant days. Single larger storms with waves greater than 2 m (and with tides > 7.12 m) do not appear to be the controlling factor in morphological change, however it is difficult to assess this since the X-band composites DEMs were derived over a 2-week (Spring/Neap) cycle and thus any evidence would be smoothed out.

Future X-band surveys would benefit from additional instrumentation within the intertidal zone. For example, localised tidal information would help to reduce the errors experienced within the water-line methodology and this would improve the spatial accuracy of the resulting derived DEMs. Also, localised tidal and wave data would lead to a better understanding of the causes of morphological change. Overall the X-band radar system has shown that it can provide the necessary temporal data for coastal engineers to manage the intertidal zone, however it needs to be used alongside additional instrumentation e.g. tide gauges, to achieve the best outcomes.

6 Final conclusions and discussion

This research has targeted advances in coastal monitoring; in particular, developing two packages to obtain improved spatial data on tides and waves in support of radar monitoring. The focus of the study has been on supporting data collection where financial resources are limited, and thus the low-cost developments are alternatives and/or supplements to high-end oceanographic instrumentation. The sea-level instrumentation developed as part of this research were created using advances taken from other research sectors and/or from mass-market driven applications. Data from these types of instrument are especially important for improving the data quality from X-band Radar derived DEMs, and to provide the necessary localised data to relate sediment movement to tidal and wave interactions. These devices are also suitable for other monitoring projects where sea-level and wave data would supplement individual research goals and provide additional capacity for existing tidal networks. Also, when deployed as part of a localised IoT network, the redundancy offered by numerous devices can to help maintain data continuity when individual sensors are lost or become faulty.

The data from the GNSS buoy, once processed can be easily converted to a national vertical coordinate system e.g., Ordnance Datum Newlyn, whereas the IoT tide using a pressure sensor has to be leveled to a known vertical datum level. Furthermore, the pressure sensor data has to be corrected using data from an atmospheric pressure sensor and then converted to a water level. In addition, the pressure sensor should also be calibrated before and after each deployment to check for sensor drift. The IoT tide gauge costs less to build than the GNSS buoy with the potential to reduce the costs further by rationalizing the electronics e.g., single pressure sensors cost £4. The GNSS buoy is more suited to locations where there are open skies, whereas in the IoT pressure sensor could be deployed very close to coastal infrastructure e.g., piers, rock groynes or sea defences.

Further development of the GNSS buoy should involve revisiting solar power which would allow for longer deployment periods. This was initially trialed and showed promise with land-based testing, however the solar panels were damaged by a boat during the final field evaluation. Also, it would be worthwhile exploring the use of bungee cord with future mooring configurations to see if it reduces the high accelerations experienced during the intertidal beach experiment at Rossall, Fleetwood. Furthermore, for deployments alongside the X-band Radar, software scripts could be setup, to routinely download the data via Wifi to the X-band Radar shore site, to be then incorporated into the overall morphological processing system. Additional developments might include using dual frequency receivers with better antennas e.g., U-blox ZED-F9P embedded within the Emlid M2 (https://emlid.com/reach/), plus interfacing low power mobile- phone/ radio telemetry to the Linux boards.

While the developed instrumentation came too late to apply to new X-band Radar deployments the research has also refined approaches for determining morphological change from successive intertidal DEMs derived from historical X-band radar deployments. Analysis of a three-year period of two-week composite DEMs, annual LiDAR DEMs, tidal and wave data shows that the morphological changes observed in the DEMs are mainly influenced by tidal range, with a contribution from waves, together with migration of tidal bedforms. The tidal and wave data used for this analysis were taken from nearby locations, however more localised data e.g., from devices developed as part of this research, would have likely improved the overall DEM data quality and thus allowed for a better interpretation of the morphological changes.

6.1 Low-cost GNSS buoy

The first package, the low-cost GPS buoy was successfully developed by first designing and building the buoy platform, and then combining it with a suitable low-cost GNSS system. The overall cost was £300, with the buoy parts costing £100 and the GNSS logger costing £200. The simple and economic design of the buoy platform, using aluminium scaffold poles and trawler net floats to create the platform has a two-fold advantage. It is quick to construct and consists of readily available and low-cost parts. The four-trawler float design provides a low and stable platform to keep the GNSS antenna level to the sea surface. In addition, the strength and stiffness of the design was improved by replacing the standard grub screw fittings with stainless steel nuts and bolts. This design can be easily replicated by other research groups, who might want to incorporate different types of sensor.

The novelty of the research was to take advantage of improvements in low-cost and low-power GNSS chip designs, and the mass market requirement for small GNSS devices. This led to successful experiments using the single frequency U-blox M8T GNSS receiver, within an evaluation kit, and then with the Emlid Reach which was incorporated into the final design. The Holyhead harbour deployment, located in a sheltered location, showed that the GNSS buoy could record sea-level to centimetre accuracy (1.4 cm RMSE) when compared to a research quality tide gauge using the Van de Castelle tide gauge performance test. The results also indicated the presence seiches with periods of 15 and 22 minutes in the sea level data; harbour oscillations caused by coastal geometry and wave-induced disturbance. In some port locations these types of harbour oscillation can cause issues for docking ships safely and thus this would also be an alternative application for the GNSS buoy. Furthermore, higher frequency oscillations were observed, of ten, eight and four second periods, and these were most likely induced by the busy port traffic.

The follow up Rossall (near Fleetwood) deployment, within an intertidal zone, returned good quality data during slack waters and for the following ebb tides. However, discontinuities were observed in the elevation data during the flood tide, coincident with high accelerations and losing satellite lock. These were probably caused by a combination of strong tidal currents with spilling waves which

would put the mooring lines under tension and allow white water to spill over the antenna, thus degrading the vertical solutions. Replacing the connection from the GNSS buoy to the surface float with a rubber bungee (as sometimes used for wave buoys) would allow for more free movement, reduce water spilling over the antenna which would likely lead to improved data quality. The GNSS buoy also returned good quality wave data as compared with a nearby wave buoy with very small differences in significant wave heights (differences between 0.0 and 0.3 m) and wave periods (differences between 0.1 and 0.2 seconds). In addition, it was demonstrated that daily raw GNSS data can be downloaded remotely using the embedded WiFi connection (if within a 500 m radius) to a shore-based computer with a suitable external antenna. Future developments could include automation of this process from a shore-based system; power and telemetry could be provided by an X-band radar installation.

The USB battery packs used provided enough power for at least four days, however for extended operations a solar panel solution would be a requirement. Although only briefly mentioned, a solar power version was designed and this was trialled within Holyhead Harbour. However, a yacht moored too close to the deployment and over a few tidal cycles managed to damage the solar panels by crossing over the top of the buoy. Unfortunately, due to time constraints and the availability of boat support a repeated experiment was not possible. Future work could involve incorporating the panels into the design to protect the antenna as well as providing resilience against similar collisions.

While the GNSS buoy developed here was based upon a single frequency receiver, the market has developed rapidly over the last three years and dual frequency devices are now becoming available at the same price point. For example, the Emlid Reach M2 is now available with a U-blox ZED-F9P dual frequency receiver; the supplied helical antenna is also taller than the Tallysman patch antenna and would be less prone to being immersed by spilling water. Further recommendations would be to evaluate these low-cost dual frequency GNSS receivers to determine if they would be an overall improvement on the existing set up.

6.2 Low-cost pressure sensor

The second package, the IoT tide gauge was based upon an Arduino Sigfox MKR 1200 microcontroller and a Measurement Specialities I^2C pressure sensor. Two different configurations were successfully developed and highlight the versatility of this package, in that it can be quickly adapted by minor changes to the hardware and software for specific purposes. These off-the shelf components are relatively cheap with the Arduino microcontroller costing £40 (including a SigFox subscription for two years), and the water proofed version of the pressure sensor from Blue Robotics costing £70. These electronic costs could be substantially be reduced (estimated ~£15) by constructing a dedicated unit as part of an electronics project e.g., the individual pressure sensors cost £4. Then, the recommendation would be to subcontract the build to a small dedicated electronics

supplier as a way of economically scaling up production. All the pressure sensors were bench tested by varying the water levels in a 4m tube, and this produced consistent results with measurements within 1cm. While other researcher groups have reported good long-term reliability for this type of pressures with no significant drifting in calibration, the recommendation would be to check the calibrations before and after deployments.

Configuration 1, with the sensor at the end of a long cable and the antenna (plus electronics) in "air" for the deployment period provided excellent results and would be suitable for locations with some form of infrastructure for attachment e.g., channel marker post. This configuration was equipped with the capability to attach solar panels and this would be the preferred power option for long term deployments. Along the Liverpool waterfront it compared well with the nearest tide gauge (RMSE 3.5 cm) which was located 2.4 km upstream. Near-real time data were also successfully returned via the wide area network (SigFox) every 15-minutes and this demonstrated the capability of the IoT concept; in this context, to provide timely data for researchers and coastal managers, and as a way to quickly identify emerging issues with data quality.

During the Crosby intertidal deployment with configuration 2, and with a co-located pressure sensor on an AWAC, the comparisons were not as good (RMSE 4.0 cm) with larger offsets towards low water. Further experiments could investigate this offset as it may have occurred due to bubbles being trapped on the pressure sensor membrane during the drying out process at low water. Aligning the sensor in the horizontal plane, instead of the vertical position, might reduce this possibility by allowing bubbles to dissipate (During the Liverpool waterfront test the pressure sensor was aligned in the horizontal plane).

Configuration 2 consisted of a single waterproof case which consisted of all the electronics, batteries, antenna and pressure sensor. The software was set up in a similar way to configuration 1, to wake up every 15 minutes, record for 40 seconds, send the sea level data via SigFox and then go into sleep mode. However, it was also adapted to record data at 10 Hz to an internal SD card attached to the microcontroller, and to record maximum, minimum and average values over each 40 second period. Post-processing of the 10 Hz data demonstrated the capability to capture higher frequency water level variability due to waves. Further analysis would be required to calculate the pressure attenuation factor, which is necessary to determine actual wave heights (this type of analysis would be beyond the processing capability of the microcontroller, and so it would always be a post recovery process). However, the software could be easily adapted to send these pressure sensor statistics in delayed mode time, as the differences between maximum and minimum pressures, to provide a pseudo approximation to the wave height. Another option which could have been tested at the Crosby channel marker would have been to add the sensor cabling with the electronics in 'air' (as with Configuration 1) as this would have allowed for near-real time communications instead of waiting for the tide to

recede. However, Configuration 2 demonstrated that deployments came be made on intertidal zones without significant infrastructure as it can be anchored down or attached to a small bottom frame.

6.3 IoT pressure sensor networks

The IoT devices developed as part of this research show that low-cost pressure sensors are robust and capable of accurately measuring sea levels and detecting the presence of waves, and these data can be successfully transmitted in near-real time over wide area networks. Appendix 8.2 describes how these near-real-time data are treated once successfully transferred to the cloud-based internet servers i.e., data delivery. These data were also made available to other user groups for download and/or to view graphically to test the IoT concept. These devices would improve the spatial data on tides and waves in support of radar monitoring. The low cost of implementation also allows the possibility of creating a network of devices to provide additional data, to increase resilience and to identify significant spatial differences. Investigation into the historical Hilbre Island X-band radar derived DEMs has highlighted the requirement for such devices, since the analysis of the morphological changes and the DEM data quality were affected by using storm surge data from Liverpool and tidal predictions instead of a localised tide gauge data. In hindsight, IoT tide gauges could have been installed at various positions to the north and south of the island chain to identify spatial differences in tidal levels. This would then provide options to target the radar processing to specific areas (using localised tidal data) instead of applying a single tidal record to the whole radar footprint.

A network of IoT tide gauges would also be very useful for areas where tidal amplitudes and phases can vary significantly over short distances. For example, in the Mersey Estuary there are four tide gauges, one situated at the channel entrance on a wind turbine and the other three located at Gladstone Lock, Alfred lock and Eastham lock respectively. These are run by the Mersey Dock and Harbour Company as part of Peel Holdings, and are used to help ships navigate from Liverpool Bay into the Mersey estuary and into the Liverpool and Birkenhead dock complex and the Manchester ship canal. The entrance channel is regularly dredged to keep the channel to 10 m (below Low Water) to accommodate larger container vessels, so the tidal observations are vitally important for timing ship approaches into the deeper inner parts of the River Mersey. There are a number of channel marker posts alongside the entrance channel and these could be instrumented with some of the IoT tides gauges developed as part of this research. Also, due to their simplicity these devices are ideal for smaller ports and harbours which do not presently have tide gauges and rely on tidal predictions for managing port traffic.

6.4 Improved detection of change from successive intertidal surveys

The emphasis within the research was to develop techniques to analyse successive X-band radar intertidal surveys and annual LiDAR data. This was done by using historical data from a three-year X-band Radar study for Hilbre Island, but the methods could also be applied to future surveys. As

mentioned previously, the overall DEM data quality was poor (from the X-band radar) and localised sea level observations would have likely improved them. However, using data masks has allowed extraction of the 'best' data by removing data e.g., caused by radar shadowing, from the subsequent calculations of morphological change. With the latest X-band radar surveys spatial confidence levels are routinely recorded for each derived DEM. These data quality indicators will make the data mask method much easier to implement for future studies (unfortunately these data were not stored for this historical data set).

Both the annual LiDAR data the derived X-band composite images indicate the presence of ridge and trough features from the mean sea level to mean high water mark, and these appear to progress shoreward over time (25 m to 75 m per year). Over the larger spatial area, the LiDAR data tend to indicate an over loss of sediment between subsequent years with more sediment lost between 2007 and 2006, than between 2008 and 2007. In contrast, the masked X-band derived data show a series of cyclic depositional and erosional events throughout the three-year period (both loses and gains) and emphasise the importance of regular surveys. Analysis of the X-band radar derived DEMS with the nearest wave and tidal data suggest that the tidal range is the dominating factor, however the morphological cycles of change appear to be an interaction between tidal height and wave height i.e., change dominated by the tides and geomorphological significant days.

The derived X-band Radar DEMs were generated as 2-week composite images to cover a spring-neap cycle, however it would be worthwhile producing 1-day, 1-week, and composite DEMs covering neap and spring tides separately; the sensors developed as part of this research would improve the accuracy of the X-band derived DEMs and provide localised sea-level, and thus facilitate the generation of acceptable shorter period composite DEMs. This would be useful for future surveys since the role of individual storms or groups of storms could be investigated. Furthermore, previous researchers (Masselink et al., 2006) have suggested there is a tendency for morphological change during neap tides and this could also be tested.

6.5 Planning for future X-band radar deployments

Taking account of the analysis of the historical Hilbre Island data it seems appropriate to identify key locations where the devices developed as part of this research would both improve the accuracy of the radar derived DEMs and also provide enough local information on tides and waves with which to relate to the observed morphological changes. In the first instance and as a minimum requirement, an IoT tide gauge should be located on Hilbre Island at the site of the old tide gauge. This could take the form of Configuration 1 (cabled pressure sensor) and would be relatively easily to deploy to the existing infrastructure. This would provide local tidal observations within the radar footprint, including the storm surge element, which is lacking from the historical data. It would also be worth installing a similar device to the north of the island chain, perhaps to the north of Little Hilbre, to

explore whether there are asymmetrical tidal differences between the flood and ebb tides, north and south of the island chain. Since these devices are quick and easy to deploy and the data the readily available, it could even be part of a pre-survey plan to determine the most appropriate position for the tide gauges. Another IoT tide gauge, with Configuration 2 (self-contained pressure sensor, with internal high frequency recording to SD card), could be installed just south of Red Rocks, to be within one the areas with the ridge and trough features and another to identify wave interactions between the Little Hilbre and Little Eye. This would need to be secured by mounting it in a bottom frame and fixing it to the sand with screw anchors. There are a couple of navigation markers close to the West Kirby marine lake where it could also be attached.

Two positions for the low-cost GNSS buoy have been identified, one in the Hilbre Channel and another just to the north-east of Hilbre Island at the low water mark. The deployment within the Hilbre Channel would have to be carried out using a small boat, however the buoy design allows for this and all that would be required would be a suitable mooring with a large enough anchor to keep it on position. The beach deployment at the low water mark would need to secured with a screw anchor. These locations would provide a more realistic measurement of waves within the radar footprint, and due to the proximity to Hilbre Island there is an opportunity to download the data on a regular basis via an internet connection.

Another option would be to relocate the X-band Radar to the mainland e.g., close to Red Rocks, and reduce the overall radar footprint to just cover the northern part of the intertidal zone. This has a two-fold advantage in that a higher resolution (2-4 m instead of 5 m) could be achieved and the radar signals would be facing the ebb and flood tides which might provide more definitive return signals for the waterline methodology.

6.6 Final reflections

This research has focused on the development of cost-effective sea level measuring technologies for the coastal zone, and in particular for use with X-band Radar monitoring programmes. Sea-level measurements are not only vital for improved accuracy of derived X-band radar DEMs, but are also necessary along with wave data to begin to understand the causes of the observed morphological change on tidal flats and beaches. These devices have been tested in sheltered and exposed coastal locations and are capable of centimetre accuracy measurement of sea level and for capturing wave information (The GNSS buoy is capable of centimetre accuracy for wave heights, whereas the pressure sensor, operating in near-real time mode with the Arduino microcontroller can only provide an approximation of wave height). They have been successfully built out of readily available low-cost parts and can be easily replicated and scaled up to provide measurements to compliment coastal monitoring programmes.

Annual LiDAR data, and three of historical DEM data derived from a X-band radar deployment on Hilbre Island have shown the presence of small sand ridges situated between the mean-sea-level and mean-low-water-springs and these appear to move shoreward over time (25 m to 75 m per year). Analysis from the masked DEMs indicate cyclic changes in the sediment volume (year to year losses between annual LiDAR surveys, contrasting with losses and gains as recorded by the X-band derived 2-week composite DEMs). These morphological changes appear to be influenced by tidal range, with a contribution from waves, together with migration of tidal bedforms. However, the limited tidal and wave data available for this analysis highlights the requirement for comprehensive and localised measurements of sea-level and waves for future X-band radar surveys

The overall low cost of these devices (~£300 for the GNSS buoy and less than £100 for the IoT tide gauge) allows them to be easily incorporated into larger networks and to fill in the gaps in knowledge along coast lines and estuary environments Also, IoT technology coupled with Arduino microcontrollers provides opportunities for incorporation of different types of environmental sensor to enhance coastal monitoring. These low-cost devices could provide coastal managers timely data to respond to extreme storm events and to warn local populations of possible flooding, and would especially useful in areas of the world where resources for hydrodynamic monitoring are limited.

7 Bibliography

André, G., Míguez, B. M., Ballu, V., Testut, L., & Wöppelmann, G. (2013). Measuring sea level with GPS-equipped buoys: a multi-instruments experiment at Aix Island. *The International Hydrographic Review*.

Andrews, E., & Peach, L. (2019). *An evaluation of current and emerging in-situ ocean wave monitoring technology.* Paper presented at the Australasian Coasts and Ports 2019 Conference: Future directions from 40 [degrees] S and beyond, Hobart, 10-13 September 2019.

Apel, H., Hung, N., Thoss, H., & Schöne, T. (2012). GPS buoys for stage monitoring of large rivers. *Journal of Hydrology, 412*, 182-192.

Archived model surge outputs. (2021). Retrieved from https://www.ntslf.org/storm-surges

Ballu, V., Bouin, M.-N., Calmant, S., Folcher, E., Bore, J.-M., Ammann, J., . . . Pelletier, B. (2010). Absolute seafloor vertical positioning using combined pressure gauge and kinematic GPS data. *Journal of Geodesy, 84*(1), 65-77.

Beddows, P. A., & Mallon, E. K. (2018). Cave pearl data logger: A flexible Arduino-based logging platform for long-Term monitoring in harsh environments. *Sensors, 18*(2), 530. doi:10.3390/s18020530

Bell, P. S. (1999). Shallow water bathymetry derived from an analysis of X-band marine radar images of waves. *Coastal Engineering, 37*(3-4), 513-527.

Bell, P. S. (2008). Mapping shallow water coastal areas using a standard marine X-Band radar.

Bell, P. S., Bird, C. O., & Plater, A. J. (2016). A temporal waterline approach to mapping intertidal areas using X-band marine radar. *Coastal Engineering, 107*, 84-101. doi:10.1016/j.coastaleng.2015.09.009

Biausque, M., Grottoli, E., Jackson, D., & Cooper, J. (2020). Multiple intertidal bars on beaches: A review. *Earth-Science Reviews, 210*, 103358.

Bird, C. O., Bell, P. S., & Plater, A. J. (2017). Application of marine radar to monitoring seasonal and event-based changes in intertidal morphology. *Geomorphology, 285*, 1-15.

Blue Robotics Bar02 Ultra High Resolution 10m Depth/Pressure Sensor. (2020). Retrieved from https://bluerobotics.com/store/sensors-sonars-cameras/sensors/bar02-sensor-r1-rp/

Bolaños, R., & Souza, A. (2010). Measuring hydrodynamics and sediment transport processes in the Dee Estuary. *Earth Syst. Sci. Data, 2*(1), 157-165. doi:10.5194/essd-2-157-2010

Brand, E., Chen, M., & Montreuil, A.-L. (2020). Optimizing measurements of sediment transport in the intertidal zone. *Earth-Science Reviews, 200*, 103029.

Bresnahan, P. J., Wirth, T., Martz, T., Shipley, K., Rowley, V., Anderson, C., & Grimm, T. (2020). Equipping smart coasts with marine water quality IoT sensors. *Results in Engineering, 5*, 100087. doi:10.1016/j.rineng.2019.100087

Brown, A. C., & Paasch, R. K. (2021). The Accelerations of a Wave Measurement Buoy Impacted by Breaking Waves in the Surf Zone. *Journal of Marine Science and Engineering, 9*(2), 214.

Brunner, F. K., & Welsch, W. M. (1993). Effect of the troposphere on GPS measurements. *GPs World, 4*(1), 42.

CDDIS. (2018). CDDIS, NASA's Archive of Space Geodesy Data. . Retrieved from https://cddis.nasa.gov/Data_and_Derived_Products/GNSS/orbit_products.html

CDDIS, NASA's Archive of Space Geodesy Data. . (2021). Retrieved from https://cddis.nasa.gov/Data_and_Derived_Products/GNSS/orbit_products.html

Cefas. (2019). WaveNet. Retrieved from https://www.cefas.co.uk/data-and-publications/wavenet/

Chowdhury, S. R., Hossain, M. S., & Sharifuzzaman, S. (2014). A simple and inexpensive method for muddy shore profiling. *Chinese journal of oceanology and limnology, 32*(6), 1383-1391.

Coco, G., Senechal, N., Rejas, A., Bryan, K. R., Capo, S., Parisot, J., . . . MacMahan, J. H. (2014). Beach response to a sequence of extreme storms. *Geomorphology, 204*, 493-501.

Costa, B., Battista, T., & Pittman, S. (2009). Comparative evaluation of airborne LiDAR and ship-based multibeam SoNAR bathymetry and intensity for mapping coral reef ecosystems. *Remote Sensing of Environment, 113*(5), 1082-1100.

Datawell, Directional Waverider MkIII, brochure. (2021). Retrieved from https://www.datawell.nl/Portals/0/Documents/Brochures/datawell_brochure_dwr-mk3_b-09-09.pdf
Datawell, Mini Directional Waverider GPS. (2021). Retrieved from https://www.datawell.nl/Portals/0/Documents/Brochures/datawell_brochure_dwr-g4_b-06-10.pdf
Dennis, H. D., Evans, A. J., Banner, A. J., & Moore, P. J. (2018). Reefcrete: reducing the environmental footprint of concretes for eco-engineering marine structures. *Ecological Engineering, 120*, 668-678.
EA. (2019a). Environment Agency: Defra Survey Data Download, National LIDAR programme. Retrieved from https://environment.data.gov.uk/DefraDataDownload/?Mode=survey
EA. (2019b). Environment Agency: UK National Tide Gauge Network. Retrieved from https://www.bodc.ac.uk/data/hosted_data_systems/sea_level/uk_tide_gauge_network/
Elko, N., Briggs, T. R., Benedet, L., Robertson, Q., Thomson, G., Webb, B. M., & Garvey, K. (2021). A century of US beach nourishment. *Ocean & Coastal Management, 199*, 105406. doi:10.1016/j.ocecoaman.2020.105406
Elsner, P., Dornbusch, U., Thomas, I., Amos, D., Bovington, J., & Horn, D. (2018). Coincident beach surveys using UAS, vehicle mounted and airborne laser scanner: Point cloud inter-comparison and effects of surface type heterogeneity on elevation accuracies. *Remote Sensing of Environment, 208*, 15-26.
Emlid Reach M+ RTK GNSS module for precise navigation and UAV mapping. (2019).
European_GNSS_Agency. (2020). *GNSS user technology report. Issue 3, 2020*: Publications Office.
Fiorentino, L. A., Heitsenrether, R., & Krug, W. (2019). Wave Measurements From Radar Tide Gauges. *Frontiers in Marine Science, 6*, 586.
Frappart, F., Roussel, N., Darrozes, J., Bonneton, P., Bonneton, N., Detandt, G., . . . Loyer, S. (2016). High rate GNSS measurements for detecting non-hydrostatic surface wave. Application to tidal borein the Garonne River. *European Journal of Remote Sensing, 49*(1), 917-932.
Gao, S. (2019). Geomorphology and sedimentology of tidal flats. In *Coastal wetlands* (pp. 359-381): Elsevier.
GDAL/OGR_contributors. (2022). GDAL/OGR Geospatial Data Abstraction software Library. Open Source Geospatial Foundation. Retrieved from https://gdal.org
Glenn, S. M., Dickey, T. D., Parker, B., & Boicourt, W. (2000). Long-term real-time coastal ocean observation networks. *Oceanography, 13*(1), 24-34.
Gobron, K., de Viron, O., Wöppelmann, G., Poirier, É., Ballu, V., & Van Camp, M. (2019). Assessment of tide gauge biases and precision by the combination of multiple collocated time series. *Journal of Atmospheric and Oceanic Technology, 36*(10), 1983-1996.
Green, J., & Pugh, D. T. (2020). Bardsey–an island in a strong tidal stream: underestimating coastal tides due to unresolved topography. *Ocean Science, 16*(6), 1337-1345.
Habel, S., Fletcher, C. H., Barbee, M., & Anderson, T. R. (2016). The influence of seasonal patterns on a beach nourishment project in a complex reef environment. *Coastal Engineering, 116*, 67-76.
Hanley, M., Hoggart, S., Simmonds, D., Bichot, A., Colangelo, M., Bozzeda, F., . . . Recio, M. (2014). Shifting sands? Coastal protection by sand banks, beaches and dunes. *Coastal Engineering, 87*, 136-146. doi:10.1016/j.coastaleng.2013.10.020
Harley, M. D., Turner, I. L., Short, A. D., & Ranasinghe, R. (2011). Assessment and integration of conventional, RTK-GPS and image-derived beach survey methods for daily to decadal coastal monitoring. *Coastal Engineering, 58*(2), 194-205.
He, Y., Liu, J., Cai, F., Li, B., Qi, H., & Zhao, S. (2022). Aeolian sand transport influenced by tide and beachface morphology. *Geomorphology, 396*, 107987.
Hein, G. W., Landau, H., & Blomenhofer, H. (1990). Determination of instantaneous sea surface, wave heights, and ocean currents using satellite observations of the global positioning system. *Marine Geodesy, 14*(3-4), 217-224.
Holgate, S., Foden, P., Pugh, J., & Woodworth, P. (2008). Real time sea level data transmission from tide gauges for tsunami monitoring and long term sea level rise observations. *Journal of Operational Oceanography, 1*(1), 3-8. doi:10.1080/1755876X.2008.11081883

Houser, C., Hapke, C., & Hamilton, S. (2008). Controls on coastal dune morphology, shoreline erosion and barrier island response to extreme storms. *Geomorphology, 100*(3-4), 223-240.
Howarth, J., & Palmer, M. (2011). The liverpool bay coastal observatory. *Ocean Dynamics, 61*(11), 1917-1926.
IOC. (2016). Manual on sea level measurement and interpretation. Volume V - Radar gauges. IOC Manuals and Guides 14. Retrieved from https://unesdoc.unesco.org/ark:/48223/pf0000246981
Joseph, A., & Prabhudesai, R. (2006). Web-enabled and real-time reporting: Cellular based instrumentation for coastal sea level and surge monitoring. *The Indian Ocean Tsunami*, 247-257.
Kaplan, E. D., & Hegarty, C. (2017). *Understanding GPS/GNSS: Principles and applications*: Artech house.
Karegar, M., Kusche, J., Geremia-Nievinski, F., & Larson, K. (2021). *Raspberry Pi Reflector (RPR): a low-cost water-level monitoring system based on GNSS Interferometric Reflectometry.* Paper presented at the AGU Fall Meeting Abstracts.
Kelecy, T. M., Born, G. H., Parke, M. E., & Rocken, C. (1994). Precise mean sea level measurements using the Global Positioning System. *Journal of Geophysical Research: Oceans, 99*(C4), 7951-7959.
Kim, T.-h., Ramos, C., & Mohammed, S. (2017). Smart city and IoT. *76*, 159-162. doi:10.1016/j.future.2017.03.034
Klemas, V. (2011). Beach profiling and LIDAR bathymetry: An overview with case studies. *Journal of Coastal Research, 27*(6), 1019-1028. doi:10.2112/JCOASTRES-D-11-00017.1
Klobuchar, J. A. (1983). *Ionospheric Effects on Earth-Space Propagation* (ADA142725). Retrieved from https://apps.dtic.mil/sti/citations/ADA142725
Knight, P., Bird, C., Sinclair, A., Higham, J., & Plater, A. (2021). Testing an "IoT" tide gauge network for coastal monitoring. *IoT, 2*(1), 17-32.
Knight, P., Bird, C. O., Sinclair, A., & Plater, A. J. (2020). A low-cost GNSS buoy platform for measuring coastal sea levels. *Ocean Engineering, 203*, 107198. doi:10.1016/j.oceaneng.2020.107198
Larson, K. M., Löfgren, J. S., & Haas, R. (2013). Coastal sea level measurements using a single geodetic GPS receiver. *Advances in Space Research, 51*(8), 1301-1310.
Larson, K. M., Ray, R. D., & Williams, S. D. (2017). A 10-year comparison of water levels measured with a geodetic GPS receiver versus a conventional tide gauge. *Journal of Atmospheric and Oceanic Technology, 34*(2), 295-307.
Larson, M., & Kraus, N. C. (1994). Temporal and spatial scales of beach profile change, Duck, North Carolina. *Marine Geology, 117*(1-4), 75-94.
Lennon, G. W. (1971). Sea level instrumentation, its limitations and the optimisation of the performance of conventional gauges in Great Britain. *The International Hydrographic Review*.
Lin, Y.-P., Huang, C.-J., Chen, S.-H., Doong, D.-J., & Kao, C. C. (2017). Development of a GNSS buoy for monitoring water surface elevations in estuaries and coastal areas. *Sensors, 17*(1), 172.
Lyman, T. P., Elsmore, K., Gaylord, B., Byrnes, J. E., & Miller, L. P. (2020). Open Wave Height Logger: An open source pressure sensor data logger for wave measurement. *Limnology and Oceanography: Methods, 18*(7), 335-345. doi:10.1002/lom3.10370
MacIsaac, C., & Naeth, S. (2013). *TRIAXYS next wave II directional wave sensor the evolution of wave measurements.* Paper presented at the 2013 OCEANS-San Diego.
Marcos, M., Wöppelmann, G., Matthews, A., Ponte, R. M., Birol, F., Ardhuin, F., . . . Testut, L. (2019). Coastal sea level and related fields from existing observing systems. *Surveys in Geophysics, 40*(6), 1293-1317.
Martin Miguez, B., Testut, L., & Wöppelmann, G. (2012). Performance of modern tide gauges: towards mm-level accuracy. *Scientia Marina, 76*(S1), 221-228.
Martins, K., Blenkinsopp, C. E., Power, H. E., Bruder, B., Puleo, J. A., & Bergsma, E. W. (2017). High-resolution monitoring of wave transformation in the surf zone using a LiDAR scanner array. *Coastal Engineering, 128*, 37-43.

Mason, D., Gurney, C., & Kennett, M. (2000). Beach topography mapping—A comparsion of techniques. *Journal of Coastal Conservation, 6*(1), 113-124.
Masselink, G., & Anthony, E. J. (2001). Location and height of intertidal bars on macrotidal ridge and runnel beaches. *Earth Surface Processes and Landforms: The Journal of the British Geomorphological Research Group, 26*(7), 759-774.
Masselink, G., Kroon, A., & Davidson-Arnott, R. (2006). Morphodynamics of intertidal bars in wave-dominated coastal settings—a review. *Geomorphology, 73*(1-2), 33-49.
Masselink, G., & Short D. , A. (1993). The Effect of Tide Range on Beach Morphodynamics and Morphology: A Conceptual Beach Model. *Journal of Coastal Research, 9*(3), 785-800. Retrieved from http://www.jstor.org/stable/4298129
Measurement Specialties, MS5837-02BA Data Sheet. (2020). Retrieved from https://www.te.com/commerce/DocumentDelivery/DDEController?Action=srchrtrv&DocNm=MS5837-02BA01&DocType=Data+Sheet&DocLang=English&DocFormat=pdf&PartCntxt=CAT-BLPS0059
Metters, D., Shayer, J., Ryan, J., Bourner, J., Corbett, B., & Tomlinson, R. (2017). *Strategic and cost-effective networks of miniaturised tide gauges*. Paper presented at the Australasian Coasts & Ports 2017: Working with Nature.
Miguez, B. M., Testut, L., & Wöppelmann, G. (2008). The Van de Casteele test revisited: an efficient approach to tide gauge error characterization. *Journal of Atmospheric and Oceanic Technology, 25*(7), 1238-1244. doi:10.1175/2007JTECHO554.1
Míguez, B. M., Testut, L., & Wöppelmann, G. (2012). Performance of modern tide gauges: towards mm-level accuracy. *Scientia Marina, 76*(S1), 221-228. doi:10.3989/scimar.03618.18A
Miles, A., Ilic, S., Whyatt, D., & James, M. R. (2019). Characterizing beach intertidal bar systems using multi-annual LiDAR data. *Earth Surface Processes and Landforms, 44*(8), 1572-1583.
Miller, L. P., & Neumeier, U. (2019). Oceanwaves: Ocean wave statistics (R). Retrieved from https://cran.r-project.org/web/packages/oceanwaves/index.html
Montreuil, A.-L., Moelans, R., Houthuys, R., Bogaert, P., & Chen, M. (2020). Characterization of intertidal bar morphodynamics using a bi-annual LiDAR dataset. *Remote Sensing, 12*(22), 3841.
Moore, R. D., Wolf, J., Souza, A. J., & Flint, S. S. (2009). Morphological evolution of the Dee Estuary, Eastern Irish Sea, UK: A tidal asymmetry approach. *Geomorphology, 103*(4), 588-596.
Morales Maqueda, M., Penna, N., Williams, S., Foden, P., Martin, I., & Pugh, J. (2016). Water surface height determination with a GPS wave glider: a demonstration in Loch Ness, Scotland. *Journal of Atmospheric and Oceanic Technology, 33*(6), 1159-1168.
National Oceanography Centre (2019). POLTIPS-3: Coastal Tidal Software. Retrieved from http://noc.ac.uk/business/marine-data-products/coastal
National Oceanography Centre, National Tidal & Sea Level Facility: Liverpool tide gauge statistics. (2020). Retrieved from https://www.ntslf.org/tgi/portinfo?port=Liverpool
NERC, British Isles continuous GNSS facility (BIGF). (2021). Retrieved from http://www.bigf.ac.uk/
Neumeier, U. (2020). Oceanwaves: Ocean wave statistics (Matlab). Retrieved from http://neumeier.perso.ch/matlab/waves.html
Nicholls, R. J., Wong, P. P., Burkett, V., Codignotto, J., Hay, J., McLean, R., . . . Arblaster, J. (2007). Coastal systems and low-lying areas.
Noll, C. E. (2010). The Crustal Dynamics Data Information System: A resource to support scientific analysis using space geodesy. *Advances in Space Research, 45*(12), 1421-1440.
Nortek manuals. (2020). *Nortek.* Retrieved from https://support.nortekgroup.com/hc/en-us/categories/360001447411-Manuals
O'Dea, A., Brodie, K. L., & Hartzell, P. (2019). Continuous coastal monitoring with an automated terrestrial lidar scanner. *Journal of Marine Science and Engineering, 7*(2), 37.
Penna, N. T., Morales Maqueda, M. A., Martin, I., Guo, J., & Foden, P. R. (2018). Sea surface height measurement using a GNSS wave glider. *Geophysical Research Letters, 45*(11), 5609-5616.

Pérez, B., Álvarez Fanjul, E., Pérez, S., de Alfonso, M., & Vela, J. (2013). Use of tide gauge data in operational oceanography and sea level hazard warning systems. In *Journal of Operational Oceanography* (Vol. 6, pp. 1-18).
Pırtı, A. (2021). Evaluating the accuracy of post-processed kinematic (PPK) positioning technique. *Geodesy and Cartography, 47*(2), 66-70.
Poate, T., Kingston, K., Masselink, G., & Russell, P. (2009). Response of high-energy, macrotidal beaches to seasonal changes in wave conditions: examples from North Cornwall, UK. *Journal of Coastal Research*, 747-751.
Pugh, D. (1972). The Physics of Pneumatic Tide Gauges. *International Hydrographic Review, 49*.
Pugh, D. (1987). Tides, surges and mean sea level.
Pugh, D., & Woodworth, P. (2014). *Sea-level science: understanding tides, surges, tsunamis and mean sea-level changes*: Cambridge University Press.
Rabinovich, A. (2010). *Handbook of coastal and ocean engineering, Seiches and Harbor Oscillations*: World Scientific.
Rocken, C., Kelecy, T. M., Born, G. H., Young, L. E., Purcell Jr, G. H., & Wolf, S. K. (1990). Measuring precise sea level from a buoy using the global positioning system. *Geophysical Research Letters, 17*(12), 2145-2148.
Roussel, N., Ramillien, G., Frappart, F., Darrozes, J., Gay, A., Biancale, R., . . . Allain, D. (2015). Sea level monitoring and sea state estimate using a single geodetic receiver. *Remote Sensing of Environment, 171*, 261-277.
RTKLIB. (2018). Open source program package for GNSS positioning. Retrieved from http://www.rtklib.com
Russell, P. E. (1993). Mechanisms for beach erosion during storms. *Continental Shelf Research, 13*(11), 1243-1265. doi:10.1016/0278-4343(93)90051-X
Sallenger Jr, A., Krabill, W., Swift, R., Brock, J., List, J., Hansen, M., . . . Meredith, A. (2003). Evaluation of airborne topographic lidar for quantifying beach changes. *Journal of Coastal Research*, 125-133.
Saye, S., Van der Wal, D., Pye, K., & Blott, S. (2005). Beach–dune morphological relationships and erosion/accretion: an investigation at five sites in England and Wales using LIDAR data. *Geomorphology, 72*(1-4), 128-155.
Scott, T., Masselink, G., O'Hare, T., Saulter, A., Poate, T., Russell, P., . . . Conley, D. (2016). The extreme 2013/2014 winter storms: Beach recovery along the southwest coast of England. *Marine Geology, 382*, 224-241. doi:10.1016/j.margeo.2016.10.011
Scott, T., Masselink, G., & Russell, P. (2011). Morphodynamic characteristics and classification of beaches in England and Wales. *Marine Geology, 286*(1-4), 1-20.
Soomere, T. (2005). Fast ferry traffic as a qualitatively new forcing factor of environmental processes in non-tidal sea areas: a case study in Tallinn Bay, Baltic Sea. *Environmental Fluid Mechanics, 5*(4), 293-323.
Spodar, A., Héquette, A., Ruz, M.-H., Cartier, A., Grégoire, P., Sipka, V., & Forain, N. (2018). Evolution of a beach nourishment project using dredged sand from navigation channel, Dunkirk, northern France. *Journal of Coastal Conservation, 22*(3), 457-474.
Spotter: the agile metocean buoy. (2021). Retrieved from https://www.sofarocean.com/products/spotter
Stal, C., Poppe, H., Vandenbulcke, A., & De Wulf, A. (2016). Study of post-processed GNSS measurements for tidal analysis in the Belgian North Sea. *Ocean Engineering, 118*, 165-172.
Stive, M., De Schipper, M. A., Luijendijk, A., Ranasinghe, R., Van Thiel De Vries, J., Aarninkhof, S., . . . Marx, S. (2013). *The Sand Engine: A solution for vulnerable deltas in the 21st century?* Paper presented at the Coastal Dynamics 2013: 7th International Conference on Coastal Dynamics, Arcachon, France, 24-28 June 2013.
Stringari, C. E., & Power, H. (2022). Picoastal: A low-cost coastal video monitoring system. *SoftwareX, 18*, 101073.
Taherkhani, M., Vitousek, S., Barnard, P. L., Frazer, N., Anderson, T. R., & Fletcher, C. H. (2020). Sea-level rise exponentially increases coastal flood frequency. *Scientific reports, 10*(1), 1-17.
Tallysman. (2019). Tallysman TW4721 performance measurements. Retrieved from https://www.tallysman.com/wp-content/uploads/TW4721-Measurements.pdf

Telling, J., Lyda, A., Hartzell, P., & Glennie, C. (2017). Review of Earth science research using terrestrial laser scanning. *Earth-Science Reviews, 169*, 35-68.
Thomas, T., Phillips, M., & Williams, A. (2011). Sheltering effects of an offshore island: short-term morphological response of a macro-tidal beach. *Journal of Coastal Research*, 1204-1208.
Thorne, P. D., Lichtman, I. D., & Hurther, D. (2021). Acoustic scattering characteristics and inversions for suspended concentration and particle size above mixed sand and mud beds. *Continental Shelf Research, 214*, 104320.
Ton, A., Lee, M., Vos, S., Gawehn, M., den Heijer, K., & Aarninkhof, S. (2020). Beach and nearshore monitoring techniques. In *Sandy Beach Morphodynamics* (pp. 659-687): Elsevier.
Tucker, M. J., & Pitt, E. G. (2001). *Waves in ocean engineering*.
Turner, R. K., Burgess, D., Hadley, D., Coombes, E., & Jackson, N. (2007). A cost–benefit appraisal of coastal managed realignment policy. *Global Environmental Change, 17*(3-4), 397-407.
Turvey, R. (2007). Vulnerability assessment of developing countries: the case of small-island developing states. *Development Policy Review, 25*(2), 243-264.
U-blox. (2016). White Paper: Achieving Centimeter Level Performance with Low Cost Antennas. . Retrieved from https://www.u-blox.com/en/white-papers
U-blox. (2019a). Application Note: GPS Antennas, RF design considerations for U-blox GPS Receivers. Retrieved from https://www.u-blox.com/sites/default/files/products/documents/GPS-Antenna_AppNote_(GPS-X-08014).pdf
U-blox. (2019b). Product details for M8T series GNSS receivers. Retrieved from https://www.u-blox.com/en/product/neolea-m8t-series
UK National Tide Gauge Network. (2019). Retrieved from https://www.bodc.ac.uk/data/hosted_data_systems/sea_level/uk_tide_gauge_network/
Van den Hoek, R., Brugnach, M., & Hoekstra, A. Y. (2012). Shifting to ecological engineering in flood management: Introducing new uncertainties in the development of a building with nature pilot project. *Environmental Science & Policy, 22*, 85-99.
Walvin, S., & Mickovski, S. (2015). *A comparative study of beach nourishment methods in selected areas of the coasts of the United Kingdom and The Netherlands*. Paper presented at the Coastal Cities and Their Sustainable Future, WIT Transactions on the Built Environment.
Watson, C., Coleman, R., & Handsworth, R. (2008). Coastal tide gauge calibration: a case study at Macquarie Island using GPS buoy techniques. *Journal of Coastal Research, 24*(4), 1071-1079.
WaveNet. (2022). Strategic wave monitoring network for the United Kingdom. Retrieved from https://www.cefas.co.uk/data-and-publications/wavenet/
Williams, S. D., Bell, P. S., McCann, D. L., Cooke, R., & Sams, C. (2020). Demonstrating the potential of low-cost GPS units for the remote measurement of tides and water levels using interferometric reflectometry. *Journal of Atmospheric and Oceanic Technology, 37*(10), 1925-1935.
Wolf, J. (2008). Coupled wave and surge modelling and implications for coastal flooding. *Advances in Geosciences, 17*, 19-22.
Wolf, J., & Bell, P. (2001). Waves at Holderness from X-band radar. *Coastal Engineering, 43*(3-4), 247-263.
Wolf, J., Brown, J. M., & Howarth, M. J. (2011). The wave climate of Liverpool Bay—observations and modelling. *Ocean Dynamics, 61*(5), 639-655.
Woodworth, P. L. (1999). High waters at Liverpool since 1768: the UK's longest sea level record. *Geophysical Research Letters, 26*(11), 1589-1592.
Woodworth, P. L., & Smith, D. E. (2003). A one year comparison of radar and bubbler tide gauges at Liverpool. *The International Hydrographic Review*.
Wright, L. D., & Short, A. D. (1984). Morphodynamic variability of surf zones and beaches: a synthesis. *Marine Geology, 56*(1-4), 93-118.
Xie, W., He, Q., Zhang, K., Guo, L., Wang, X., Shen, J., & Cui, Z. (2017). Application of terrestrial laser scanner on tidal flat morphology at a typhoon event timescale. *Geomorphology, 292*, 47-58.

Zanutta, A., Lambertini, A., & Vittuari, L. (2020). UAV photogrammetry and ground surveys as a mapping tool for quickly monitoring shoreline and beach changes. *Journal of Marine Science and Engineering, 8*(1), 52.

8 Appendix

8.1 Arduino tide gauge software

The following tools and software drivers were used in the development of the IoT tide gauge software scripts (see chapter 3). The software developed as part of this research are listed in sections 8.1.1 and 8.1.2 below; Section 8.1.1 lists the script for the river installation alongside Liverpool docks (configuration-1), and section 8.1.2 lists the script for the intertidal installation on Crosby beach (configuration-2).

The Arduino IDE package was used to create software for the different tide gauge configurations; this package has an editor, a live debugger, inbuilt standard Arduino subroutines and facilitates transfer of code to the Arduino microcontroller:

https://www.arduino.cc/en/software

The software has been written in the C++ language. https://www.arduino.cc/reference/en/

The following links are for sensor software drivers used in the development of the IoT tide gauge:

Software drivers for MS5803 series of pressure sensors:

https://github.com/millerlp/MS5803_02

Blue Robotics driver for the MS5837 pressure sensor:

https://github.com/bluerobotics/BlueRobotics_MS5837_Library

Bosch Sensortec BME280 atmospheric sensor:

https://www.arduino.cc/reference/en/libraries/bme280/

The real-time data were sent to the Sigfox cloud server with access and forwarding of data via the Sigfox Backend online system. The following links document this process.

https://support.sigfox.com/docs/backend-user-account-creation

https://support.sigfox.com/docs

Tutorial on how to connect MKR FOX 1200 to work with Sigfox

https://docs.arduino.cc/tutorials/mkr-fox-1200/sigfox-first-configuration

8.1.1 Liverpool docks deployment (configuration-1)

```
/*
Program: SigfoxTideGauge_v4_BlueRobotics.ino
SigFox Tide Gauge Version 2
  Does 40 second average of sensor data to eliminate effect of waves
  Uses 2 bar pressure sensor
  Outputs data to Sigfox Cloud server; sea temperature, air temperature, air pressure
  water pressure, humidity and message status
  Date and time applied at server end
*/

#include <ArduinoLowPower.h>
#include <SigFox.h>
#include <Wire.h>
#include <SPI.h>
#include <Adafruit_BME280.h>
#include <Adafruit_Sensor.h>
#include <MS5837.h>
#include "conversions.h"

// Set oneshot to false to trigger continuous mode when you finished setting up the whole flow
int oneshot = false;

Adafruit_BME280  bme;


// MS5837 sensor
MS5837 sensor;
```

```
float TotNum;
unsigned long counter;
unsigned long time_elapsed;
unsigned long time_start;
unsigned long time_now;

#define STATUS_OK     0
#define STATUS_BME_KO 1
#define STATUS_PRS_KO 2

#define SLEEPTIME 15 * 60 * 1000

float alarm_source;

/*
   ATTENTION - the structure we are going to send MUST
   be declared "packed" otherwise we'll get padding mismatch
   on the sent data - see http://www.catb.org/esr/structure-packing/#_structure_alignment_and_padding
   for more details
*/
typedef struct __attribute__ ((packed)) sigfox_message {
  uint8_t status;
  int16_t sensorTemperature;
  int16_t bmeTemperature;
  uint16_t bmePressure;
  uint16_t bmeHumidity;
  uint16_t sensorPressure;
  uint8_t lastMessageStatus;
} SigfoxMessage;

// stub for message which will be sent
SigfoxMessage msg;
```

```
void setup() {

  if (oneshot == true) {
    // Wait for the serial
    Serial.begin(9600);
    while (!Serial) {}
  }

LowPower.attachInterruptWakeup(RTC_ALARM_WAKEUP,alarmEvent0,CHANGE);

  if (!SigFox.begin()) {
    // Something is really wrong, try rebooting
    // Reboot is useful if we are powering the board using an unreliable power source
    // (eg. solar panels or other energy harvesting methods)
    reboot();
  }

  //Send module to standby until we need to send a message
  SigFox.end();

  if (oneshot == true) {
    // Enable debug prints and LED indication if we are testing
    SigFox.debug();
  }

// Added this to make it work
    SigFox.debug();

    bool status;
    delay(2000);
```

```
  // default settings
  // (you can also pass in a Wire library object like &Wire2)
  status = bme.begin();
  if (!status) {
      Serial.println("Could not find a valid BME280 sensor, check wiring!");
      while (1);
  }

 delay(1000);

// Initialize pressure sensor
// Returns true if initialization was successful
// We can't continue with the rest of the program unless we can initialize the sensor

 Wire.begin();
  while (!sensor.init()) {
   Serial.println("Init failed!");
   Serial.println("Are SDA/SCL connected correctly?");
   Serial.println("Blue Robotics Bar30: White=SDA, Green=SCL");
   Serial.println("\n\n\n");
   delay(5000);
  }

  sensor.setModel(MS5837::MS5837_02BA);
  sensor.setFluidDensity(1029); // kg/m^3 (freshwater, 1029 for seawater)

   Serial.println();

}

void loop() {
  // Every 15 minutes, read all the sensors and send them
```

```
  // Let's try to optimize the data format
  // Only use floats as intermediate representation, don't send them directly

float AvgNum = 0;
float pressure;
float temperature;
float humidity;
float pressure1;
float temperature1;

while (time_elapsed < 40000) {

  pressure = bme.readPressure() / 100.0F;
  temperature = bme.readTemperature();
  humidity = bme.readHumidity();

  sensor.read();
  pressure1 = sensor.pressure();
  temperature1 = sensor.temperature();

// Add up 40 seconds of pressure readings
  TotNum += pressure1;

    time_now  = millis();
  if (counter == 0) {
    time_start = time_now;
  }

// Catch Rollover of millis when it gets to 2^32 and resets itself (i.e. ~ 49 days)

 if (time_now < time_start) {
  unsigned long time_biggest = 4294967295;
```

```
 time_elapsed = time_biggest - time_start;
 time_elapsed = time_elapsed + time_now;
 }
 else {
 time_elapsed = time_now - time_start;
 }

// Using counter for average since this slightly varies within the 40 second period
 counter++;

}

 AvgNum = TotNum/float(counter);

// Reset variables for after sleep period
 TotNum = 0.0;
 counter = 0;
 time_elapsed = 0;

// Append output to msg :  Remember order received by SigFox is the order as set in the typedef (see above)
 msg.bmePressure = convertoFloatToUInt16(pressure, 2100);
 msg.bmeTemperature = convertoFloatToInt16(temperature, 60, -60);
 msg.bmeHumidity = convertoFloatToUInt16(humidity, 120);
 msg.sensorPressure = convertoFloatToUInt16(AvgNum, 2100);
 msg.sensorTemperature = convertoFloatToInt16(temperature1, 60, -60);

 // Start the module
 SigFox.begin();
 // Wait at least 30ms after first configuration (100ms before)
 delay(100);
```

```
  if (oneshot == true) {
    Serial.println("Air pressure: " + String(pressure));
    Serial.println("Air temperature: " + String(temperature));
    Serial.println("Water pressure: " + String(pressure1));
    Serial.println("Water temperature: " + String(temperature1));
    Serial.println("Air humidity: " + String(humidity));
  }

  // Clears all pending interrupts
  SigFox.status();
  delay(1);

  SigFox.beginPacket();
  SigFox.write((uint8_t*)&msg, 12);

  msg.lastMessageStatus = SigFox.endPacket();

  if (oneshot == true) {
    Serial.println("Status: " + String(msg.lastMessageStatus));
  }

  SigFox.end();

  if (oneshot == true) {
    // spin forever, so we can test that the backend is behaving correctly
    while (1) {}
  }

  //Sleep for 10 minutes
  LowPower.sleep(SLEEPTIME);
}
```

```
void reboot() {
  NVIC_SystemReset();
  while (1);
}

void alarmEvent0() {
  alarm_source = 0;
}
```

8.1.2 Crosby beach deployment (configuration-2)

```
/*
  Program: TideGauge_v4 (Buffering version)
  Whole unit under water and thus sends the buffered data once the tide has gone out
  Does 40 second average of sensor data to eliminate effect of waves
  Uses 2bar Blue Robotics pressure sensor
  Note: Real-time clock needs separate power supply
  Pass through mon, day, hr and min, plus 4 water pressure archives

  Records the 40 second data burst at 10Hz to microSD card
  Calculates statistics and records to microSD card
  Sending averages via SigFox

  Plus buffering
*/

#include <ArduinoLowPower.h>
#include <SigFox.h>
#include <Wire.h>
#include <SPI.h>
#include <RTCZero.h>
#include <SdFat.h>
#include<stdio.h>
#include <MS5837.h>
#include "conversions.h"

//  RTC clock
RTCZero rtc;



// ***************************************************************
/* Change these values to set the current initial date and time */
```

```
// ****************************************************************
const byte day = 14;
const byte month = 2;
const byte year = 20;

const byte seconds = 0;
const byte minutes = 15;
const byte hours = 9;


const int chipSelect = 4;


// Set oneshot to false to trigger continuous mode when you finished setting up the whole flow
int oneshot = true;

// MS5837 sensor
MS5837 sensor;


float TotNum;
unsigned long counter;
unsigned long time_elapsed;
unsigned long time_start;
unsigned long time_now;



// Set up start criteria for delayed mode sending
int nc = 1;
int nc_send = 1;
int bufmon[49];
```

```
int bufday[49];
int bufhr[49];
int bufmin[49];
float bufprs[49];


#define STATUS_OK     0
#define STATUS_BME_KO 1
#define STATUS_PRS_KO 2

#define SLEEPTIME 15 * 60 * 1000

float alarm_source;

SdFat sd;
File dataFile;
SdFile file;


/*
   ATTENTION - the structure we are going to send MUST
   be declared "packed" otherwise we'll get padding mismatch
   on the sent data - see http://www.catb.org/esr/structure-packing/#_structure_alignment_and_padding
   for more details
*/


typedef struct __attribute__ ((packed)) sigfox_message {
  uint8_t myMon;
  uint8_t myDay;
  uint8_t myHr;
  uint8_t myMin;
```

```
  uint16_t sensorPressure1;
  uint16_t sensorPressure2;
  uint16_t sensorPressure3;
  uint16_t sensorPressure4;
} SigfoxMessage;


// stub for message which will be sent
SigfoxMessage msg;

void setup() {

  if (oneshot == true) {
    // Wait for the serial
    Serial.begin(9600);
    while (!Serial) {}
  }

LowPower.attachInterruptWakeup(RTC_ALARM_WAKEUP,alarmEvent0,CHANGE);

  if (!SigFox.begin()) {
    // Something is really wrong, try rebooting
    // Reboot is useful if we are powering the board using an unreliable power source
    // (eg. solar panels or other energy harvesting methods)
    reboot();
  }

  //Send module to standby until we need to send a message
  SigFox.end();

  if (oneshot == true) {
    // Enable debug prints and LED indication if we are testing
```

```
  SigFox.debug();
 }

// Added this to make it work
  SigFox.debug();

  bool status;
  delay(2000);


 // Initialize pressure sensor
 // Returns true if initialization was successful
 // We can't continue with the rest of the program unless we can initialize the sensor

 Wire.begin();

  while (!sensor.init()) {
    if (oneshot == true) {
   Serial.println("Init failed!");
   Serial.println("Are SDA/SCL connected correctly?");
   Serial.println("Blue Robotics 2Bar: White=SDA, Green=SCL");
   Serial.println("\n\n\n");
    }
   delay(5000);

  }

  sensor.setModel(MS5837::MS5837_02BA);
  sensor.setFluidDensity(1029); // kg/m^3 (freshwater, 1029 for seawater)

// Initialize RTC
  rtc.begin(); // initialize RTC
```

```
// Set the time
  rtc.setHours(hours);
  rtc.setMinutes(minutes);
  rtc.setSeconds(seconds);

// Set the date
  rtc.setDay(day);
  rtc.setMonth(month);
  rtc.setYear(year);

// you can use also
//rtc.setTime(hours, minutes, seconds);
//rtc.setDate(day, month, year);

// SD card
   if (oneshot == true) {
     Serial.print("Initializing SD card...");
   }

   if (!sd.begin(chipSelect, SD_SCK_MHZ(50))) sd.initErrorHalt();

   if (oneshot == true) {
     Serial.println("card initialized.");
   }

}

void loop() {
  // Every 15 minutes, read all the sensors and send them
  // Let's try to optimize the data format
  // Only use floats as intermediate representation, don't send them directly
```

```
float AvgNum = 0;
float pressure1;
float temperature1;
int pMon,pDay,pHr,pMin,pSec,pYr;
char fname[12];
float mymax = -9999.9;
float mymin =  9999.9;



if (oneshot == true) {

    Serial.println("Starting loop");
    Serial.println("time elapsed: " + String(time_elapsed));
    Serial.println("counter: " + String(counter));




  }

// open the file for write at end like the Native SD library
  sprintf(fname, "%02d%02d%02d%02d.txt", rtc.getMonth(),rtc.getDay(), rtc.getHours(),
rtc.getMinutes());

 if (oneshot == true) {
  Serial.println(fname);
  }
  if (!file.open(fname, O_WRITE | O_CREAT | O_AT_END)) {

    sd.errorHalt("opening test.txt for write failed");

  }
```

```
while (time_elapsed < 40000) {

  sensor.read();
  pressure1 = sensor.pressure();
  temperature1 = sensor.temperature();

// Keep track of max and min azE
    mymax = max(pressure1,mymax);
    mymin = min(pressure1,mymin);

// Add up 40 seconds of pressure readings
  TotNum += pressure1;

  time_now  = millis();

// Write to SD card this 40 second burst

  file.print(time_now);
  file.write(' ');
  file.print(pressure1);
  file.write(' ');
  file.println(temperature1);


  if (counter == 0) {
    time_start = time_now;
  }

  time_elapsed = time_now - time_start;
```

```
// Using counter for average since this slightly varies within the 40 second period
  counter++;

}

  AvgNum = TotNum/float(counter);

// Get date and time for passing via SigFox
 pYr  = rtc.getYear();
 pMon = rtc.getMonth();
 pDay = rtc.getDay();
 pHr  = rtc.getHours();
 pMin = rtc.getMinutes();
 pSec = rtc.getSeconds();

  char datim[17];
  sprintf(datim, "%02d/%02d/%02d %02d:%02d:%02d", pDay, pMon,pYr,pHr,pMin,pSec);
// Log data
//  File dataFile = SD.open("datalog.txt", FILE_WRITE);

  // if the file is available, write to it:
  if (fname) {
//    sprintf(datim, "%02d/%02d/%02d %02d:%02d:%02d", rtc.getDay(), rtc.getMonth(),
rtc.getYear(), rtc.getHours(), rtc.getMinutes(), rtc.getSeconds());
    file.print(datim);
    file.print(" ");
    file.print(AvgNum);
    file.print(" ");
    file.print(mymax);
    file.print(" ");
    file.print(mymin);
    file.println(" ");
    file.close();
```

```
 }
 // if the file isn't open, pop up an error:
 else {
   if (oneshot == true) {
   Serial.println("error opening datalog.txt");
   }
 }
```

// Append output to msg : Remember order received by SigFox is the order as set in the typedef (see above)

```
// Resets array counter
 if (nc > 48 ) {
  nc = 1;
 }

// Resets message sent counter
 if (nc_send > 45) {
  nc_send = 1;
 }

 if (AvgNum > 1050) {
  bufmon[nc] = pMon;
  bufday[nc] = pDay;
  bufhr[nc]  = pHr;
  bufmin[nc] = pMin;
  bufprs[nc] = AvgNum;
  nc = nc + 1;
  nc_send = 1;
 }
```

```
 else {

// Add to SigFox message
  msg.myMon = (uint8_t) bufmon[nc_send];
  msg.myDay = (uint8_t) bufday[nc_send];
  msg.myHr  = (uint8_t) bufhr[nc_send];
  msg.myMin = (uint8_t) bufmin[nc_send];
// Testing send the nc_send counter back
//    msg.myMin = (uint8_t) nc_send;
// msg.sensorPressure1 = convertoFloatToUInt16(bufprs[nc_send], 2100);
// Testing send current average air pressure back (i.e., pressure its now recording)
  msg.sensorPressure1 = convertoFloatToUInt16(AvgNum, 2100);
  msg.sensorPressure2 = convertoFloatToUInt16(bufprs[nc_send+1], 2100);
  msg.sensorPressure3 = convertoFloatToUInt16(bufprs[nc_send+2], 2100);
  msg.sensorPressure4 = convertoFloatToUInt16(bufprs[nc_send+3], 2100);

  if (oneshot == true) {
    Serial.println("Buffer Month = " + String(bufmon[nc_send]));
    Serial.println("Buffer Day = " + String(bufday[nc_send]));
    Serial.println("Buffer Hour = " + String(bufhr[nc_send]));
    Serial.println("Buffer Minute = " + String(bufmin[nc_send]));
    Serial.println("Buffer pressure 1 = " + String(bufprs[nc_send]));
    Serial.println("Buffer pressure 2 = " + String(bufprs[nc_send+1]));
    Serial.println("Buffer pressure 3 = " + String(bufprs[nc_send+2]));
    Serial.println("Buffer pressure 4 = " + String(bufprs[nc_send+3]));
  }

// Do SigFox stuff here


    // Start the module
    SigFox.begin();
```

```
    // Wait at least 30ms after first configuration (100ms before)
    delay(100);

    // Clears all pending interrupts
    SigFox.status();
    delay(1);
    SigFox.beginPacket();
    SigFox.write((uint8_t*)&msg, 12);
    int my_lastMessageStatus = SigFox.endPacket();
    SigFox.end();

    nc_send = nc_send + 4;
    nc = 1;
 }

if (oneshot == true) {
    Serial.println("Water pressure: " + String(pressure1));
    Serial.println("Water temperature: " + String(temperature1));
    Serial.println("Water pressure average: " + String(AvgNum));
    Serial.println("time elapsed: " + String(time_elapsed));
    Serial.println("counter: " + String(counter));
}




  if (oneshot == true) {
    // spin forever, so we can test that the backend is behaving correctly
    while (1) {}
  }

// Reset variables for after sleep period
```

```
  TotNum = 0.0;
  counter = 0;
  time_elapsed = 0;

//  delay(10000);
  //Sleep for 15 minutes
  delay(1000);
//  LowPower.sleep(SLEEPTIME);
  delay(SLEEPTIME);
}

void reboot() {
  NVIC_SystemReset();
  while (1);
}

void alarmEvent0() {
  alarm_source = 0;
}
```

8.2 IoT processing and online display of real-time data

Data were transmitted to the SigFox Back-End cloud server. Once processed, these data were then automatically pushed to ThingSpeak cloud server. The ThingSpeak cloud server (https://thingspeak.com/) allows for Matlab scripts to be used to convert the Ascii data in compressed format to standard units of measurement e.g., mb, degrees C, for online graphical display (using a conventional internet browser).

Sigfox Back-End cloud server → ThingSpeak cloud Server

In addition, the ThingView Android/Apple application was used to display the graphical outputs for mobile devices e.g., the android version can be found at the following location, https://play.google.com/store/apps/details?id=com.cinetica_tech.thingview&hl=en&gl=US).

8.2.1 Matlab script to convert Ascii data to standard units on ThingSpeak cloud server

```
% Template MATLAB code for reading data from a private channel, analyzing
% the data and storing the analyzed data in another channel.


% Prior to running this MATLAB code template, assign the channel ID to read
% data from to the 'readChannelID' variable. Since this is a private
% channel, also assign the read API Key to the 'readAPIKey' variable. You
% can find the read API Key in the right side pane of this page.


% To store the analyzed data, you will need to write it to a channel other
% than the one you are reading data from. Assign this channel ID to the
% 'writeChannelID' variable. Also assign the write API Key to the
% 'writeAPIKey' variable below. You can find the write API Key in the right
% side pane of this page.


% TODO - Replace the [] with channel ID to read data from:
readChannelID = 523344;
% TODO - Enter the Read API Key between the '' below:
readAPIKey = 'HFW5CNV0MT3B331L';


% TODO - Replace the [] with channel ID to write data to:
writeChannelID = 523347;
% TODO - Enter the Write API Key between the '' below:
writeAPIKey = 'R7LTC6A6CY1GWMH3';


%% Read Data %%
data = thingSpeakRead(readChannelID, 'ReadKey', readAPIKey);
```

```
%% Analyze Data %%
% Add code in this section to analyze data and store the result in the
% analyzedData variable
analyzedData = data;
display(data(1,:));


%% Analyze Data %%
INT16_t_MAX = 32767;
UINT16_t_MAX = 65536;
analyzedData(1,1) = data(1,1) / INT16_t_MAX * 120 ;
analyzedData(1,3) = data(1,3) / INT16_t_MAX * 120 ;
analyzedData(1,2) = data(1,2) / UINT16_t_MAX * 2100 ;
analyzedData(1,5) = data(1,5) / UINT16_t_MAX * 2100 ;
analyzedData(1,4) = (data(1,4)) / UINT16_t_MAX * 110 ;
%% Write Data %%
thingSpeakWrite(writeChannelID, analyzedData, 'WriteKey', writeAPIKey);
%% Schedule action: React -> every 10 minutes


display(analyzedData);
```

8.2.2 ThingSpeak Matlab code (screen dump of online interface)

This code was applied to convert the Ascii data from the IoT device to standard SI units of measurement.

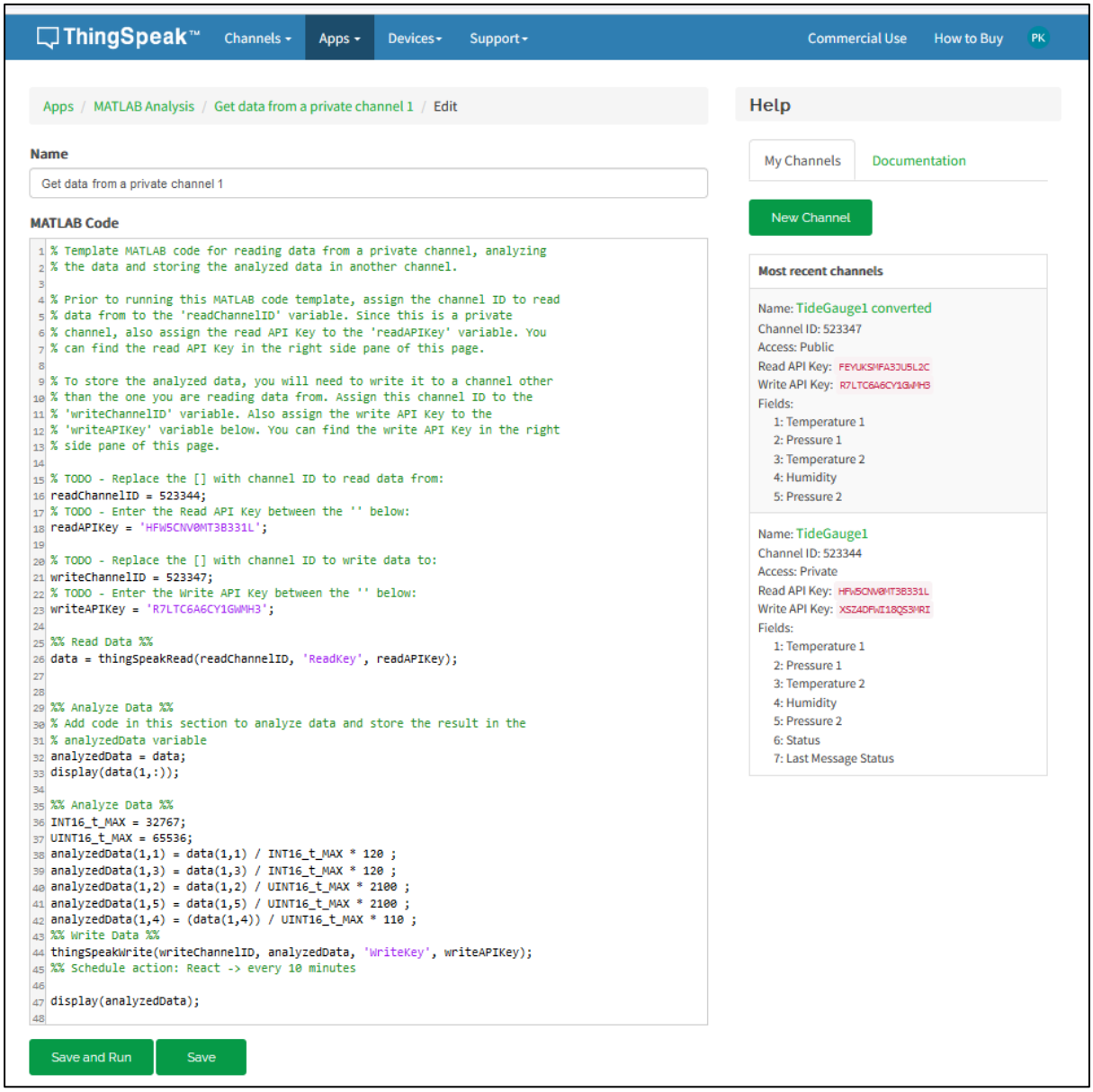

8.2.3 ThingSpeak My Channels on ThingSpeak website (screen dump of online interface)

Web page showing the raw and converted channels. Private is to keep the data unseen to the public interface, whereas Public allows access to the data plots.

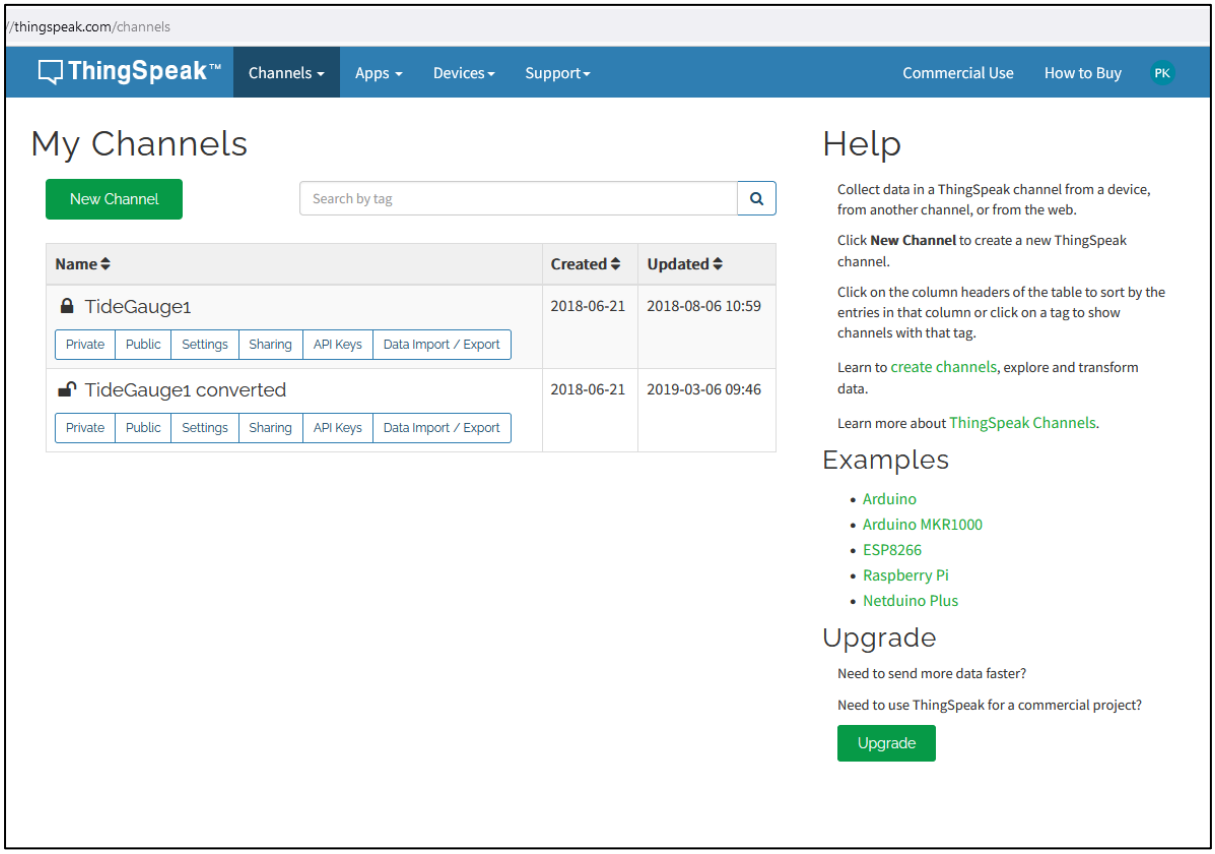

8.2.4 ThingSpeak Private view of real-time data via ThingSpeak website (screen dump)

This is an example of output plots in raw units before conversion.

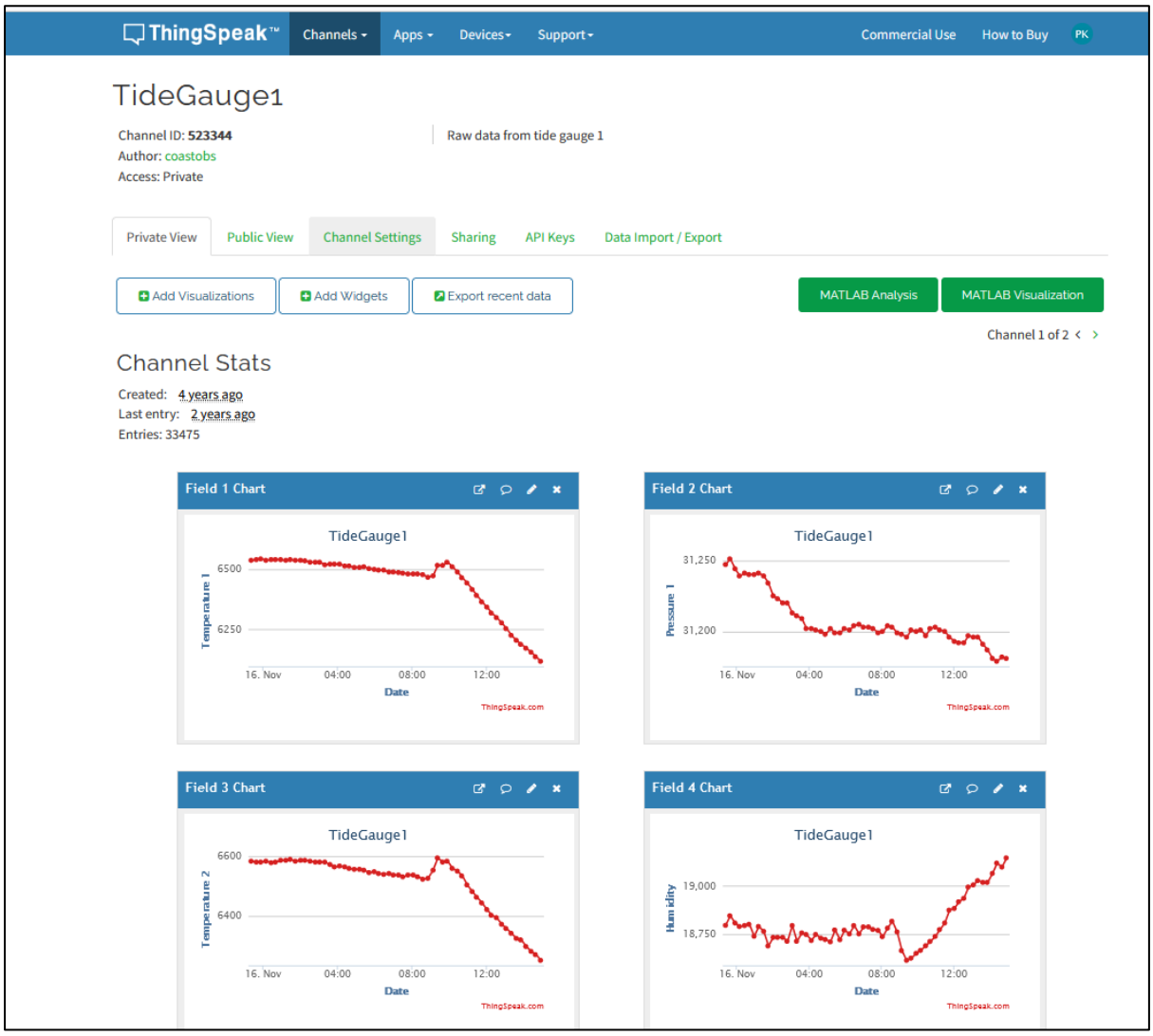

8.2.5 ThingView channel and plot display on Android application (mobile screen dump)

This is an example of two Android application views, with the right one showing the data in converted units, in this case humidity and air pressure (other channels not shown).

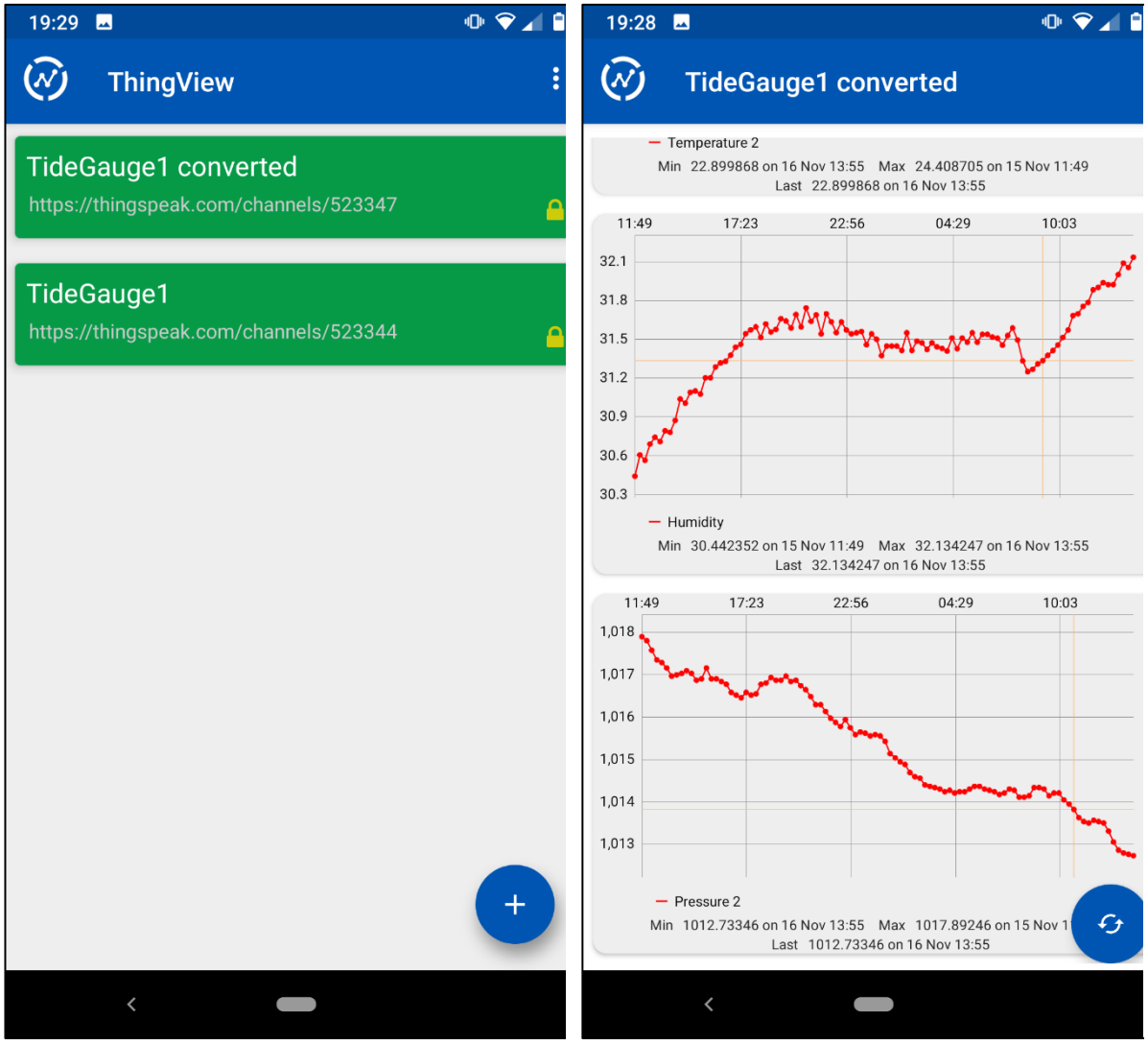

8.3 Laboratory pressure sensor calibration checks

The pressure sensors were tested in the laboratory using the set up as described in the photographs below. This shows the testing for Configuration 1 (cabled pressure sensor).

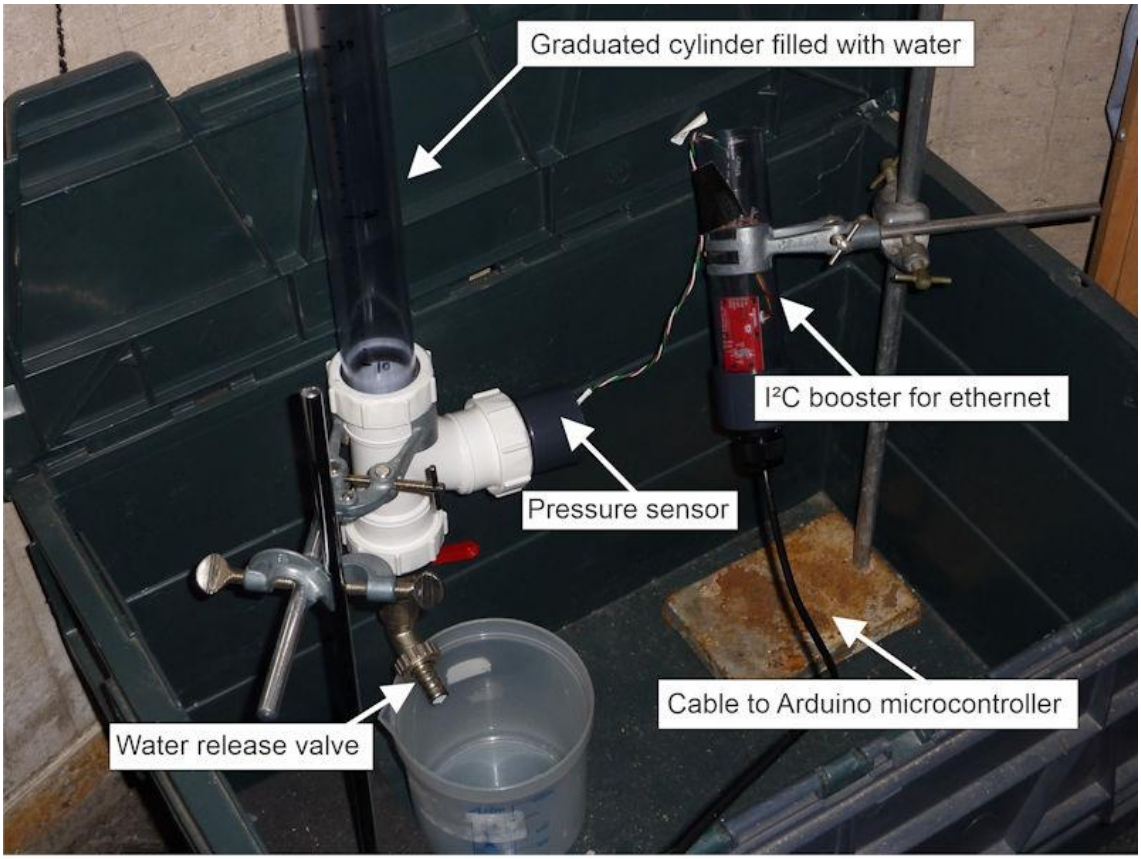

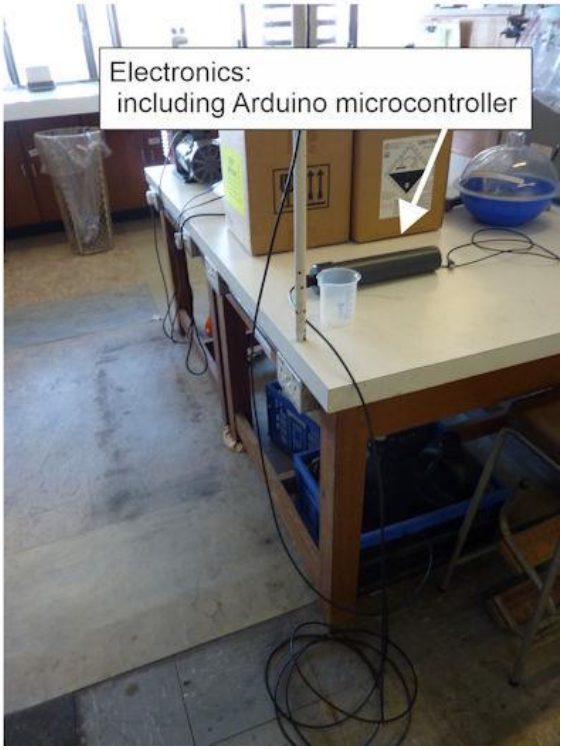

8.4 Buoyancy testing of GNSS platform

The GNSS platform was tested in West Kirby marine lake. Various weights were applied to the platform to review the buoyancy in sea water, and to determine the stability of the construction.

The following photographs show the testing in action: